



**Williams Dias Lozada Peña**

**Cavern integrity for underground hydrogen storage in the  
Brazilian pre-salt fields**

**Tese de Doutorado**

Thesis presented to the Programa de Pós-graduação em Engenharia Civil of PUC-Rio in partial fulfillment of the requirements for the degree of Doutor em Engenharia Civil.

Advisor: Prof. Deane de Mesquita Roehl

Rio de Janeiro  
May 2023

PONTIFÍCIA UNIVERSIDADE CATÓLICA  
DO RIO DE JANEIRO



**Williams Dias Lozada Peña**

**Cavern integrity for underground hydrogen storage in the  
Brazilian pre-salt fields**

Thesis presented to the Programa de Pós-graduação em Engenharia Civil of PUC-Rio in partial fulfillment of the requirements for the degree of Doutor em Engenharia Civil. Approved by the Examination Committee.

**Prof. Deane de Mesquita Roehl**

Advisor

Departamento de Engenharia Civil e Ambiental – PUC-Rio

**Prof. Raul Rosas e Silva**

Departamento de Engenharia Civil e Ambiental – PUC-Rio

**Prof. Paulo Batista Gonçalves**

Departamento de Engenharia Civil e Ambiental – PUC-Rio

**Prof. Colombo Celso Gaeta Tassinari**

Universidade de São Paulo – USP

**Dr. Leonardo Cabral Pereira**

CENPES/Petrobras

Rio de Janeiro, May 25th, 2023

Todos os direitos reservados. É proibida a reprodução total ou parcial do trabalho sem autorização do autor, do orientador e da universidade.

### **Williams Dias Lozada Peña**

Williams Dias Lozada Peña is graduated in Civil Engineering from Rio de Janeiro's State University, UERJ – Brazil in 2013. Masters in Civil Engineering from Rio de Janeiro's State University – Brazil in 2015. Researcher at the Tecgraf Institute – PUC-Rio 2018-2023. In 2018 he started the doctoral program at PUC-Rio in the research line of computational geomechanics.

#### Bibliographic data

Peña, Williams Dias Lozada

Cavern integrity for underground hydrogen storage in the Brazilian pre-salt fields / Williams Dias Lozada Peña ; advisor: Deane de Mesquita Roehl. – 2023.  
147 f. : il. color. ; 30 cm

Tese (doutorado)–Pontifícia Universidade Católica do Rio de Janeiro, Departamento de Engenharia Civil e Ambiental, 2023.  
Inclui bibliografia

1. Engenharia Civil e Ambiental - Teses. 2. Armazenamento de hidrogênio. 3. Fluência em rochas salinas. 4. Cavernas de sal. 5. Análise termo-mecânica. 6. Elementos finitos. I. Roehl, Deane de Mesquita. II. Pontifícia Universidade Católica do Rio de Janeiro. Departamento de Engenharia Civil e Ambiental. III. Título.

CDD: 624

To my grandmother Benedita Dias.

## Acknowledgments

I would like to thank my grandmother Benedita Dias and my uncle Hedivaldo Cláudio (*in memoriam*) for their support, friendship, love, affection, and patience throughout my life. I owe you my success and will be eternally grateful for all you have done for me. My mother, Laura, for her emotional support. My aunt Lígia and her husband Carlos for the encouragement.

I would also like to thank, in particular, all those who contributed to the development of this thesis:

My advisor Professor Deane Roehl for the opportunity to join the Tecgraf Institute and work/study in an immersive group with interesting and challenging activities in computational geomechanics. Thanks for all the knowledge transmitted and precious support until this moment.

The researcher Cristian Mejia for the friendship, guidance, technical support, and valuable discussions about geomechanics and computational analysis.

The researcher Paul Sotomayor for the support with the thermodynamical simulator.

The professors who contributed to my academic education and the opportunity to improve and acquire new knowledge.

All colleagues and friends of the group.

This study was financed in part by the Coordenação de Aperfeiçoamento de Pessoal de Nível Superior - Brasil (CAPES) - Finance Code 001. The authors gratefully acknowledge the support from Brazilian National Council for Scientific and Technological Development (CNPq) Grant 309384/2019-2, Carlos Chagas Filho Foundation for Supporting research in the State of Rio de Janeiro (FAPERJ) Grants E-26/202.928/2019 and E-26/201.391/2021.

## Abstract

Dias, Williams; Roehl, Deane. **Cavern integrity for underground hydrogen storage in the Brazilian pre-salt fields**. Rio de Janeiro, 2023. 147p. PhD Thesis - Departamento de Engenharia Civil e Ambiental, Pontifícia Universidade Católica do Rio de Janeiro.

Over the years, energy has been highly dependent on non-sustainable resources. However, global warming and the energy crisis urge for investments in renewable energy resources, such as hydrogen. The gas must be stored in a secure medium to avoid migration to the external environment. Thus, this work focuses on hydrogen storage in salt caverns, as these rocks present relevant properties for a storage site, such as low permeability. A workflow for cavern analysis from construction to operation is proposed, implemented, and applied to synthetic and actual field cases. Hydrogen storage provokes variations in temperature and pressure inside the cavern. The gas thermodynamics follows a diabatic solution, which updates gas pressure and temperature to represent the field conditions. The thermomechanical formulation is implemented into an in-house framework GeMA, which couples different physics. Synthetic case studies include homogeneous deposits and different cavern geometries. The results demonstrate the importance of thermal effects, as temperature amplitudes may compromise rock integrity, inducing tensile stresses and affecting its permeability. A hydraulic study demonstrated minimal hydrogen migration risk. Finally, two real field conditions were investigated, considering heterogeneous salt stratifications and a sonar-based cavern geometry. The results highlight some integrity challenges to be faced during cavern operation.

## Keywords

Hydrogen storage; Creep in salt rocks; Salt cavern; Thermomechanical analysis; Finite element.

## Resumo

Dias, Williams; Roehl, Deane. **Integridade de cavernas para armazenamento de hidrogênio nos campos do pré-sal**. Rio de Janeiro, 2023. 147p. PhD Thesis - Departamento de Engenharia Civil e Ambiental, Pontifícia Universidade Católica do Rio de Janeiro.

Ao longo dos anos, a produção de energia tem dependido de recursos não sustentáveis, como os combustíveis fósseis. No entanto, com o aquecimento global e a crise energética urge-se investir em recursos de energia renovável, como o hidrogênio. O gás deve ser armazenado em um ambiente seguro para evitar vazamentos. Portanto, este trabalho foca no armazenamento de hidrogênio em cavernas de sal, uma vez que essas rochas possuem propriedades relevantes, como a baixa permeabilidade. Um fluxo de trabalho para análise de integridade de cavernas desde a construção até a operação é proposto, implementado e aplicado para o estudo de casos sintéticos e reais. O armazenamento de hidrogênio provoca variações de temperatura e pressões dentro da caverna. A termodinâmica do gás segue uma solução diabática, atualizando a pressão e a temperatura do gás a cada instante para representar cenários de campo. A formulação termomecânica é implementada no simulador GeMA, que acopla diferentes físicas. Casos sintéticos consideram modelos homogêneos e diferentes geometrias de caverna. Os resultados demonstraram a importância dos efeitos térmicos, pois as amplitudes térmicas podem comprometer a integridade da rocha, por exemplo, induzindo tensões de tração e afetando a permeabilidade. Um estudo hidráulico demonstrou risco mínimo de migração de gás para o exterior. Por último, dois casos reais foram investigados, litologia heterogênea e uma caverna irregular baseada em dados de sonar. Os resultados evidenciaram alguns desafios na operação de cavernas.

## Palavras-Chave

Armazenamento de hidrogênio; Fluência em rochas salinas; Cavernas de sal; Análise termo-mecânica; Elementos finitos.

# Contents

|  |           |
|--|-----------|
| <b>1 Introduction</b>  | <b>18</b> |
| <b>2 Salt rocks mechanics</b>                                    | <b>26</b> |
| 2.1. Characteristics of salt rocks                               | 26        |
| 2.2. Main concepts and literature review                         | 29        |
| 2.3. Creep phenomenon  | 31        |
| 2.4. Microstructure  | 32        |
| 2.5. Constitutive models   | 33        |
| 2.5.1. Rheological models  | 34        |
| 2.5.2. Physical-empirical models                                 | 39        |
| 2.6. Summary of creep models                                     | 51        |
| 2.7. Dilatancy criteria  | 52        |
| <b>3 Salt caverns for material storage</b>                       | <b>55</b> |
| 3.1. Literature review   | 55        |
| 3.2. Hydrogen storage in salt caverns                            | 61        |
| 3.2.1. Introduction and worldwide cases                          | 61        |
| 3.2.2. Construction of a salt cavern                             | 67        |
| <b>4 Workflow for cavern integrity analysis</b>                  | <b>69</b> |
| 4.1. Cavern geometry   | 69        |
| 4.2. Initial stress state and temperature (geostatic conditions) | 70        |
| 4.3. Gas pressure and temperature                                | 71        |
| 4.4. Constitutive model for creep                                | 77        |
| 4.5. Safety criteria   | 78        |

|  |            |
|--|------------|
| 4.6. Load conditions before the cyclic operation   | 79         |
| 4.7. Cyclic operation                              | 81         |
| 4.8. Permeability measurement                      | 83         |
| 4.9. Simulation summary                            | 84         |
| 4.10. Validations in GeMA framework                | 85         |
| 4.11. Results and discussion                       | 87         |
| 4.12. Partial conclusions                          | 98         |
| <b>5 Analysis of field applications</b>            | <b>100</b> |
| 5.1. Heterogeneous salt cavern                     | 100        |
| 5.1.1. Region for the salt cavern installation     | 102        |
| 5.1.2. Rock properties                             | 103        |
| 5.1.3. Load conditions                             | 105        |
| 5.1.4. Results and discussion                      | 105        |
| 5.1.5. Partial conclusions                         | 115        |
| 5.2. Real salt cavern                              | 116        |
| 5.2.1. Region for the salt cavern installation     | 117        |
| 5.2.2. Rock properties                             | 118        |
| 5.2.3. Load conditions                             | 119        |
| 5.2.4. Results and discussion                      | 120        |
| 5.2.5. Partial conclusions                         | 125        |
| 5.3. Hydraulic analysis                            | 126        |
| 5.3.1. Salt rock porosity                          | 126        |
| 5.3.2. Salt rock and hydrogen hydraulic properties | 127        |
| 5.3.3. Load conditions and simulation details      | 127        |
| 5.3.4. Results and discussion                      | 128        |
| 5.3.5. Partial conclusions                         | 130        |
| <b>6 Conclusions</b>                               | <b>131</b> |
| <b>References</b>                                  | <b>136</b> |
| <b>Appendix A</b>                                  | <b>146</b> |

## List of Figures

|   |    |
|---|----|
| Figure 1.1 – Greenhouse gas emissions by gas ( EPA and Pachauri et al. 2014). .....   | 18 |
| Figure 1.2 – Different molecular structures - (EERE ENERGY 2001). .....   | 19 |
| Figure 1.3 – Impacts of hydrogen properties on underground storage, Hassanpouryouzband et al. (2020). .....   | 20 |
| Figure 1.4 – Hydrogen-fueled bus, COPPE (2012). .....   | 22 |
| Figure 1.5 – Costs of hydrogen storage options (Peng et al. 2023). .....  | 23 |
| Figure 2.1 - Salt rock tensile stress, Poiate (2012). .....   | 27 |
| Figure 2.2 - Salt rock stratification from TV mine, Firme et al. (2014). .....  | 28 |
| Figure 2.3 – Solubility of some salt rocks, adapted from Mohriak et al. (2008). .....   | 29 |
| Figure 2.4 – Brazilian Pre-Salt, Petrobras (2020). .....  | 30 |
| Figure 2.5 – Cavities for energy storage, Tractebel (2021). .....   | 30 |
| Figure 2.6 – Typical creep curve and its correspondent stages. ....   | 32 |
| Figure 2.7 – Most common crystalline defects. ....  | 33 |
| Figure 2.8 – Spring and viscous elements used in the rheological models. ....   | 34 |
| Figure 2.9 – Schematic representation of Maxwell model, adapted from Firme (2013). .....  | 35 |
| Figure 2.10 – Schematic representation of Kelvin/Voigt model, adapted from Firme (2013). .....  | 36 |
| Figure 2.11 – Schematic representation of Burgers model, adapted from Firme (2013). .....   | 37 |
| Figure 2.12 – Schematic representation of Minkley model, Minkley et al. (2001); Günther et al. (2015). .....  | 39 |
| Figure 2.13 – Comparison of calculated and experimental creep curve for WIPP salt- stress of 25 MPa and 1 MPa confining pressure, Chan et al. (1994). ..... | 47 |
| Figure 2.14 – Creep x time plot considering Ma et al. model - Ma et al. (2013). .....   | 50 |
| Figure 2.15 – Creep models divided into groups. ....  | 51 |
| Figure 2.16 – Principal dilatancy boundaries in the literature. ....  | 54 |
| Figure 3.1 – Factors influencing the UHS salt caverns, Aftab et al. (2021). .....   | 59 |

|   |    |
|---|----|
| Figure 3.2 – .....  | 62 |
| Figure 3.3 – Suggested European UHS sites, adapted from Hévin (2019).....   | 64 |
| Figure 3.4 – Structure map of an area in Santos basin, Alves et al. (2017).....   | 65 |
| Figure 3.5 – Proposed salt caverns for CO <sub>2</sub> storage in Brazilian pre-salt,<br>Costa (2015).....  | 66 |
| Figure 3.6 – Proposed salt caverns for H <sub>2</sub> storage in Brazilian pre-salt (Hévin<br>2019). .....  | 66 |
| Figure 3.7 – (1) initial phase, geostatic condition (2) leaching phase,<br>excavation using solution mining technique (3) debrining phase (4,5) first<br>filling and cyclic loading operation, variation of the internal pressure within a<br>predefined range, adapted from Khaledi et al. (2016). ..... | 68 |
| Figure 4.1 – Three-dimensional cavern shape, Liu et al. (2020).....   | 69 |
| Figure 4.2 – Capsular shape adopted for the UHS salt cavern.....  | 70 |
| Figure 4.3 – Axisymmetric model of the salt cavern. ....  | 71 |
| Figure 4.4 – Air mass flow rate for a cavern, Xia et al. (2015).....  | 73 |
| Figure 4.5 – Complete gas temperature and pressure calculation during a<br>cycle. ....  | 75 |
| Figure 4.6 – Van Sambeek, Ratigan, and Hansen (1993) dilatancy boundary.<br>.....   | 78 |
| Figure 4.7 – Geostatic equilibrium with very low displacements (in meters). .....   | 79 |
| Figure 4.8 – Simulation steps and their assumptions. ....   | 80 |
| Figure 4.9 – Gas pressure and temperature for case studies 1 to 4.....  | 82 |
| Figure 4.10 – Gas pressure and temperature for case study 5.....  | 83 |
| Figure 4.11 – Permeability evolution in salt rock according to Peach's (1991)<br>criterion.....   | 84 |
| Figure 4.12 – Complete procedure for salt cavern installation and monitoring.<br>.....  | 84 |
| Figure 4.13 – Orchestration to carry out REPROP inputs into GeMA.....   | 85 |
| Figure 4.14 – S11 and S22 stress components validations in GeMA. ....   | 86 |
| Figure 4.15 – von Mises equivalent stress and displacement validations in<br>GeMA. ....   | 86 |
| Figure 4.16 – Permeability validation in GeMA.....  | 87 |
| Figure 4.17 – Evaluated points in the salt cavern and the axis orientation. ....  | 87 |
| Figure 4.18 – a) Cavern pressure during the leaching stage; b) Cavern<br>pressure during the subsequent stages; c) Dilatancy index during the<br>leaching stage; d) Dilatancy index during the subsequent stages. ....  | 88 |
| Figure 4.19 – Maximum principal stresses for cases 1 to 5. ....   | 89 |

|  |     |
|--|-----|
| Figure 4.20 – Comparison between case 4 mechanical and TM analysis. ....   | 90  |
| Figure 4.21 – Stress trajectory $p \times q$ for cases 1 to 5. ....  | 92  |
| Figure 4.22 – Dilatancy index overview for all the case studies.....   | 93  |
| Figure 4.23 – Comparison of DI disturbed zones between cases 1 and 4. ....   | 94  |
| Figure 4.24 – Thermal diffusion for case study 4.....  | 94  |
| Figure 4.25 – Temperature distribution measured from the cavern’s wall for<br>case study 4 .....                                     | 95  |
| Figure 4.26 – Permeability changes in the host rock.....   | 96  |
| Figure 4.27 – Cavern displacements at all the monitored points for all the<br>case studies.....                                      | 97  |
| Figure 5.1 – Typical pre-salt lithology, Firme et al. (2014).....  | 100 |
| Figure 5.2 – Santos Basin location, Petrobras (2023). ....   | 101 |
| Figure 5.3 – Stratification from the Tupi field. ....  | 102 |
| Figure 5.4 – Salt cavern lithology in the Tupi field. ....   | 103 |
| Figure 5.5 – Gas pressure and temperature along a cycle.....   | 105 |
| Figure 5.6 – Evaluated points in the salt cavern and axis orientation. ....  | 106 |
| Figure 5.7 – Stress trajectory $p \times q$ for points A, B, D, E, and F.....  | 107 |
| Figure 5.8 – Dilatancy index for points A, B, D, E, and F.....   | 107 |
| Figure 5.9 – Mohr-Coulomb yield surface in meridional and deviatoric planes<br>(ABAQUS 2011). ....                                   | 108 |
| Figure 5.10 – Dilatancy index or MC ratio for the salt rocks. ....   | 109 |
| Figure 5.11 – Dilatancy index or MC ratio for the salt rocks. ....   | 110 |
| Figure 5.12 – Comparison of dilatancy index or MC ratio between the<br>heterogeneous and homogeneous models. ....                    | 111 |
| Figure 5.13 – Shear stresses in the salt cavern. ....  | 111 |
| Figure 5.14 – Permeability evolution at different points. ....   | 112 |
| Figure 5.15 – Comparison of the permeability evolution at different points<br>between the heterogeneous and homogeneous models. .... | 112 |
| Figure 5.16 – Displacements at the different points.....   | 113 |
| Figure 5.17 – Displacements during the cavern lifespan .....   | 114 |
| Figure 5.18 – Volume losses comparison. ....   | 115 |
| Figure 5.19 – Simulation model of the real salt cavern, based on Liu et al.<br>(2020). ....  | 117 |
| Figure 5.20 – Axisymmetric model of the real salt cavern. ....   | 118 |
| Figure 5.21 – Simulation steps and their assumptions. ....   | 119 |
| Figure 5.22 – Gas pressure and temperature along a cycle.....  | 120 |
| Figure 5.23 – Points of monitoring in the salt cavern.....   | 120 |

|  |     |
|--|-----|
| Figure 5.24 – Evaluated points in the salt cavern and axis orientation. ....               | 121 |
| Figure 5.25 – Stress trajectory $p \times q$ for points A to E. ....                       | 121 |
| Figure 5.26 – Dilatancy index for points A to E.....                                       | 122 |
| Figure 5.27 – Dilatancy index for points A to E.....                                       | 122 |
| Figure 5.28 – Comparison of dilatancy for different distances from the wall. ....          | 123 |
| Figure 5.29 – Permeability evolution at different points. ....                             | 123 |
| Figure 5.30 – Displacements at the different points.....                                   | 124 |
| Figure 5.31 – Volume loss of the real salt cavern.....                                     | 124 |
| Figure 5.32 – Permeability and porosities according to the KC model.....                   | 127 |
| Figure 5.33 – Process to run the hydraulic analysis. ....                                  | 128 |
| Figure 5.34 – Pore pressure variation during the hydraulic analysis (t = 50<br>years)..... | 129 |
| Figure 5.35 – Pore pressure variation during the hydraulic analysis (t = 50<br>years)..... | 129 |

## List of Tables

|   |     |
|---|-----|
| Table 1.1– Hydrogen properties (EERE ENERGY 2001; Aftab et al. 2021) .....                          | 21  |
| Table 1.2– UHS sites worldwide (Panfilov 2016; Zivar et al. 2021) .....                             | 22  |
| Table 2.1– Important evaporitic minerals and chemical composition, Baar (1977).....                 | 27  |
| Table 2.2– Strength values for salt rocks with different compositions, Fairhurst et al. (1979)..... | 27  |
| Table 2.3– Evaluation of the creep models. ....   | 51  |
| Table 3.1– Comparison between UHS options, Zivar, Kumar, and Foroozesh (2021).....                  | 64  |
| Table 4.1– Material properties for salt rock and parameters for the analytical. ....                | 74  |
| Table 4.2– Properties of the Brazilian halite (Poiate 2012).....                                    | 77  |
| Table 4.3– Case studies considered in the simulations.....  | 81  |
| Table 4.4 – Comparison of maximum stress in case 4 against cases 1 to 5.....                        | 91  |
| Table 4.5 – Permeability summary after the simulations. ....  | 95  |
| Table 4.6– Relevant results during the case studies. ....   | 97  |
| Table 5.1– Salt rock properties. ....   | 104 |
| Table 5.2– Creep parameters for the salt rocks. ....  | 104 |
| Table 5.3– Material properties for salt rock and parameters for the analytical. ....                | 105 |
| Table 5.4 – Material properties for salt rock and parameters for the analytical solution. ....      | 118 |
| Table 5.5– Maximum permeabilities during the simulations. ....                                      | 126 |
| Table 5.6 – Salt rock and hydrogen properties.....  | 127 |

## List of Symbols

|                 |   |
|-----------------|---|
| $\sigma$        | Normal stress                               |
| $k$             | Elastic constant of spring                  |
| $\eta$          | Viscous damping                             |
| $t$             | Time  |
| $G$             | Shear modulus                               |
| $E$             | Young's modulus                             |
| $\varepsilon$   | Strain                                      |
| $T$             | Temperature                                 |
| $\sigma_d$      | Deviatoric stress                           |
| $R$             | Universal gas constant                      |
| $Q$             | Thermal activation energy                   |
| $H$             | Heaviside step function                     |
| $T_0$           | Reference absolute temperature              |
| $\sigma_0$      | Reference effective stress                  |
| $I_1$           | First invariant of stress tensor            |
| $\omega$        | Kachanov damage                             |
| $\varepsilon_p$ | Primary creep                               |
| $\varepsilon_s$ | Secondary creep                             |
| $\varepsilon_t$ | Tertiary creep                              |
| $n$             | Exponential stress parameter for creep      |
| $\nu$           | Poisson's ratio                             |
| $\sigma^*$      | Equivalent stress                           |
| $D$             | Damage factor                               |
| $\sigma_m$      | Mean stress                                 |
| $s_{ij}$        | Deviatory stress tensor                     |
| $\delta_{ij}$   | Kronecker standard tensor                   |
| $\nabla$        | Gradient                                    |
| $\rho$          | Density                                     |
| $\dot{m}_i(t)$  | Function of the injected air mass flow rate |

|                |  |
|----------------|--|
| $\dot{m}_e(t)$ | Function of the withdrawn air mass flow rate   |
| V              | Cavern's volume                                |
| $c_v$          | Constant volume-specific heat                  |
| $h_i$          | Specific enthalpy of injected air              |
| h              | Specific enthalpy of air                       |
| u              | Specific internal energy of air                |
| Z              | Air compressibility                            |
| R              | Specific air constant                          |
| $\dot{Q}$      | Convective heat transfer rate                  |
| $h_c$          | Heat transfer coefficient                      |
| $A_c$          | Cavern wall surface area                       |
| $T_{RW}$       | Cavern wall surface temperature                |
| $\rho_R$       | Rock density                                   |
| $c_{pR}$       | Constant pressure specific heat of rock        |
| $k_R$          | Thermal conductivity of rock                   |
| $T_R$          | Temperature of rock                            |
| $\alpha$       | Charging coefficient or thermal                |
| $\beta$        | Discharging coefficient                        |
| $K_G$          | Mechanical stiffness matrix                    |
| $M_G$          | Thermo-mechanical coupling term                |
| $R_G$          | Residual force vector                          |
| $C_G$          | Thermal expansion matrix                       |
| $\Phi_G$       | Conductivity and advection capacity matrix     |
| $Q_G$          | Heat source or sink matrix                     |
| $R_{MC}$       | Mohr-Coulomb deviatoric stress measure         |
| q              | Von Mises equivalent stress                    |
| p              | Equivalent pressure stress                     |
| c              | Cohesion                                       |
| $\varphi$      | Friction angle or porosity                     |
| $\theta$       | Deviatoric polar angle                         |
| r              | Third invariant of the deviatoric stress       |
| $q_{max}$      | Maximum von Mises equivalent stress            |
| $V_0$          | Volume of the salt cavern before the operation |

|          |                        |
|----------|------------------------|
| $k$      | Rock permeability      |
| $C_{KC}$ | Kozeny-Carman constant |

# 1 Introduction

This chapter presents the main conceptions of hydrogen as an alternative energy resource. Energy is fundamental for developing a country and its population's well-being. The recent energetic crisis, which emerged from the war between Ukraine and Russia, has shown the importance of having alternative energies to supply the market and avoid discontinuities. Russia is one of the top exporters of oil, gas, and coal, and the economic sanctions imposed by several countries will aggravate the energy supply worldwide. Brazil suffered from an energy crisis in 2001, which impacted different sectors, such as industrial, security, economy, and electrical, Bardelin (2003). Thus, it is evident how having viable alternatives to supply the market and avoid discontinuities is important. For several years, the energy requirements highly depended on petroleum-based fuels and electricity powered by fossil fuels (An et al. 2011). However, these energies are not sustainable and contribute to the increase in global warming (greenhouse effect). Other activities, like agriculture, waste management, energy use, and biomass burning, also negatively impact the environment. The key greenhouse gases emitted by human activities are shown in Figure 1.1.

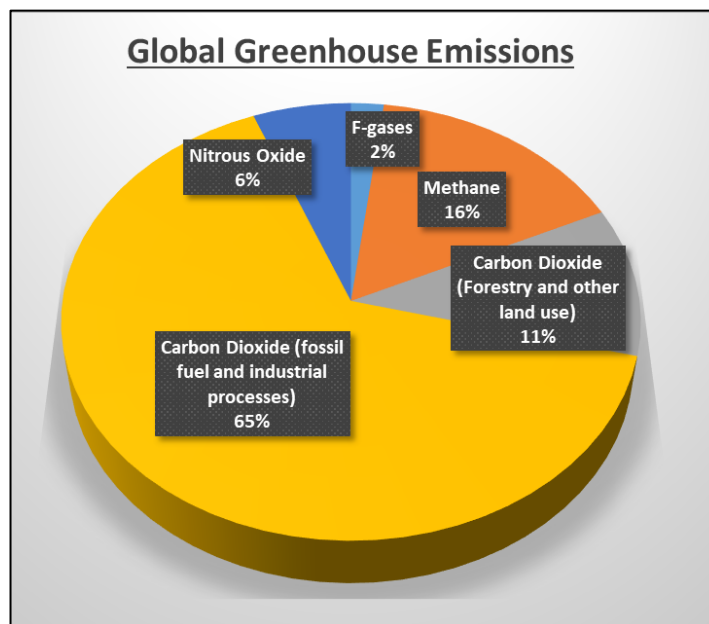


Figure 1.1 – Greenhouse gas emissions by gas ( EPA and Pachauri et al. 2014).

Investing in renewable sources assures the fulfillment of the climate protection agreements and is essential to balance fluctuations in electricity generation - Caglayan et al. (2020). In the context of the Paris Agreement climate targets by 2050, Hassanpouryouzband et al. (2020) suggest hydrogen as a suitable option to reduce the dependency on fossil fuels and accelerate the energy mix transition towards low-carbon energy sources. Recent studies from Goldman Sachs confirm that green hydrogen could supply up to 25% of the world's energy needs by 2050 and become a US\$10 trillion addressable market in the same period - Forbes (2020).

Brazil's government focus has also been redirected to hydrogen technologies, including storage. Resolution 06 was published by the Brazilian National Council for Energy Policy (CNPE) in 2021. The guidelines will include more details about hydrogen plans, and it is expected to enable a competitive market in the following years. The 2050 Energy Plan dedicated a specific chapter to hydrogen, listing it as a disruptive technology capable of significantly changing the energy market. An interesting point is the targeted link between hydrogen and natural gas. The plan suggests that the regulatory framework for hydrogen storage follows the legislation on natural gas (when it is viable). We point out that this could enable hydrogen transportation using the existing gas pipeline infrastructure, reducing operational costs. Hydrogen is the most abundant element in the universe, with a presence in about 75% of the mass of all stars and galaxies. A molecular structure compared with other gases and alcohols is shown in Figure 1.2.

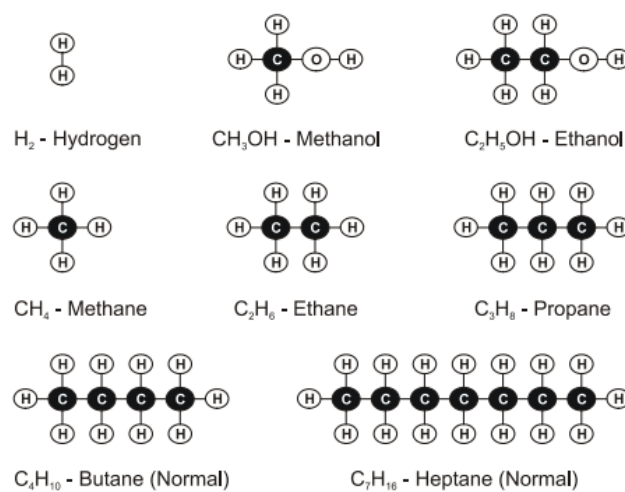


Figure 1.2 – Different molecular structures - (EERE ENERGY 2001).

Substances are present on earth as gas, liquid, or solid. They will change between these states depending on the temperature and pressure of their surroundings. In most cases, the gas turns into a liquid through a temperature reduction and from a liquid to a solid by reducing its temperature further. Increasing the pressure will sometimes provoke liquefaction and solidification at a higher temperature than required. Due to the impacts of these properties on several hydrogen applications, a better knowledge of the physical properties of hydrogen is mandatory to operate its underground storage safely - Figure 1.3.

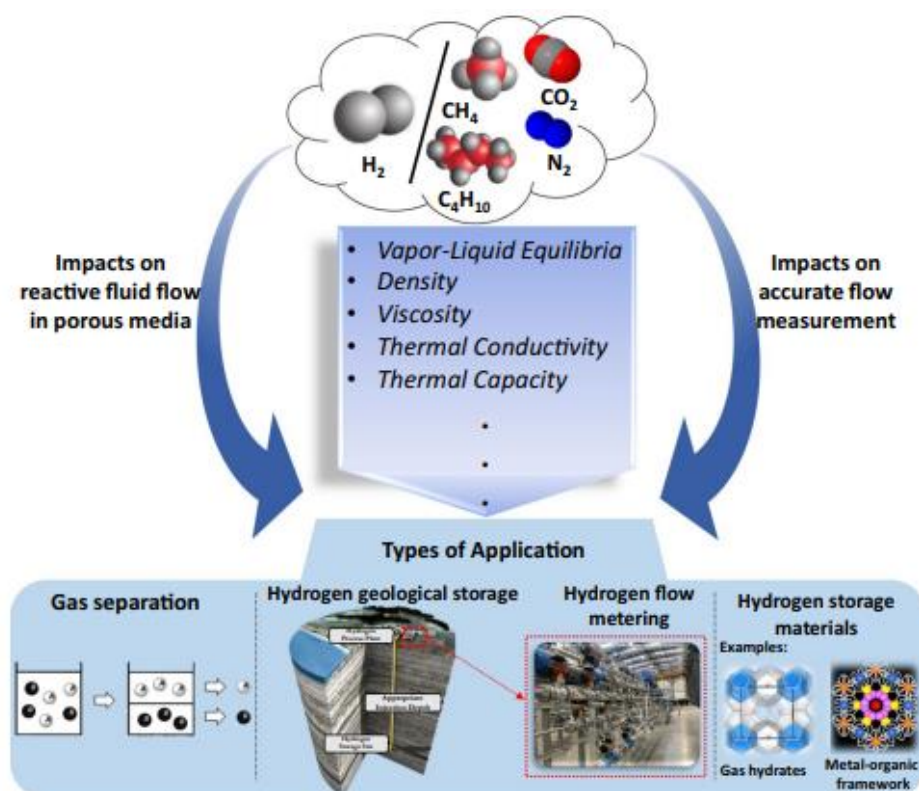


Figure 1.3 – Impacts of hydrogen properties on underground storage, Hassanpouryouzband et al. (2020).

Andersson and Grönkvist (2019) highlight the challenge of storing hydrogen. Being the lightest molecule, hydrogen gas has a very low density: 1 kg of hydrogen gas occupies over 11 m<sup>3</sup> at room temperature and atmospheric pressure. In order to make the storage economically viable, it is necessary to increase the gas density. However, current research and technologies focus on increasing gas density, for instance, modifying the density of adsorbed hydrogen in metal-organic frameworks (Liu et al. 2008).

Hydrogen is less dense than natural gas and requires more pressure to store the same gas mass. Zivar, Kumar, and Foroozesh (2021) point out that it is also less

viscous than methane, and thereby, there is a low probability of coning issues during hydrogen withdrawal. Solubility gains importance when the gas is stored in saline aquifers or depleted oil and gas reservoirs. Issues regarding hydrogen leakage may occur more frequently once it has a low molecular weight making it highly diffusive through overburden layers in comparison with air or methane storage, Simbeck (2003). A summary of the hydrogen properties is given in Table 1.1.

Table 1.1– Hydrogen properties (EERE ENERGY 2001; Aftab et al. 2021)

| Properties                                | Unit                                     | H <sub>2</sub>          |
|---|--|-------------------------|
| Molecular weight                          | -  | 2.016                   |
| Specific volume (20°C and 1 atm)          | m <sup>3</sup> /kg                       | 11.9                    |
| Viscosity (25°C and 1 atm)                | Pa.s                                     | 8.9 x 10 <sup>-6</sup>  |
| Density (25°C and 1 atm)                  | kg/m <sup>3</sup>                        | 0.082                   |
| Solubility in pure water (25°C and 1 atm) | mol.kgw <sup>-1</sup> H <sub>2</sub> (g) | 7.9 x 10 <sup>-4</sup>  |
| Normal boiling point                      | °C                                       | -253                    |
| Critical temperature                      | °C                                       | -239.95                 |
| Critical pressure                         | atm                                      | 12.8                    |
| Heating value                             | kJ/g                                     | 120-142                 |
| Diffusion in pure water (25°C and 1 atm)  | m <sup>2</sup> /s                        | 5.13 x 10 <sup>-9</sup> |

Hydrogen is also powerful energy; for instance, the combustion of 1 m<sup>3</sup> (one cubic meter) produces 12.7 MJ (Megajoules). The conversion process to electricity or heat is easy, which turns it into a viable option to be used as an energy source. Regarding non-industrial activities, it is considered an efficient replacement for natural gas (around 60%), because of its high energy potential - Aftab et al. (2021). It can be used for passenger cars, prime movers, and buses. COPPE UFRJ (COPPE 2012) already developed a hydrogen-fuelled bus, as shown in Figure 1.4. There are different ways to produce hydrogen: a) thermochemical; b) electrolytic; c) biological; c) high-temperature water splitting; d) photo-biological water splitting; e) photo-electro-chemical water splitting.



Figure 1.4 – Hydrogen-fueled bus, COPPE (2012).

Regarding its storage, underground hydrogen storage (UHS) has risen as a good alternative because of its high capacity to accommodate a significant gas volume, cost effectivity, and safety. Several hydrogen storage projects have been conducted worldwide in the last decade - Roads2HyCOM (2005), Hychico (2006), H2STORE (2012), ANGUS<sub>p</sub> (2013), InSpEE (2015), and HyINTEGER (2016), Zivar et al. (2021). Worldwide operational projects also show the viability of UHS systems. Table 1.2 presents some information regarding the principal existing sites.

Table 1.2– UHS sites worldwide (Panfilov 2016; Zivar et al. 2021)

| Site location              | Type               | % H <sub>2</sub> | P, T        | Depth (m) |
|----------------------------|--------------------|------------------|-------------|-----------|
| Bad Lauchstadt, Germany    | Salt cavern        | -                | 150 bar     | 820       |
| Kiel, Germany              | Salt cavern        | 60-64            | 80-100 bar  | 1330      |
| Ketzin (Germany)           | Aquifer            | 62               | -           | 200-250   |
| Teesside, UK               | Salt cavern        | 95               | 50 bar      | 365       |
| Texas: Air Liquid, USA     | Salt cavern        | 95               | -           | -         |
| Texas: ConocoPhillips, USA | Salt cavern        | 95               | -           | 850       |
| Texas: Praxair, USA        | Salt cavern        | -                | -           | -         |
| Clemens (USA)              | Salt dome          | 95               | 70-137 bar  | 1000      |
| Moss Bluff (USA)           | Salt dome          | -                | 55-152 bar  | 1200      |
| Spindletop (USA)           | Salt dome          | 95               | 68-202 bar  | 1340      |
| Beynes, France             | Aquifer            | 50               | -           | 430       |
| Lobodice, Czech            | Aquifer            | 50               | 90 bar/34°C | 600       |
| Diadema, Argentina         | Depleted reservoir | 10               | 10 bar/50°C | 600       |

Salt caverns are an ideal medium for storing materials and gases due to the intrinsic characteristics of salt rocks, such as low porosity and permeability, easy water solution, good creep properties, and self-healing. Regarding hydrogen, it also becomes a suitable option, as the high saline condition restricts the consumption of hydrogen by microbes (Zivar et al. 2021). From an economic aspect, the salt caverns require less cushion gas than the other storage options (depleted gas reservoirs or aquifers), approximately 20% (Chen et al. 2023). Another advantage is the possibility of multiple cycles per year, turning it into a rentable option to match the market demands. There is less concern about gas leakage, minimizing the necessary investments to guarantee site tightness. One of the most expensive steps in a salt cavern project is cavern mining, as shown in Figure 1.5. However, recent technologies are already reducing the leaching time, through high-speed levels of water injection (above 300 m<sup>3</sup>/h) or different techniques, such as multiple wells for water injection (Chromik and Korzeniowski 2021; Peng et al. 2023). Despite it being more expensive to store hydrogen than the depleted reservoirs or aquifers, at approximately 1.61 \$/kg, we highlight that this difference is eliminated with the profits from allowing multiple cycles per year and fewer investments to make the site less susceptible to chemical reactions or microbial activities. Finally, the price of crude oil stored in the above-ground tanks is about \$15-18 per barrel, but the price for underground storage in salt caverns is approximately \$3 per barrel, which speaks for the viability of salt as storage material (Peng et al. 2023).

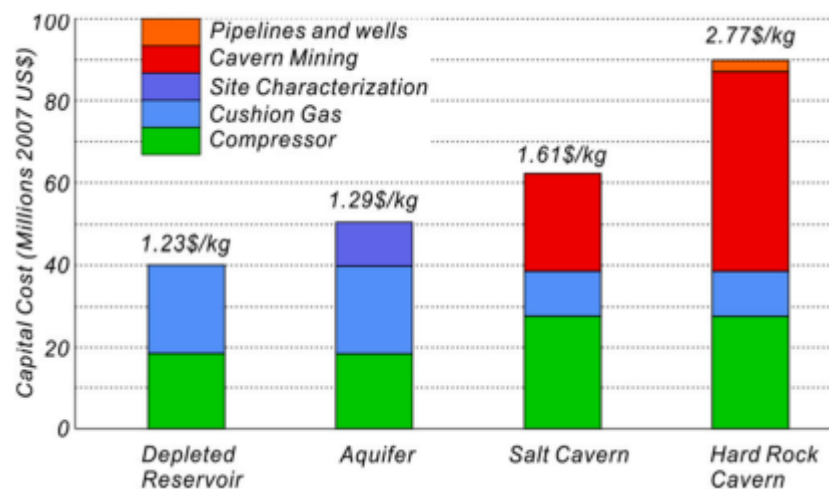


Figure 1.5 – Costs of hydrogen storage options (Peng et al. 2023).

The hydrogen production process leads to the following nomenclatures by the literature: a) grey hydrogen, b) blue hydrogen, and c) green hydrogen. Grey hydrogen is a non-sustainable option. It is produced by the steam reforming of methane in natural gas, with high carbon dioxide emissions. Grey hydrogen follows the same process as blue hydrogen, but without carbon capture and storage. On the other hand, the blue term refers to the hydrogen produced from natural gas and supported by carbon capture and storage. The CO<sub>2</sub> generated during manufacturing is captured and stored underground (Howarth and Jacobson 2021). The result is low-carbon hydrogen with no emission of CO<sub>2</sub> into the atmosphere. A sustainable process obtains green hydrogen. The energy used for electrolysis comes from renewable sources like wind, water, or solar. Considering the compromise with a sustainable engineering project, this research suggests using green hydrogen in the salt caverns.

Costa et al. (2011) discussed the great potential of the pre-salt Santos basin as a future underground storage site. Experience with underground storage worldwide also points towards the viability of these projects in Brazil. Based on that, it is relevant to understand salt rocks' creep response under the operational conditions of the deposit to assure project safety. Regarding numerical analysis, studies emphasize the mechanical behavior, gas pressure ranging between a minimum and maximum pressure. However, these pressure amplitudes provoke gas heating or cooling, and thermal effects may be relevant. These effects include tensile stresses and increased cavern convergence, as evidenced by Böttcher et al. (2017). Besides, the thermodynamic aspects of the stored gas are constantly neglected, which could help in understanding the pressure/temperature amplitudes during the operation.

Therefore, with the vast hydrogen potential as an alternative to fossil fuels and Brazilian's privileged underground storage facilities, this research proposes the installation of a salt cavern for hydrogen storage (UHS) in the pre-salt fields. These opportunities could put Brazil in a leading role in America, supplying the region and possibly Europe. Despite the importance of this topic, there are just a few studies in Brazil regarding simulations of underground storage (Costa et al., 2011a; Costa et al., 2015; Costa, 2018; Firme, Roehl, and Romanel, 2019), all of which apply only to natural gas or CO<sub>2</sub> storage. Hydrogen caverns have been projected in Europe and the United States since the 1970s. It makes evident how Brazil is still

behind in this type of project. In order to overcome the gap, this thesis provides the first assessment of salt cavern construction and operation for hydrogen storage in the Brazilian pre-salt fields. The analysis will represent the entire cavern's lifespan and consider the thermal effect of gas injection/discharge in the operation stage. The thesis is divided into six chapters, as follows:

**Chapter 1** presents the introduction, an overview of hydrogen and its characteristics, the use of salt caverns for material storage, and the objectives of this thesis.

**Chapter 2** presents creep in salt rocks, covering the phenomenon and the constitutive models after an extensive literature review.

**Chapter 3** covers a literature review of salt caverns for material storage, including hydrogen. It also discusses worldwide cases, a possible location for the Brazilian project, and the stages from cavern construction to its operation.

**Chapter 4** approaches a workflow for cavern integrity analysis. It includes cavern geometry, identifying the repository properties, definition of allowable pressures and temperature amplitudes, constitutive models, safety criteria adopted, and the necessary time to inject and discharge the gas. Finally, numerical analyses are also performed to understand the effect of different time cycles on cavern integrity.

**Chapter 5** discusses the effect of a heterogeneous salt deposit on the cavern integrity. A comparison with a homogeneous model is provided to comprehend better how different salt rocks may compromise the cavern operation. It also studies a cavern with real geometry to represent the in-field conditions competently. Finally, a hydraulic study aims to investigate the hydrogen migration into the host rock due to the medium's permeability enhancement.

**Chapter 6** summarizes the conclusions of this thesis. Future works are proposed.

## **2**

### **Salt rocks mechanics**

Salt rock mechanics is commonly associated with its creep response and dilatancy criteria to check if the compression domain is still assured and no microcracking occurs in the rock. Creep is an important phenomenon that has been the focus of many studies in recent years, mainly associated with waste deposits and developing oil extractions in ultra-deepwater. According to Lao et al. (2012), drilling and completing wells are difficult and costly procedures that require a good understanding of geomechanical concepts. Yin et al. (2019) emphasize the importance of salt rock mechanics in energy repositories.

#### **2.1.**

##### **Characteristics of salt rocks**

Salt rocks are a type of evaporitic rock generated from evaporated seawater deposits. Different from other rocks, they can change their form and dissolve in short geological intervals (millions of years) - Poiate (2012). They have very different material behaviors if compared to standard rocks. For instance, the thermal conductivity of salt rocks is about three times higher, according to Petersen and Lerche (1996). Other properties such as fracture strength, self-healing, solubility in water, and sealing capacity due to low porosity and permeability are also relevant to operations, Firme (2013). Regarding P&A (plug and abandonment) projects, enhancing sealing capacity by creep may be a useful option compared to the high costs of cement plugs - Fjær, Stenebråten, and Bakheim (2018).

Britto (2013) points out that the intense evaporation of water is responsible for increasing the concentration of ions, forming a new composition known as brine. Besides that, the presence of an arid environment contributes to the intense precipitation of these ions, generating, at last, evaporitic deposits. Table 2.1 describes the minerals present in salt deposits.

Table 2.1– Important evaporitic minerals and chemical composition, Baar (1977).

| Mineral      | Formula  | Colour (normal)    |
|--------------|--|--------------------|
| Halite       | NaCl   | Colorless to grey  |
| Sylvite      | KCl  | White, reddish     |
| Carnallite   | KMgCl <sub>3</sub> .6H <sub>2</sub> O  | Red, white         |
| Bischofite   | MgCl <sub>2</sub> . 6H <sub>2</sub> O  | Colorless to white |
| Tachyhydrite | CaMg <sub>2</sub> Cl <sub>6</sub> .12H <sub>2</sub> O                              | Yellow             |
| Kieserite    | MgSO <sub>4</sub> .H <sub>2</sub> O  | Colorless to white |
| Polyhalite   | K <sub>2</sub> MgCa <sub>2</sub> (SO <sub>4</sub> ) <sub>4</sub> .H <sub>2</sub> O | Red                |
| Kainite      | 4(KClMgSO <sub>4</sub> ).11H <sub>2</sub> O  | Reddish            |

Regarding the unconfined compressive strength (UCS), Fairhurst et al. (1979) tested some salt samples in the Sergipe salt deposit (Brazil). Table 2.2 reports the strength values.

Table 2.2– Strength values for salt rocks with different compositions, Fairhurst et al. (1979).

| Mineral      | UCS (MPa) |
|--------------|-----------|
| Halite       | 37.3      |
| Sylvinitite  | 42.3      |
| Carnallite   | 19.7      |
| Tachyhydrite | 3.0       |

Poiate (2012) performed tests with halite, anhydrite, carnallite, and tachyhydrite samples to obtain the tensile strength. The results are shown in Figure 2.1.

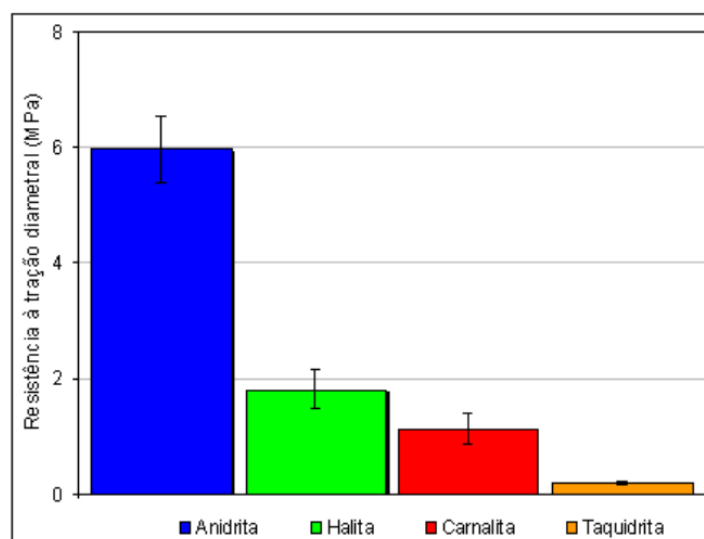


Figure 2.1 - Salt rock tensile stress, Poiate (2012).

We observed that halite has a low tensile strength, approximately 1.80 MPa, emphasizing how important temperature control is in engineering projects. The excessive amplitudes may induce high tensile stresses. An important characteristic of salt rocks is self-healing, defined as the capacity to recover from damage when exposed to sufficient pressures and temperatures, Chen et al. (2013). This process can improve the mechanical properties/permeability of damaged rocks and is related to the recrystallization of salt crystals. Fuenkajorn and Phueakphum (2011) highlight healing as a chemical and physical process associated with the evolution of material properties over time.

Considering the Brazilian scenario, the most important salt rocks are: a) carnallite, b) halite, c) sylvinite, and d) tachyhydrite. Figure 2.2 shows an example of a salt rock stratification from the Taquari-Vassouras (TV) mine in Brazil.

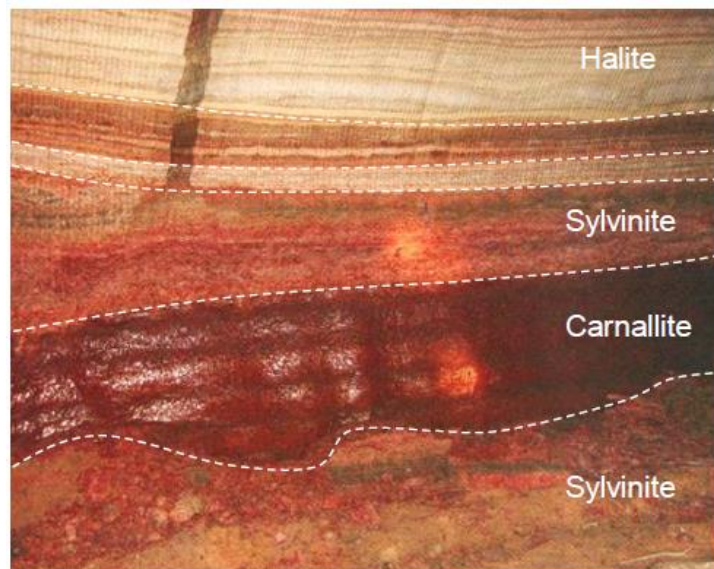


Figure 2.2 - Salt rock stratification from TV mine, Firme et al. (2014).

Carnallite is a chloride mineral made of potash, magnesium, and chlorine - Britto (2013). It is highly soluble in water and is found in variable colors, such as red, yellow, and white. Halite is almost colorless or in gray tones and is one of the most analyzed salt rocks, an object of study in several papers. Sylvinite is usually found in red/white colors and results from the crystallization of halite and sylvite, frequently named in the literature as potash, Mohriak et al. (2008). Tachyhydrite has a yellowish pigmentation and is a variation of carnallite. Its relevant properties are high solubility, mobility, and hygroscopic nature, as Baar (1977) mentioned. Figure 2.3 relates the solubility of some salt rocks.

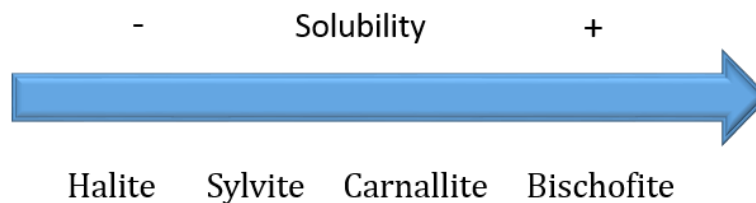


Figure 2.3 – Solubility of some salt rocks, adapted from Mohriak et al. (2008).

## 2.2. Main concepts and literature review

Unlike standard rocks, creep has an essential role in studying salt rocks. The perpetuation of slow and constant deformations over time may cause operational problems during wellbore drilling or material storage. On the other hand, in terms of P&A projects, creep may be a suitable option to reduce the high costs of creating cement sealing barriers.

The study of creep is associated with the end of the 19<sup>th</sup> century and the beginning of the 20<sup>th</sup> century, Altenbach (2003). Firstly, the interest was focused on metals and based on accidents and experimental observations. Over the years, several studies have started to evaluate creep in relation to evaporitic rocks' behavior (e.g., Lomenick and Bradshaw 1969; Munson 1979; Munson and Dawson 1982; Yang et al. 1999; Wang 2004). With the necessity for deeper water oil extraction, the advance in the oil industry has boosted the development of specific constitutive models to evaluate creep around boreholes and large cavities.

In the last decade, the discovery of advanced techniques to explore oil into deeper waters allowed access to pre-salt Brazilian fields, such as Lula and Libra fields. An overview of the Brazilian pre-salt is shown in Figure 2.4. In these areas, the water depth can exceed 2,000 m. The sequence follows a post-salt layer compounded by different rocks, such as sandstones and shales. The salt layer has thickness varies from 2,000 to 5,000 m, with a high predominance of halite rock, but there is also the presence of carnallite, tachyhydrite, and anhydrite salt rocks. Below the salt layers, we finally have the hydrocarbon reservoirs discovered under large and thick salt rock specimens, as Wang and Samuel (2016) described.

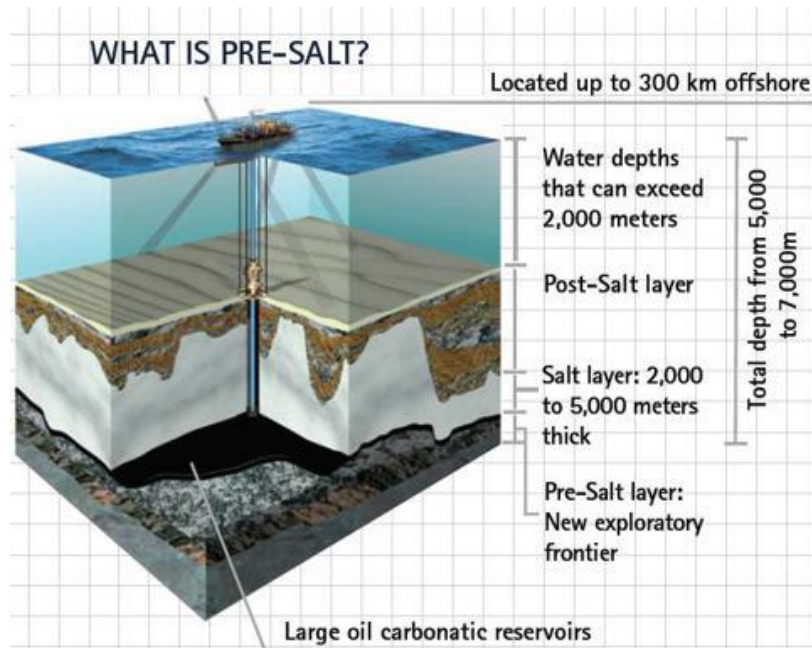


Figure 2.4 – Brazilian Pre-Salt, Petrobras (2020).

Creep studies have also been applied to solve problems regarding compressed-air energy storage (CAES), hydrogen, toxic materials, and waste residuals/gases in underground caverns (e.g., Liu et al. 2014; Nazary Moghadam et al. 2015; Khaledi et al. 2016; Chen et al. 2016). Figure 2.5 shows an example of cavities for hydrogen storage.

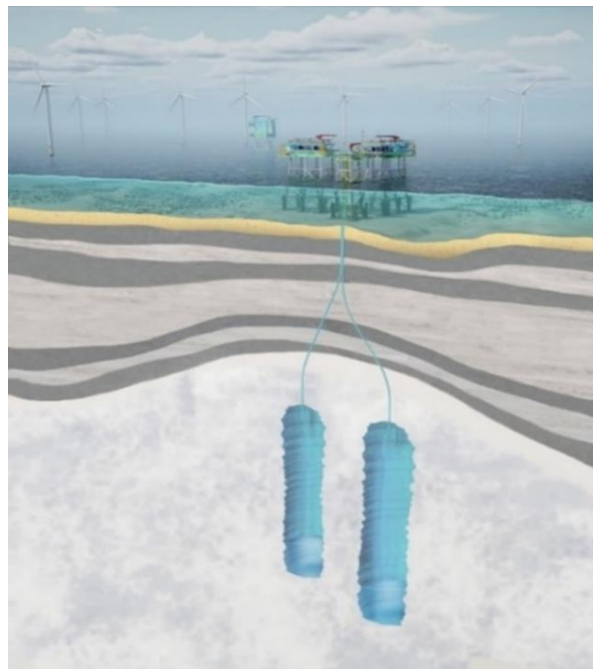


Figure 2.5 – Cavities for energy storage, Tractebel (2021).

One of the most important projects related to the creep response of salt rocks is the WIPP (Waste Isolation Pilot Plant), located in the Chihuahuan desert of southwestern New Mexico and developed by the US Department of Energy (DOE). The main objective is to encapsulate the toxic material taking advantage of the creep and healing of existing salt rocks. In particular, significant results were achieved in this project, including developing the multi-mechanism (MD) deformation model, Munson (1979).

### **2.3. Creep phenomenon**

In common sense, creep can be defined as the evolution of deformations over time under constant stress and temperature. This phenomenon is notable plastic once strains remain after the loading removal - Cella et al. (2003). The higher or lower creep rate is related to the viscosity characteristics of the material, temperature, and stress state to which the rock is subjected. Poiate (2012) highlights the importance of the material's crystalline structure. The presence of imperfections and the size of atoms and molecules are considerable aspects of this phenomenon.

Baar (1977) points out that salt rocks in the in-situ state have an elastoplastic behavior, so the salt will behave as an elastic material until the yield strength is exceeded. Once this limit is reached, the salt will begin to deform plastically by creep, and depending on the level of plastic deformations and time, damage may be verified (tertiary creep).

The complete creep process is usually divided into three stages as follows: the transient (primary creep), the steady-state (secondary creep), as well as the critical stage that precedes damage (accelerative or tertiary creep). Primary or transient creep corresponds to the first stage of the strain curve shown in Figure 2.6. Botelho (2008) highlights that the evolution of the elastic strains is the principal characteristic of this stage. After applying a given differential stress, the strain rate has a large initial value (high creep rate) that decreases over time until it maintains constant, identifying the beginning of the stationary stage.

Secondary or steady-state creep corresponds to the stationary section of the creep strain curve, Figure 2.6. Creep strains constantly occur since loading and temperature conditions remain constant. There is a balance between

work-hardening and recovery of the material, Firme (2013). This stage is most observed in the salt rock mechanics literature. Therefore, most of the proposed constitutive models consider a vast experimental database acquired in this stage, according to Munson and Dawson (1982).

Tertiary creep or accelerative creep corresponds to the final ascending stage of the strain curve shown in Figure 2.6. It is defined by a high strain rate associated with localized damage, which leads to material rupture, Aydan (2017). The dilatancy of the material occurs in this stage. Dilatancy increases the volume through micro-fracturing, resulting in the rupture of the solid body.

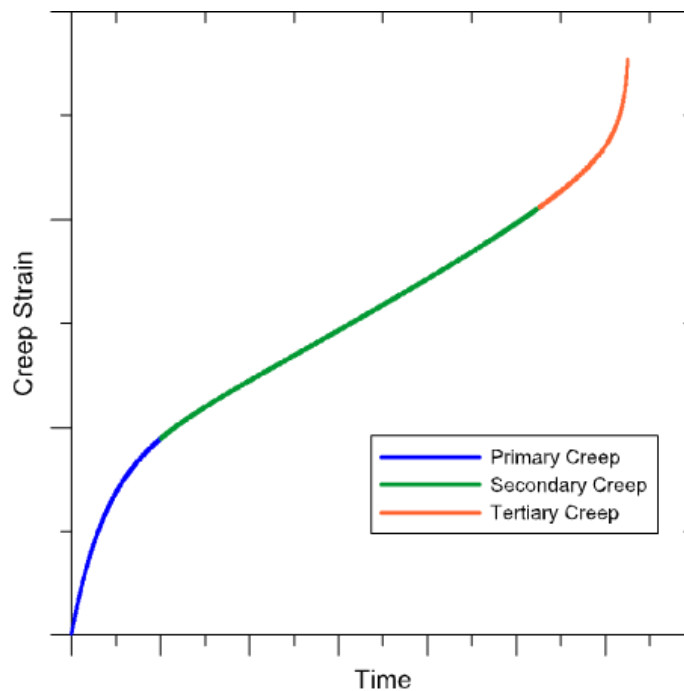


Figure 2.6 – Typical creep curve and its correspondent stages.

## 2.4. Microstructure

Although the creep process is commonly associated with stress state and temperature, micromechanisms of creep deformation cannot be neglected. Evaporitic rocks have weaker ionic bonds and imperfections in the atomic arrangement of their crystalline structure (crystalline defects). The crystalline defect is defined as a grid irregularity with one or more dimensions in the order of an atomic diameter. Classification of these defects is made based on the geometry or dimensionality of the defect.

The vacancy is a point defect in which an atom is absent in the normally occupied lattice. The auto-interstitial represents an atom of the compressed crystal into an interstitial site, a small space that, under ordinary conditions, is not occupied. Impurities occur when the solute (element or compound in a lower concentration) is added to a material called solvent (element or compound in a higher concentration) without changing the crystal structure. Imperfections are an extra plane of atoms with an edge ending inside a crystal and define the linear defects or lines of disagreement.

These crystalline defects affect the creep rate of the material, so the study of the crystalline structure is relevant for a better understanding of the subject. Figure 2.7 shows a general overview of the most common crystalline defects.

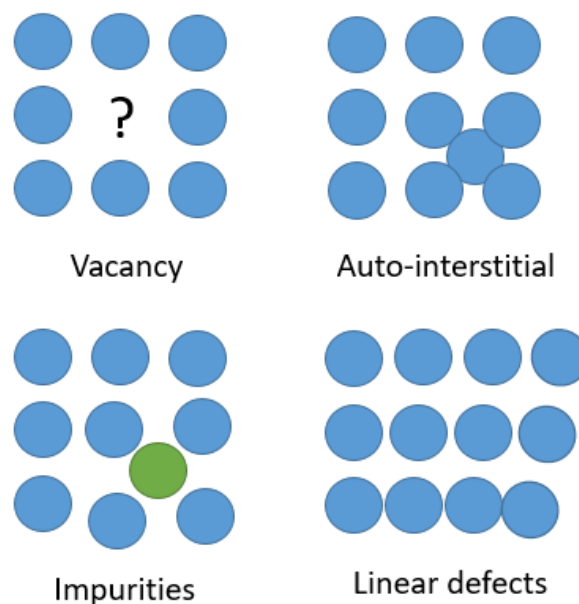


Figure 2.7 – Most common crystalline defects.

## 2.5. Constitutive models

Constitutive models developed to study creep in salt rocks have their fundamentals in the rheological and physical models proposed for metals analyses. Fuenkajorn (1988) divides the constitutive creep laws into three groups: a) rheological models, b) empirical laws, and c) physical theory models.

Costa (1984) analyzed several models described in the literature and concluded that the empirical models presented excellent results in creep evaluation

in salt mining, such as the TV mine. Firme et al. (2014) compared three different empirical relations regarding creep in salt rocks: a) Power Law; b) Multi-Mechanism Model (MD), and c) Double-Mechanism Model (D-M). Results demonstrated that the MD fits well with the experimental data. Additionally, the double-Mechanism model and the power law can be used for long and short-term conditions.

### 2.5.1. Rheological models

Rheology originates in using simplified models to simulate the creep response of different materials. These models represent the association of viscous (damping) and spring elements, which can be adjusted to represent the experimental curves obtained during the uniaxial tests. Figure 2.8 shows the basic rheological elements.

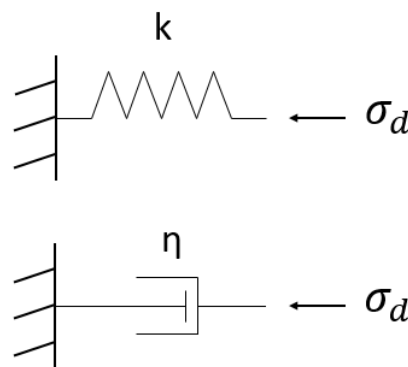


Figure 2.8 – Spring and viscous elements used in the rheological models.

The spring element shows a linear elastic response and is defined by Hook's Law as follows:

$$\sigma = k\varepsilon \quad (2.1)$$

The viscous element is assumed as a Newtonian fluid and exhibits a linear, perfectly viscous response, as represented by equation (2.2):

$$\sigma = \eta\dot{\varepsilon} \quad (2.2)$$

If the strain is null at  $t = 0$ , equation (2.3) gives:

$$\varepsilon(t) = \frac{\sigma t}{\eta} \quad (2.3)$$

Aydan (2017) describes some typical rheological models commonly used in rock mechanics: a) Maxwell Model, b) Kelvin/Voight Model, c) the Generalized Maxwell Model, d) the Generalized Kelvin Model, and e) Burgers Model.

### 2.5.1.1. Maxwell model

Maxwell model represents an in-series connection of spring and damping elements, where the deviatoric stress  $\sigma_d$  is the same in both. It requires only two constants: shear modulus ( $G_1$ ) and damping viscosity ( $\eta_1$ ). Strains are linear over time, as demonstrated in Figure 2.9.

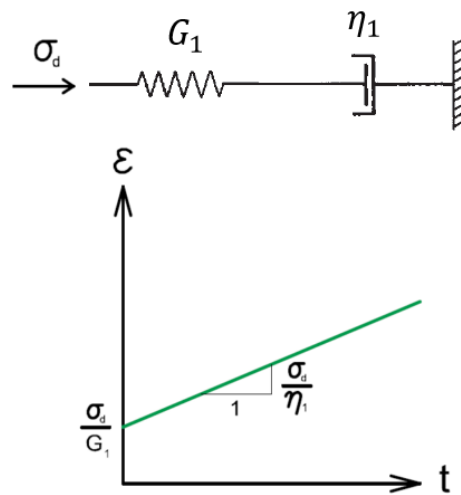


Figure 2.9 – Schematic representation of Maxwell model, adapted from Firme (2013).

The following expression defines the creep rate:

$$\dot{\epsilon} = \dot{\epsilon}_s + \dot{\epsilon}_d \quad (2.4)$$

where  $\dot{\epsilon}$  means the total creep rate and  $\dot{\epsilon}_s$  and  $\dot{\epsilon}_d$  are the strain rates in the spring and damping elements, respectively.

Assuming a constant deviatoric stress state ( $\sigma_d$ ), elastic strain in the spring element will be instantaneous and will not change with time. According to equation (2.5):

$$\dot{\epsilon} = \dot{\epsilon}_d = \frac{d\epsilon}{dt} = \frac{\sigma_d}{\eta_1} \quad (2.5)$$

In this case:

$$\int_{\varepsilon(0)}^{\varepsilon(t)} d\varepsilon = \frac{\sigma_d}{\eta_1} \int_0^t dt \quad (2.6)$$

The elastic phase can be expressed in terms of the spring constant ( $k$ ), elasticity modulus ( $E$ ) or shear modulus ( $G$ ), which convention varies from author to author. Once the lateral deformation is not simulated, we have:

$$k \approx E \approx 2G \quad (2.7)$$

Solving the differential equation, the strain rate is represented by equation (2.8):

$$\varepsilon(t) = \frac{\sigma_d}{2G_1} + \frac{\sigma_d}{\eta_1} t \quad (2.8)$$

From Figure 2.9 and equation (2.8) is reasonable to affirm that the Maxwell model adjusts well for secondary creep experiments.

### 2.5.1.2. Kelvin-Voigt model

Kelvin/Voigt model is an in-parallel association of spring and damping elements. The creep curve follows an exponential relation, according to Figure 2.10. For great periods, the strain tends to maintain constantly.

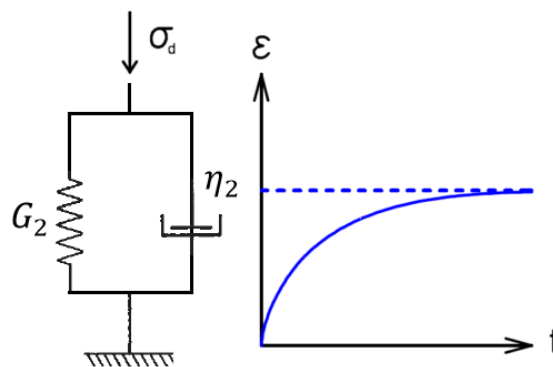


Figure 2.10 – Schematic representation of Kelvin/Voigt model, adapted from Firme (2013).

In this model, deviatoric stress is assumed to be distributed in both elements, where  $(\sigma_d^s)$  and  $(\sigma_d^d)$  refer to stress applied in the spring and damping, respectively. By equation (2.9):

$$\sigma_d = \sigma_d^s + \sigma_d^d \quad (2.9)$$

This leads to the following expression:

$$\sigma_d = 2G_2\varepsilon + \frac{d\varepsilon}{dt}\eta_2 \quad (2.10)$$

If the deviatoric stress is constant, the strain can be expressed by equation (2.11):

$$\varepsilon(t) = \frac{\sigma_d}{2G_2} \left[ 1 - \exp\left(-\frac{2G_2}{\eta_2} t\right) \right] \quad (2.11)$$

From the analysis of Figure 2.10 and equation (2.10), we concluded that Kelvin/Voigt model adjusts well for primary creep experiments.

### 2.5.1.3. Burgers model

Burgers model links the Maxwell and Kelvin/Voigt models, in other words, an in-series and parallel connection of the components. Figure 2.11 shows a schematic representation of this rheological model.

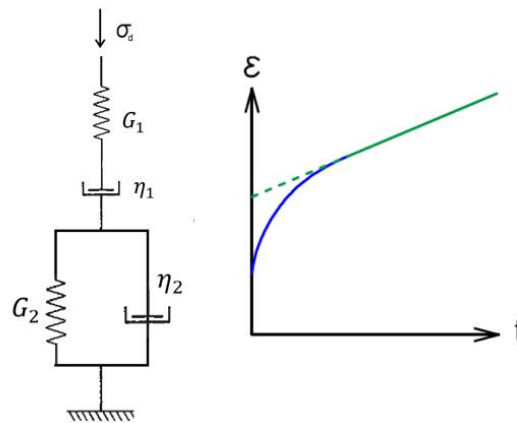


Figure 2.11 – Schematic representation of Burgers model, adapted from Firme (2013).

Equation (2.12) determine the strains:

$$\varepsilon(t) = \frac{\sigma_d}{2G_1} + \frac{\sigma_d}{\eta_1} t + \frac{\sigma_d}{2G_2} \left[ 1 - \exp\left(-\frac{2G_2}{\eta_2} t\right) \right] \quad (2.12)$$

From Figure 2.11 and equation (2.12), we observe that the Burgers model is suitable for representing the primary and secondary creep stages. Costa (1984) highlights the Burgers model as one of the most efficient rheological models to

simulate the creep response of salt rocks. However, the author points out the immense difficulty of adjusting the creep equation with the experimental curves because of the number of parameters that need to be fitted.

#### 2.5.1.4. Minkley model

Minkley model - Minkley et al. (2001) is a visco-elastoplastic model developed to evaluate creep behavior. It is a rheological approach based on the Burgers model, considering the damage and the tertiary creep stage. Equation (2.13) defines Mohr-coulomb formulation:

$$\sigma_{eff}^{Max}(\sigma_3, \varepsilon_s^{pl}) = \sigma_D + \frac{\sigma_{Max} - \sigma_D}{\sigma_\varphi + \sigma_3} \cdot \sigma_3 \quad (2.13)$$

where  $\sigma_D$ ,  $\sigma_{Max}$ , and  $\sigma_\varphi$  are strength parameters. Plastic flow occurs if stress exceeds the effective strength – Equation (2.13). In this case, equation (2.14) leads to the calculation of the incremental plastic strain.

$$\Delta\varepsilon_i^{pl,s} = \lambda_s \cdot \frac{\delta g_s}{\delta \sigma_i} \quad (2.14)$$

with  $g_s$  as the potential function of equation (2.14) and  $\lambda_s$  as the plastic shear strain increment. When the stress state exceeds the failure strength, dilatancy of the material occurs. For these cases, the authors proposed a nonlinear formulation to consider the dilatancy behavior - Equations (2.15) and (2.16):

$$\Delta\varepsilon_{vol}^{pl,s} = \lambda_s \cdot (1 - N_\psi) \quad (2.15)$$

$$N_\psi(\sigma_3, \varepsilon_s^{pl}) = 1 + \frac{\sigma_\psi^2}{(\sigma_\psi - \sigma_3)^2} \cdot \tan\beta^0 \quad (2.16)$$

where  $\sigma_\psi$  and  $\tan\beta^0$  are properties of the dilatancy function. The researchers reinforce that all material parameters are additionally dependent on the plastic shear strain  $\varepsilon_s^{pl}$ . If minimal stress exceeds the effective tensile strength, tensile failures occur. Equation (2.17) gives the plastic tensile strain increment:

$$\Delta\varepsilon_i^{pl,t} = \lambda_t \cdot \frac{\delta g_t}{\delta \sigma_i} \quad (2.17)$$

with  $g_t$  as the potential function of the tensile strength and  $\lambda_t$  as the plastic tensile strain increment. According to Günther et al. (2015), it is defined a condition that only one of both plastic terms can be active. Suppose a simultaneous violation of the shear failure threshold and the tensile strength occurs. In that case, the constitutive model enforces that either the modified Mohr-Coulomb or the tensile model is active to determine the plastic strain increment, as shown in Figure 2.12.

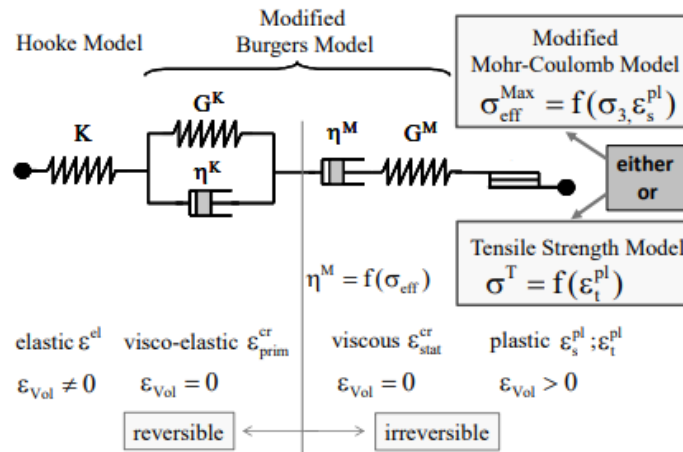


Figure 2.12 – Schematic representation of Minkley model, Minkley et al. (2001); Günther et al. (2015).

### 2.5.2. Physical-empirical models

Physical-empirical models were initially developed to study creep in metals. After successive improvements and the necessity for specific analysis in the case of salt rocks, additional models were implemented - for example, Lomenick & Bradshaw (1969). This section presents a bibliographical review of the most important physical-empirical models found in the literature (primary and secondary creep).

The Lomenick Law - Lomenick & Bradshaw (1969) is an empirical law frequently used to represent the creep response of salt rocks in geomechanical projects. This law is defined by a single constitutive equation, which incorporates deviatoric stress state, temperature, and time - Equation (2.18):

$$\epsilon_f = K\sigma^c T^b t^a \quad (2.18)$$

where  $\varepsilon_f$  is the creep strain,  $K$  ( $\text{Pa}^{-c} \cdot \text{K}^{-b} \cdot \text{s}^{-a}$ ),  $a$ ,  $b$ , and  $c$  are dimensionless experimental parameters,  $\sigma$  is the deviatoric stress state (Pa),  $T$  is the absolute temperature (K), and  $t$  is the time (s).

Despite its importance, Poiate (2012) warns that this empirical law presents limitations for large periods. The creep strains tend to nullify because of the exponential time parameter “ $a$ ,” which varies from 0.3 to 0.5. In this case, additional caution is required for nuclear waste repositories projects.

### **2.5.2.1. Multi-mechanism deformation model (MD)**

The multi-mechanism deformation model (MD) obtained from Munson (1979) is a sophisticated physical-empirical model for the numerical modeling of creep in salt rocks. Damage is not considered. According to Botelho (2008), MD consists of the superposition of three microscopic creep mechanisms (secondary creep stage) and the insertion of primary creep through inverse analysis, considering the secondary creep rate obtained previously. This model, therefore, can represent with fidelity the primary and secondary creep phases. However, its sophistication (about 16 parameters need to be defined experimentally) implies difficulties in application outside the WIPP project. The detailed three mechanisms (secondary creep stage) in the next section will allow a better model comprehension.

#### **2.5.2.1.1. Dislocation climb mechanism**

The thermal activation phenomenon influences the dislocation climb mechanism. As Senseny et al. (1992) mentioned, the climb is a well-documented recovery mechanism contributing significantly to deformation at elevated temperatures. The thermal increment provokes internal rearrangement of the molecular structure due to a higher oscillation of atoms around the equilibrium point. In this case, major or minor creep response is proportional to the temperature to which salt is submitted. Munson and Devries (1991) give the equation that defines the dislocation climb mechanism – Equation (2.19):

$$\varepsilon_{dcl} = A_1 \left( \frac{\sigma}{G} \right)^{n_1} e^{\left( -\frac{Q_1}{RT} \right)} \quad (2.19)$$

where  $\varepsilon_{dcl}$  is the creep rate in the secondary creep regime (dislocation climb mechanism),  $A_1$  is a constant ( $s^{-1}$ ),  $\sigma$  represents the generalized stress (Pa),  $n_1$  is a stress exponential,  $G$  is the shear modulus (Pa),  $Q$  is the thermal activation energy (J/mol),  $R$  is associated with the universal gas constant (J/mol.K), and  $T$  is the absolute temperature (K).

### 2.5.2.1.2. Dislocation glide mechanism

The dislocation glide mechanism is a high-stress regime controlled by the superposition of various possible dislocation slip mechanisms. According to equation (2.20):

$$\varepsilon_{dgl} = H(B_1 e^{-Q_1/RT} + B_2 e^{-Q_2/RT}) \sinh \left( \frac{q(\sigma - \sigma_0)}{G} \right) \quad (2.20)$$

where  $\varepsilon_{dgl}$  is the creep rate in the secondary creep regime (dislocation glide mechanism),  $B_1$ ,  $B_2$ , and  $q$  are constants ( $s^{-1}$ ),  $H$  is a Heaviside step function,  $\sigma$ ,  $G$ ,  $Q$ ,  $R$ , and  $T$  are the parameters described in the previous section.

### 2.5.2.1.3. Undefined mechanism

Munson and Devries (1991) state that the undefined mechanism is a low-temperature and low-stress regime. The authors clarify that the name “undefined” is because it does not represent a micromechanical model but is empirically defined by laboratory testing. Equation (2.21) gives the creep rate in this mechanism:

$$\varepsilon_{und} = A_2 \left( \frac{\sigma}{G} \right)^{n_2} e^{\left( -\frac{Q_2}{RT} \right)} \quad (2.21)$$

here,  $\varepsilon_{und}$  is the creep rate in the secondary creep regime (undefined mechanism),  $A_2$  is a constant ( $s^{-1}$ ),  $n_2$  is stress exponential,  $\sigma$ ,  $G$ ,  $Q$ ,  $R$ , and  $T$  were already explained in the previous sections.

#### 2.5.2.1.4. Creep response – MD Model

The creep response in the MD model can be expressed in two steps of calculation: secondary and primary creep.

The secondary creep rate ( $\dot{\varepsilon}_{sc}$ ) is the respective summation of each one of the mechanisms described in the last sections: dislocation climb, dislocation glide, and undefined mechanism – Equation (2.22):

$$\dot{\varepsilon}_{sc} = \dot{\varepsilon}_{dcl} + \dot{\varepsilon}_{dgl} + \dot{\varepsilon}_{und} \quad (2.22)$$

On the other hand, primary creep is determined by inverse analysis, having obtained the secondary creep rate. Firstly, it is required the determination of the intercept of the secondary creep line on the ordinate axis, considering the experimental creep curve. This intercept provides the  $K_0$  parameter, used to estimate the primary stretch (creep experimental curve) through Munson and Devries (1991) formulation – Equation (2.23):

$$\varepsilon_{pc}^* = K_0 e^{cT} \left( \frac{\sigma}{G} \right)^m \quad (2.23)$$

where  $K_0$ ,  $c$  ( $K^{-1}$ ) and  $m$  are constants. The next step is to define the transient function “F,” according to Equation (2.24):

$$F = \begin{cases} \exp \left[ \Delta \left( 1 - \frac{\zeta}{\varepsilon_{pc}^*} \right)^2 \right], & \zeta \leq \varepsilon_{pc}^* \\ 1, & \zeta = \varepsilon_{pc}^* \\ \exp \left[ -\delta \left( 1 - \frac{\zeta}{\varepsilon_{pc}^*} \right)^2 \right], & \delta \geq \varepsilon_{pc}^* \end{cases} \quad (2.24)$$

with  $\Delta$  and  $\delta$  as hardening and softening parameters, respectively.  $\zeta$  is an internal variable related to isotropic hardening, which evolution is defined by equation (2.25):

$$\dot{\zeta} = (F - 1) \cdot \dot{\varepsilon}_{sc} \quad (2.25)$$

The creep rate, considering the contribution of the primary and secondary creep stages, is given by equation (2.26):

$$\dot{\varepsilon} = F \cdot \dot{\varepsilon}_{sc} \quad (2.26)$$

Equation (2.27) gives creep along time:

$$\varepsilon(t) = \int_0^t F \cdot \dot{\varepsilon}_{sc} dt \quad (2.27)$$

### 2.5.2.2. The double mechanism creep law (D-M)

Costa et al. (2005) and Poiate et al. (2006) emphasize that the double mechanism law simplifies the equation developed by Munson. It considers the creep mechanisms dislocation glide and undefined. Equation (2.28) presents the formulation for this constitutive model:

$$\dot{\varepsilon} = \dot{\varepsilon}_0 \left( \frac{\sigma_{ef}}{\sigma_0} \right)^n e^{\left( \frac{Q}{RT_0} - \frac{Q}{RT} \right)} \quad (2.28)$$

where  $\dot{\varepsilon}$  is the strain rate due to creep at the steady-state condition,  $\dot{\varepsilon}_0$  means the reference strain rate due to creep (steady-state),  $T_0$  is the reference absolute temperature (K),  $\sigma_{ef}$  and  $\sigma_0$  are the creep effective stress and the reference effective stress (Pa), respectively,  $n$  is the stress exponential, and  $Q$ ,  $R$ , and  $T$  were defined in the previous section.

### 2.5.2.3. The multi-mechanism coupled fracture model (MDCF)

The multi-mechanism coupled fracture model, proposed by Chan et al. (1992), is an extension of the multi-mechanism deformation model (MD) to include creep-induced damage in the form of microcracks and cavities (tertiary creep). It used the database collected during the WIPP project.

This extended model couples creep and damage mechanisms in order to describe time-dependent and pressure-sensitive inelastic flow in salt rocks under nonhydrostatic triaxial compression. The authors compare it with the MD model and point out that the creep rate is pressure-insensitive, incompressible, and originates from dislocation mechanisms.

Damage-induced inelastic strain rate, on the other hand, depends on pressure, and the dilatational process is considered to arise from the opening of microcracks present in the material. The proposed formulation adopts a continuum damage variable  $\omega$  from Kachanov (1958), which measures the damage evolution over time.

The MDCF model makes possible a complete prediction of the creep phenomenon, representing the primary, secondary, and tertiary stages. However, the researchers say its application outside the WIPP project remains complex because of the lack of creep data obtained under low confining pressures and sufficient time to reach the tertiary creep regime.

### 2.5.2.3.1. Coupled creep-damage constitutive model

According to Chan et al. (1992 and 1994), both dislocation motion and creep-induced damage contribute directly to the macroscopic inelastic strain rate. In this way, equation (2.29) presents the generalized average kinetic equation for the coupled creep and damage-induced flow:

$$\dot{\varepsilon}_{ij} = \frac{\partial \sigma_{eq}^c}{\partial \sigma_{ij}} \cdot \varepsilon_{eq}^c + \frac{\partial \sigma_{eq}^\omega}{\partial \sigma_{ij}} \cdot \varepsilon_{eq}^\omega \quad (2.29)$$

$\sigma_{eq}^c$ ,  $\sigma_{eq}^\omega$ ,  $\varepsilon_{eq}^c$  e  $\varepsilon_{eq}^\omega$  are work-conjugate equivalent stress and equivalent inelastic strain rates for the dislocation and damage mechanisms, respectively.

The next step is establishing two basic premises: a) introduction of a damage variable ( $\omega$ ), to represent the reduction of the load-bearing area due to damage evolution; b) damage also contributes to the inelastic strain rate through the opening of microcracks and micro voids.

Equation (2.30) proposes formulation for the work-conjugate equivalent stress considering dislocation-induced flow:

$$\sigma_{eq}^c = |\sigma_1 - \sigma_3| \quad (2.30)$$

with  $\sigma_1$  and  $\sigma_3$  representing the maximum and minimum principal stresses, respectively. The work-conjugate equivalent stress considering damage-induced flow is given by equation (2.31):

$$\sigma_{eq}^\omega = |\sigma_1 - \sigma_3| - x_7 \operatorname{sgn}(I_1 - \sigma_1) \left[ \frac{I_1 - \sigma_1}{3x_7 \operatorname{sgn}(I_1 - \sigma_1)} \right]^{x_6} - x_1 \sigma_3 H(-\sigma_3) \quad (2.31)$$

where  $I_1$  is the first invariant of the stress tensor,  $x_i$  are material constants, and H is a Heaviside step function. As mentioned by the authors, the first term is associated with the driving force for shear-induced damage, manifested through slip-induced microcracks or grain boundary cracks whose opening leads to irreversible inelastic

strain additional to those originated from dislocation mechanisms. In the second term, a function of  $(I_1 - \sigma_1)$  demonstrates suppression of the opening of microcracks phenomenon by a confining pressure. Finally, the third term represents the opening of microcracks by the maximum tensile stress. Equation (2.32) gives the creep rate ( $\dot{\varepsilon}_{eq}^c$ ) due to dislocation mechanisms:

$$\dot{\varepsilon}_{eq}^c = F \dot{\varepsilon}_s \quad (2.32)$$

where F is a transient function and  $\dot{\varepsilon}_s$  is the overall steady-state strain rate, which corresponds to the summation of three independent dislocation mechanisms (like MD model), equations (2.33) to (2.38) :

$$\dot{\varepsilon}_s = \dot{\varepsilon}_{s1} + \dot{\varepsilon}_{s2} + \dot{\varepsilon}_{s3} \quad (2.33)$$

$$\dot{\varepsilon}_{s1} = A_1 e^{-Q_1/RT} \left[ \frac{\sigma}{G(1-\omega)} \right]^{n_1} \quad (2.34)$$

$$\dot{\varepsilon}_{s2} = A_2 e^{-Q_2/RT} \left[ \frac{\sigma}{G(1-\omega)} \right]^{n_2} \quad (2.35)$$

$$\dot{\varepsilon}_{s3} = H(B_1 e^{-Q_1/RT} + B_2 e^{-Q_2/RT}) \sinh \left[ \frac{q(\sigma - \sigma_0)}{G(1-\omega)} \right] \quad (2.36)$$

with  $A_1, A_2, B_1, B_2$  ( $s^{-1}$ ), and  $q$  as constants,  $\sigma$  is the deviatoric stress (Pa),  $n$  means a stress exponential,  $H, G, Q, R$ , and  $T$  are the parameters described in the previous sections, and  $(1 - \omega)$  represents a reduction of the load-bearing area due to damage.

The transient function ‘‘F’’ adopts the same conception defined by equation (2.24). However, equation (2.23) needs to be reevaluated to consider damage, leading to equation (2.37):

$$\dot{\varepsilon}_t^* = K_0 e^{cT} \left[ \frac{\sigma}{G(1-\omega)} \right]^m \quad (2.37)$$

here,  $K_0, c$  ( $K^{-1}$ ), and  $m$  are constants, and  $(1 - \omega)$  term is the reduction of the load-bearing area due to damage. Calculating internal variable  $\zeta$  follows the same procedure defined in equation (2.25). Equation (2.38) gives the expression in the case of damage-induced flow:

$$\dot{\varepsilon}_{eq}^{\omega} = c_1 \omega \left[ \sinh \left( \frac{c_2 \sigma_{eq}^{\omega} H(\sigma_{eq}^{\omega})}{(1-\omega)\mu} \right) \right]^{n_3} \quad (2.38)$$

where  $c_1$ ,  $c_2$ , and  $n_3$  are material constants. The authors observed some discrepancies during the evaluation of creep in the WIPP salt: a) creep damage accumulates in the transient creep region, but does not lead to tertiary creep immediately, and b) damage-induced inelastic flow strain rate exhibits a transient behavior similar to dislocation-induced creep. Then, some adjustments were necessary – Equations (2.39) to (2.41):

$$\dot{\varepsilon}_{eq}^{\omega} = F \dot{\varepsilon}_S^{\omega} \quad (2.39)$$

$$\dot{\varepsilon}_S^{\omega} = c_1 \omega_0 e^{c_3 \omega} \left[ \sinh \left( \frac{c_2 \sigma_{eq}^{\omega} H(\sigma_{eq}^{\omega})}{(1-\omega)\mu} \right) \right]^{n_3} \quad (2.40)$$

$$c_1 = c_0 \left( B_1 e^{-Q_1/RT} + B_2 e^{-Q_2/RT} \right) \exp \left[ c_4 \left( \frac{\sigma - c_5}{\sigma_0} \right) \right] \quad (2.41)$$

with  $c_0$ ,  $c_2$ ,  $c_3$ ,  $c_4$ ,  $c_5$  e  $n_3$  as material constants,  $\omega_0$  is the initial value of the damage variable  $\omega$ ,  $B_i$  and  $Q_i$  are constants of dislocation glide mechanisms. The damage evolution is defined by equation (2.42):

$$\dot{\omega} = \frac{x_4}{x_5} \omega \left[ \ln \left( \frac{1}{\omega} \right) \right]^{\frac{x_4+1}{x_4}} \left[ \sigma_{eq}^{\omega} H(\sigma_{eq}^{\omega}) \right]^{x_3} - h(\omega, T, I_1) \quad (2.42)$$

where  $x_i$  are material constants and  $h(\omega, T, I_1)$  is a damage-healing function. Additional information about damage evolution can be found in Hult & Lemaitre's (1981) studies. The authors concluded that the modifications implemented in equations (2.39) to (2.41) adjusted well to represent damage accumulation in the transient creep regime. They also affirm that the modified model can represent the creep response of WIPP salt in the hypothesis of low and high confining pressures, as shown in Figure 2.13.

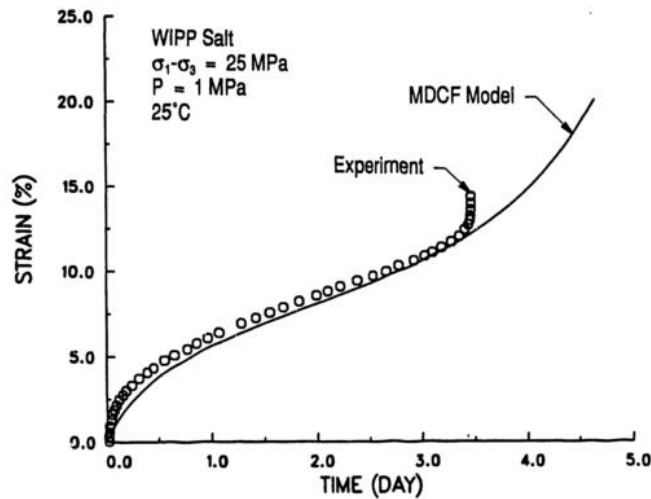


Figure 2.13 – Comparison of calculated and experimental creep curve for WIPP salt- stress of 25 MPa and 1 MPa confining pressure, Chan et al. (1994).

#### 2.5.2.4. Wang model

In the Wang model, Wang (2004) proposes a new constitutive creep-damage model for salt rocks and their characteristics. The researcher points out that the MDCF model is complex and inconvenient to use outside the WIPP project. This model introduces damage through Carter's creep model, which accurately describes salt rocks' primary, secondary, and tertiary creep stages. Two simulations with salt rock samples were performed, and the results are in accordance with the formulation described in the paper.

Considering the condition of higher stress, damage of salt rock, and transient creep in Carter's creep model, equation (2.43) gives the new creep-damage model:

$$\varepsilon = \varepsilon_t + \varepsilon_s + \varepsilon_d \quad (2.43)$$

where  $\varepsilon$  represents the total creep,  $\varepsilon_t$ ,  $\varepsilon_s$ , and  $\varepsilon_d$  are the primary (transient), secondary (steady-state), and tertiary (damage-induced) creep stages, respectively. Equations (2.44) to (2.46) represent the primary, secondary, and tertiary creep stages calculation:

$$\varepsilon_t = \frac{\sigma}{c_1} \left[ 1 - \exp\left(-\frac{G}{c_2} t\right) \right] \quad (2.44)$$

$$\varepsilon_s = A_1 \exp\left(-\frac{Q_1}{RT}\right) \sigma^n \quad (2.45)$$

$$\varepsilon_d = A_2 \exp\left(-\frac{Q_2}{RT}\right) \left(\frac{\sigma}{1-D}\right)^n t \quad (2.46)$$

where  $c_1, c_2, A_1, A_2$  e  $n$ : are material constants,  $t$  is the time,  $D$  means a damage factor ( $0 \leq D < 1$ ),  $\sigma$ ,  $G$ ,  $Q$ ,  $R$ , and  $T$  have the same meaning as those explained in the previous sections. Damage and creep enter the accelerative stage when the damage factor reaches a critical limit value ( $D_a$ ). It is proposed a damage evolution – Equations (2.47) and (2.48) following Lemaitre/Chaboche's equation, as follows:

$$\dot{D} = \left[ \frac{\sigma^*}{B(1-D)(1-\langle D - D_a \rangle)} \right]^r \quad (2.47)$$

$$\sigma^* = \sigma \left[ \frac{2}{3}(1 + \mu_0) + 3(1 - 2\mu_0) \left(\frac{\sigma_m}{\sigma}\right)^2 \right]^{1/2} \quad (2.48)$$

Where  $\mu_0$  is the Primary Poisson ratio,  $\sigma_m$  is the mean stress,  $\langle x \rangle$  represents a switch function, and  $B$  and  $r$  are material coefficients. The researcher performed some analysis (at high and low-stress levels) based on the test data for WIPP salt rock. Considering the higher stress level, the accumulation and evolution of damage lead the damage factor to exceed the accelerative limit, and then damage evolves quickly. They concluded that this creep damage model gives good representations of the creep-damage characteristics for salt rock at a high-stress level, and it can efficiently describe primary and secondary creep in the case of low-stress levels.

#### 2.5.2.5.

##### Ma et al. model

According to Ma et al. (2013), this elasto-viscoplastic damage model combines a proposed creep law with the generalized Hoek–Brown criterion model, considers the coupled creep damage /failure under various stress states, represents

the three creep stages, and verifies the deformation induced by viscous damage and plastic flow to be calculated.

According to the authors, a complete creep damage model must consider the damage evolution during these phases. The inclusion of the damage factor  $D$  into the total creep equation to reflect the creep-induced damage was proposed according to Lemaitre's strain equivalent principle. Equation (2.49) gives the new creep-damage model:

$$\varepsilon = \varepsilon_t + \varepsilon_s + \varepsilon_d \quad (2.49)$$

where  $\varepsilon$  represents the total creep,  $\varepsilon_t$ ,  $\varepsilon_s$ , and  $\varepsilon_d$  are the primary (transient), secondary (steady-state), and tertiary (damage-induced) creep stages, respectively. The transient creep stage (exponential strain curve) derives from Kelvin /Voigt rheological model - Equation (2.50):

$$\varepsilon_t = \frac{\bar{\sigma}}{c_1} \left[ 1 - \exp\left(-\frac{G}{c_2} t\right) \right] \quad (2.50)$$

where  $c_1, c_2$  are material constants,  $G$  is the shear modulus,  $t$  is the time, and  $\bar{\sigma} = \sqrt{3/2 s_{ij} s_{ij}}$ , with  $s_{ij}$  as the deviatoric stress component.

The secondary creep phase is described considering the Norton Power Law application, as follows:

$$\varepsilon_s = A_1 \bar{\sigma}^n t \quad (2.51)$$

where  $A_1$  and  $n$  are material parameters. The creep damage term ( $\varepsilon_d$ ) derives from equations (2.52) to (2.55):

$$\sigma^* = \sigma \left[ \frac{2}{3} \left( 1 + \mu_0 + 3(1 - 2\mu_0) \left( \frac{\sigma_m}{\sigma} \right)^2 \right) \right]^{1/2} \quad (2.52)$$

$$\dot{D} = \left[ \frac{\sigma^*}{B(1-D)} \right]^r \quad (2.53)$$

$$D = 1 - \left[ 1 - (r+1) \left( \frac{\sigma^*}{B} \right)^r t \right]^{1/(r+1)} \quad (2.54)$$

$$\varepsilon_d = A_2 \left( \frac{\bar{\sigma}}{1-D} \right)^n t \quad (2.55)$$

here,  $\mu_0$  and  $\sigma_m$  have the same meaning as those explained during the Wang model, and  $A_2$ ,  $B$ ,  $r$ , and  $n$  are material coefficients. Figure 2.14 shows a comparative plot between the theoretical model and the results observed in the WIPP project.

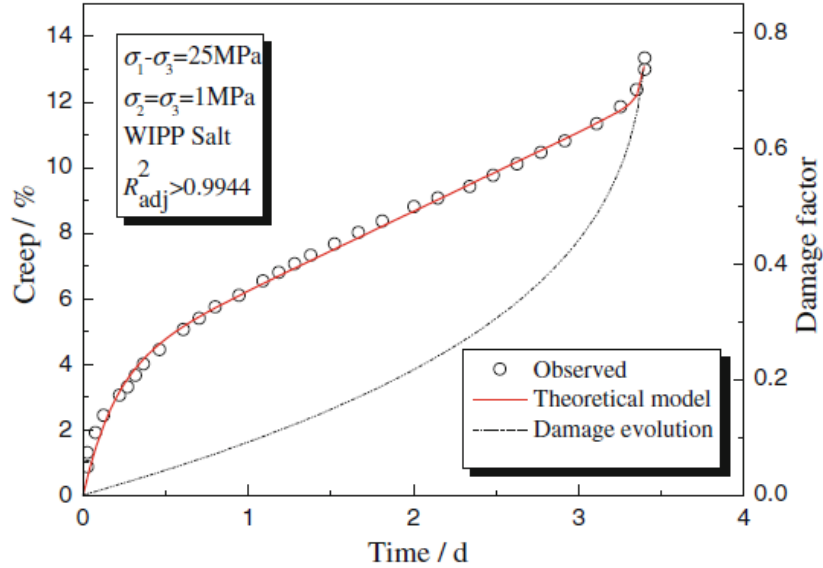


Figure 2.14 – Creep x time plot considering Ma et al. model - Ma et al. (2013).

### 2.5.2.6. The Hou & Lux model

According to Hou & Lux (1998), this model includes a phenomenological way to determine the effects of various deformation mechanisms: diffusion and dislocation, hardening, recovery, and damage healing. Equations (2.56) to (2.58) give Hou & Lux material model for the total strain rate.

$$\dot{\varepsilon}_{ij} = \dot{\varepsilon}_{ij}^e + \dot{\varepsilon}_{ij}^i \quad (2.56)$$

$$\dot{\varepsilon}_{ij}^e = \frac{1}{2G} \frac{\dot{s}_{ij}}{1-D} + \left( \frac{1}{9K} - \frac{1}{6G} \right) \frac{I_1}{1-D} \delta_{ij} \quad (2.57)$$

$$\dot{\varepsilon}_{ij}^i = \dot{\varepsilon}_{ij}^{vp} + \dot{\varepsilon}_{ij}^d + \dot{\varepsilon}_{ij}^h \quad (2.58)$$

where  $s_{ij}$  is the deviatoric stress tensor,  $\delta_{ij}$  represents the Kronecker standard tensor,  $\varepsilon_{ij}^{vp}$  is a viscoplastic strain tensor induced by the deformation mechanisms of diffusion, dislocation, hardening, and recovery,  $\varepsilon_{ij}^d$  a viscoplastic strain tensor induced by damage,  $\varepsilon_{ij}^h$  is a viscoplastic strain tensor induced by the healing of

damages,  $T$  is the absolute temperature, and  $D$  is a damage variable ( $0 \leq D < 1$ ). However, Wang (2004) stated that this model is highly complex because of the excessive number of required parameters and the model formulation.

## 2.6. Summary of creep models

After presenting the most important creep models for primary, secondary, and tertiary stages, Figure 2.15 shows a schematic representation of each group studied in this chapter.

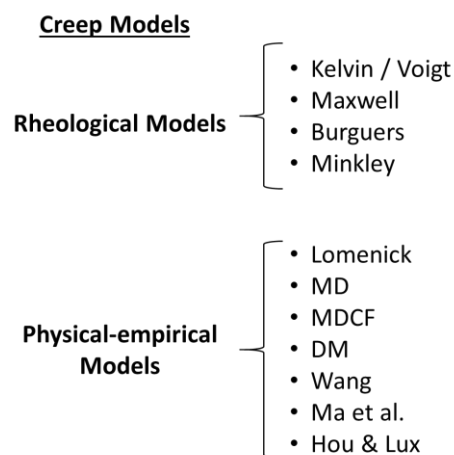


Figure 2.15 – Creep models divided into groups.

Next, Table 2.3 evaluates these creep models regarding the creep stages covered, the number of parameters, and the difficulty level.

Table 2.3– Evaluation of the creep models.

| Creep models   | Primary stage | Secondary stage | Tertiary stage | Number of parameters | Difficulty |
|----------------|---------------|-----------------|----------------|----------------------|------------|
| Kelvin / Voigt | X             |                 |                | 2                    | Low        |
| Maxwell        |               | X               |                | 1                    | Low        |
| Burguers       | X             | X               |                | 3                    | Medium     |
| Minkley        | X             | X               | X              | 10                   | Very high  |
| Lomenick       | X             |                 |                | 4                    | Low        |
| MD             | X             | X               |                | 16                   | High       |
| MDCF           | X             | X               | X              | 23                   | Very high  |
| DM             |               | X               |                | 4                    | Low        |
| Wang           | X             | X               | X              | 8                    | High       |
| Ma et al.      | X             | X               | X              | 9                    | High       |

According to the creep summary, the tertiary creep models require many parameters and present a significant difficulty level. Another difficulty is the lack of data involving Brazilian salt rocks. Among the non-damage models, the DM seems to be the most suitable for describing the creep response of rock, considering there is a great database from the national literature (Costa et al. 2005, 2006; da Costa et al. 2011; Poiate 2012). Regarding the failure, the rock integrity will be monitored through a stress-based ratio that normalizes the current deviatoric stress ( $\sigma_d$ ) by the maximum admissible value from a dilatancy criterion.

## **2.7. Dilatancy criteria**

In parallel with creep laws, dilatancy criteria have been proposed to verify the stability and feasibility of engineering projects related to salt rock mechanics. The dilatancy phenomenon is linked to damage, as the high volume expansion occurs due to micro-fractures and, consequently, a loss of material strength and the development of flow paths - Labaune et al. (2018). The literature divides these criteria into two main groups: a) strain-based criteria, which consist of defining a threshold for the strains, for example, the norm of the viscoplastic strain or its rate - Vouille et al. (1993), b) stress-based criteria, which are defined by the stress state (Spiers et al. 1988; Hunsche 1993; Van Sambeek et al. 1993; Hou 2003; DeVries et al. 2005; Labaune et al. 2018).

Firme, Roehl, and Romanel (2019) point out that salt cavern walls are in direct contact with the storage material, and access to the cavern is restricted to measuring tools. It is important to guarantee its integrity during the planned lifespan. In this context, dilatancy criteria are relevant, enhancing the safety requirements. If the dilatancy criterion is exceeded, the material will exhibit dilatant behavior. Thereby, the volumetric expansion is significant, and microcracks will become evident. Material degradation affects the strength, decreasing until failure - Schulze, Popp, and Kern (2001). There will be an increase in permeability due to the microcrack's percolation paths. In this case, the cavern's sealability may be compromised. Peach (1991) presented a study linking deformations' influence on salt rocks' fluid transport. The author proposed an equation correlating the volumetric strains with the rock permeability.

Dilatancy boundaries have their basis in laboratory tests, such as triaxial tests. The stress state is the factor with the highest impact on the dilatancy boundary. Temperature, lithology, strain rate, and salt type contribute marginally. The principal dilatancy stress-based criteria will be presented in the sequence (values considered in MPa), formulated in terms of the mean stress ( $\sigma_m$ ) and the critical deviatoric stress ( $\sigma_{d,limit}$ ). The von Mises flow rule is considered in this study, and the corresponding dilatancy envelopes are presented in such a way to be easily handled in codification for use in numerical simulators. Thus, the deviatoric stress ( $\sigma_d$ ) is expressed as  $\sqrt{3J_2}$ , where  $J_2$  is the second invariant of the deviatoric stress tensor.

Spiers' boundary (Spiers et al. 1988) originates in experiments with salt cores from the Asse mine. The tests were conducted under a temperature range from 20 to 200°C, a confinement pressure range from 0 to 50 MPa, and a constant strain rate range from  $10^{-7}$  to  $10^{-4}$  s. The authors did not observe the influence of temperature or strain rate in the results. The maximum allowable deviatoric stress is a function of the mean stress:

$$\sigma_{d,limit} = (A\sigma_m + B)\sqrt{3} \quad (2.59)$$

where  $A = 0.83$  and  $B = 1.9$ . Even when totally unconfined ( $\sigma_m = 0$ ) the material remains in the compressive regime.

Hunsche (1993) presented a dilatancy boundary based on uniaxial and triaxial tests from the Asse mine. A quadratic function of the mean stress best fits the experimental data:

$$\sigma_{d,limit} = (C\sigma_m^2 + D\sigma_m)3/\sqrt{2} \quad (2.60)$$

with  $C = -0.0168$  and  $D = 0.86$ . Popp, Kern, and Schulze (2001) highlighted that this boundary crosses the mean stress axis at approximately 50 MPa. The authors emphasize that the microcracks are closed under hydrostatic pressures higher than this value after a short time. It was also proposed a modification in the dilatancy boundary by replacing the downward trend of the parabola with a rectilinear band of low slope. Firme, Roehl, and Romanel (2019) presented the equations for the upper and lower limits, respectively:

$$\sigma_{d,limit} = A_1 e^{C_1 \sigma_m} - B_1 e^{D_1 \sigma_m} \quad (2.61)$$

$$\sigma_{d,limit} = A_2 e^{C_2 \sigma_m} - B_2 e^{D_2 \sigma_m} \quad (2.62)$$

where  $A_1 = 25.02$ ,  $A_2 = 19.06$ ,  $B_1 = 17.9$ ,  $B_2 = 19.23$ ,  $C_1 = 0.004636$ ,  $C_2 = 0.00562$ ,  $D_1 = -0.1285$  and  $D_2 = -0.1139$ .

Van Sambeek, Ratigan, and Hansen (1993) performed triaxial tests with WIPP salt samples, defining Ratigan's boundary. It is one of the most utilized in Brazilian salt rock projects (Costa et al. 2005, 2006, 2011; Poiate 2012; Firme et al. 2014). The function is expressed by:

$$\sigma_{d,limit} = (0.81\sigma_m)\sqrt{3} \quad (2.63)$$

DeVries' boundary (DeVries et al. 2005) is based on the laboratory tests carried out with salt samples from a formation near Cayuta, New York. It considers the effect of intermediate stress on the rock strength and the mechanical responses for compression/extension due to the Lode angle ( $+30^\circ$  for triaxial compression and  $-30^\circ$  for triaxial extension). The presented function is:

$$\sigma_{d,limit} = \left( \frac{E(|3\sigma_m|)^k + F}{\sqrt{3}\cos\theta - G\sin\theta} \right) \sqrt{3} \quad (2.64)$$

where  $E = 0.77$ ,  $F = 1.95$ ,  $G = 0.524$ ,  $k = 0.693$  and  $\theta$  is the Lode angle. The referred dilatancy boundaries are shown in Figure 2.16.

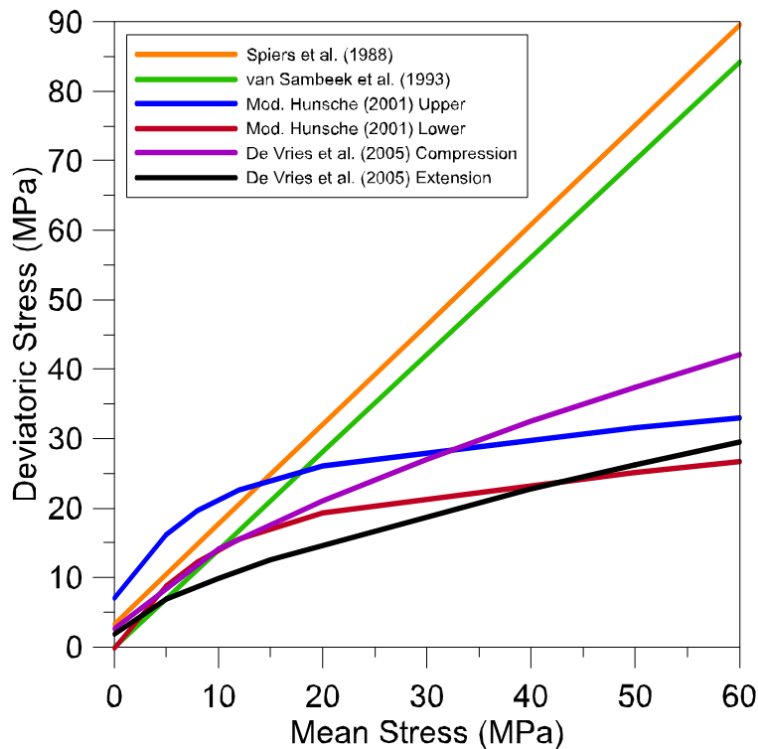


Figure 2.16 – Principal dilatancy boundaries in the literature.

### **3 Salt caverns for gas storage**

Salt caverns are cavities created by the leaching out of salt formations. Due to the salt rock's low permeability, their use emerges as an ideal way to ensure a natural barrier formation and prevent fluid/gas migration to the surface. Depending on the type of material storage, some requirements, and additional criteria may be necessary during the engineering project.

#### **3.1. Literature review**

This section will do a short literature review about salt caverns and their use in material storage. According to Foh et al. (1979), the first successful underground storage of natural gas occurred in Ontario (1915) in a partially depleted gas field. During the II World War, more studies considered the storage of fluids and gases in salt caverns - Bays (1963).

In the United States, underground storage of materials in dissolved salt cavities took place, for the first time, in 1949, Texas - Parker (1958). Pierce and Rich (1962) analyzed the viability of several salt deposits in North America to be used as repositories for radioactive materials rejects. Lomenick and Bradshaw (1969) focused on understanding the stability of underground salt structures when submitted to high temperatures while storing high-level radioactive waste. Boucher et al. (1979) provided a mathematical model to predict volume changes for cavity pressure history. In Germany, Langer et al. (1993) discussed using solution-mined caverns in salt for oil/gas storage and toxic waste disposal in terms of safety aspects. According to the authors, the safe disposal of toxic and radioactive wastes has become an increasingly important problem for modern engineering.

Staudtmeister and Rokahr (1997) performed numerical simulations and defined a criterion to verify the safety of salt cavities. Bérest et al. (2001) focused on the abandonment analysis of salt caverns, which is important for avoiding environmental problems. The objective was to measure the brine equilibrium

pressure reached when the cavern was closed. Beutel and Black (2005) emphasized that the United Kingdom (UK) has many salt deposits. Mining for salt production is one of the oldest industries in the country. The authors provided a geological overview of the principal salt deposits in the country and focused on an individual gas cavern storage project in the city of Cheshire. Still in the UK, the Teeside site was the first hydrogen underground deposit in the world, and it has been operating since the 1970s, with a total volume of 210,000 m<sup>3</sup>.

Costa et al. (2011, 2015) considered underground natural gas (UGS) and CO<sub>2</sub> storage in Brazil's deep/ultra-deepwater offshore salt caverns. The authors point out that Petrobras is studying these activities' technical and economic feasibility, which could take advantage of the previous know-how acquired during oil exploration in the pre-salt fields. Da Costa (2018) evaluated the potential use of salt caverns for UGS in these areas, providing a better understanding of operational challenges regarding the geological and logistical aspects. However, there is a lack of research regarding hydrogen storage in the pre-salt fields. Therefore, this thesis expects to contribute to a better understanding of UHS projects in Brazilian ultra-deep waters. The thesis will consider gas thermodynamics (important to represent the pressure and temperature variations during hydrogen injection/discharge) and provide a thermomechanical analysis covering the entire process: from construction to operation. Thus, it sets the primary basis for a complete engineering project in Brazil.

Ozarslan (2012) investigated the existing underground gas storage methods and designed aspects of salt caverns for large-scale purposes. It concluded that a solar-hydrogen and natural gas system could be utilized to meet future large-scale energy storage requirements. Brouard et al. (2013) described brine outflow and shut-in pressure tests performed in a 250-m deep cavern in France. The objective was to assess the long-term creep and the possible consequences regarding environmental protection. Nazary Moghadam et al. (2013, 2015) presented an elasto-viscoplastic constitutive model to describe dilatancy, short-term, and long-term failure during transient and steady-state creep of rock salt caverns. Iordache et al. (2014) examined Romania's energy system structures to evaluate the country's current potential for underground hydrogen storage (UHS). Simon et al. (2015) provided a comprehensive study about the geological potential for hydrogen

storage in Spain and the competitiveness of hydrogen storage against other large-scale energy concepts.

Zhu, Pouya, and Arson (2015) analyzed the microscopic mechanisms that control the transition between secondary and tertiary creep around salt caverns in typical geological storage conditions. They observed that the initiation of tertiary creep is linked to the stresses and the viscoplastic strains. Damage also concentrates near the top of the cavern, indicating a critical region. The potential use of salt caverns for strategic oil storage was observed by Niu et al. (2015). The authors affirmed that salt caverns for oil storage are rarely seen in China. Thus, a constitutive model was presented based on thermodynamic, percolation, and creep theories. Liang et al. (2016) investigated the creep evolution of a selected salt cavern. Specific indexes, for example, the cavity volume shrinkage and safety factors of surrounding rocks, were calculated under different operating conditions. An optimized model was also presented to improve the analysis in terms of cavity shape and the height-diameter ratio.

Ma et al. (2017) proposed a salt rock creep damage model to evaluate the stability and serviceability of a storage cavern in a bedded salt formation under different loading scenarios, which could well represent the variations during the cavern operation. Böttcher et al. (2017) verified the influence of temperature on the cavern capacity through a thermomechanical model. The gas temperature followed a diabatic analytical solution proposed by Xia et al. (2015). This solution assumes that the gas density inside the cavern is constant at a given time step and that heat diffusion into the rock salt occurs very fast. Safety criteria, such as the absence of tensile stresses, the definition of a dilatancy criterion, low convergence rates, and limited ground subsidence, were considered during the analyses. Due to the reduced operational cycles (characteristic of hydrogen storage), the high-temperature amplitudes emphasized the importance of thermomechanical simulations, principally because of the undesired risk of tensile stress when the cavern is cooled, an effect of gas depressurization during the discharge period.

Wang et al. (2018) investigated gas storage in China's ultra-deep salt cavity (more than 1800 m in depth). This cavern will be the deepest UGS salt cavern in Asia. The authors proposed a new index system composed of displacement, volume shrinkage, plastic zone, dilatancy safety factor, and equivalent strain to evaluate the cavern's safety. Bérest (2019) discussed aspects related to the thermodynamics of

salt caverns containing brine, oil, natural gas, air, or hydrogen. The author points out that the heat capacity is much smaller in a gas cavern, temperature evolutions are much faster, and heat transfer from the rock mass is relevant. Firme, Roehl, and Romanel (2019) extensively reviewed salt caverns' history and the fundamentals of their mechanical behavior. Simulations considered both the construction and operation periods. The results demonstrated that the salt cavern remained tight, thereby safe.

Li et al. (2020, 2021) observed the temperature-pressure effects on the stability of salt caverns. These coupled mechanisms cause effective stress variation on the cavern wall and consequently modify the creep rate. The results indicated that the affected region by cyclic pressure and temperature is approximately 10 m inside the rock salt from the cavern wall. The critical area was found at the cavern top, indicating it is most liable to deformation damage. Caglayan et al. (2020) conducted a technical study to analyze the potential of salt caverns across Europe for hydrogen storage. The assessment considered the land eligibility constraints derived from a review of the relevant literature, distributed the caverns across eligible locations, and finally estimated the individual cavern storage capacity by factoring in the salt formation characteristics regarding thermodynamic storage considerations. Liu et al. (2020) evaluated UHS caverns in bedded salt rocks in China (Jintan salt mine). Several criteria, such as volume loss rate, distribution of plastic zones, and deformation around the wall rock measured the stability of the salt cavern. Results indicated the possibility of this project, as the site requirements were satisfied. Lyu et al. (2021) and Zhao et al. (2021) focused on developing creep-damage constitutive models based on experimental data calibrations and their further application to salt caverns.

Zivar, Kumar, and Foroozesh (2021) presented a comprehensive review regarding hydrogen storage in salt caverns. The discussion involved worldwide operating and potential sites, salt rock properties, monitoring mechanisms, optimization of injection-withdrawal strategies, microbial/geochemical activities, physics of hydrogen flow in porous media, and hydrodynamics activities (rock-fluid and fluid-fluid interactions). Portarapillo and Di Benedetto (2021) provided a risk assessment of the large-scale hydrogen storage in salt caverns. They also considered the influence of hydrogen contamination by bacterial metabolism, and the gas composition was expressed as a time variable. Ramesh Kumar et al.

(2021) studied the impact of heterogeneity on the deformation of salt caverns and the state of stress around the caverns. Simulations considered the influence of a cavern on the adjacent caverns and the sensitivity analysis of parameters involved with creep and damage. Aftab et al. (2021) focused on understanding the geological aspects of hydrogen storage. According to the authors, the injection/production cycles of  $H_2$  can influence the geomechanical characteristics of salt caverns, as shown in Figure 3.1.

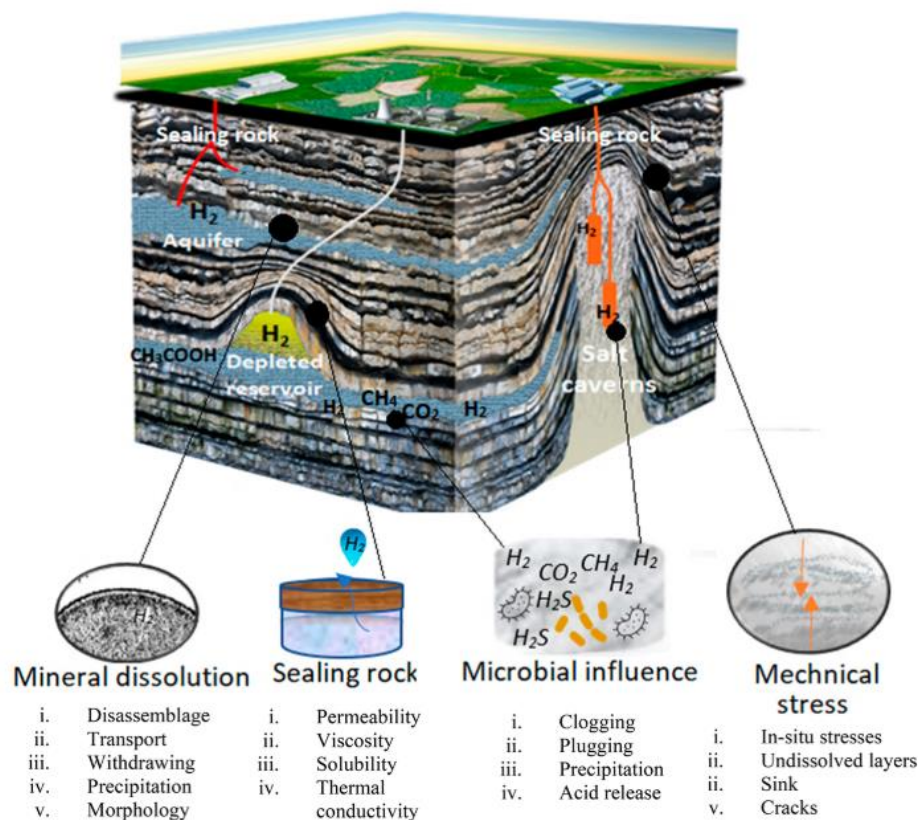


Figure 3.1 – Factors influencing the UHS salt caverns, Aftab et al. (2021).

Lankof, Urbańczyk, and Tarkowski (2022) presented a methodology for assessing salt domes' hydrogen storage potential. It considers the size of storage caverns, their depth, the influence of convergence, and the geological structure of the selected salt domes. They also performed statistical analysis of data from the underground cavern storage facility in the Mogilno salt dome. Wang et al. (2022) proposed nonlinear creep damage of salt rock for displacement prediction of a salt cavern used for gas storage. The constitutive model considers the connection of two viscous bodies with the conventional elastic body and the Kelvin model in series. Cai, Zhang, and Guo (2022) improved the capabilities of GPSFLOW (General

Purpose Subsurface Flow Simulator) for modelling grid-scale hydrogen and gas mixture storage in a cavern, deep saline aquifers, and depleted gas fields.

Lyu et al. (2022) focused on understanding salt rock's mechanical characteristics and gas tightness through a thermal-hydro-mechanical (THM) coupling condition. The effective confining pressure and inelastic volumetric strain were considered to predict salt rock's permeability evolution under different temperatures. The authors point out that better comprehending these mechanics is crucial for the safety evaluation of salt caverns. Grgic et al. (2022) monitored the evolution of gas permeability of rock salt under different loading conditions and its implications on the UHS in salt caverns. The results demonstrated that underground hydrogen storage in salt caverns is the safest solution because the different mechanisms (viscoplasticity with strain hardening, microcracking, and crack healing) involved in material deformation act competitively to annihilate any significant permeability evolution. Abreu et al. (2023) provided a feasibility study of offshore blue or green hydrogen storage in salt caverns created by leaching within potentially identifiable salt deposits extent of the Gulf of Mexico coastline (US). However, the analysis still neglects the thermal effect during the operation time of 30 years, which may be relevant. The permeability evolution of salt rock was ignored in the simulations. Thus, the analysis focused only on the mechanical aspects of salt caverns.

Therefore, salt caverns are suitable for material storage, particularly natural gas, CO<sub>2</sub>, and hydrogen. Different studies approached the topic from the perspectives of site selection, rock tightness, and cavern creep, among others. This research will analyze salt caverns for hydrogen storage (UHS) purposes, considering the enormous potential in the following years and the increasing necessity for storing renewable energy. It follows the paper published by the author – Dias et al.(2023). Also, Brazilian's future energy strategy, expressed by the 2050 Energy Plan, corroborates hydrogen as an energy alternative. In this context, the thermomechanical and thermodynamic analysis will fill the gap in the Brazilian literature on the integrity assessment of salt caverns for gas storage. The hydraulic study will also better comprehend how hydrogen propagates into the host salt rock and the possible impacts on the cavern integrity.

## 3.2. Hydrogen storage in salt caverns

This section will approach the specific case of hydrogen storage in salt caverns, contemplating an introduction of the theme, a review of worldwide cases, the pros and cons of hydrogen storage, and finally, the steps of cavern creation.

### 3.2.1. Introduction and worldwide cases

Salt caverns are an ideal medium to store materials and gases due to the intrinsic characteristics of salt rocks, such as the low porosity and permeability, easy water solution (ideal for building and shaping caverns), good creep properties and self-healing. For instance, laboratory experiments show permeabilities below  $10^{-20}$  m<sup>2</sup>, and field measurements still give values below  $10^{-18}$  m<sup>2</sup>, even with inhomogeneities and local disturbances (Schulze et al. 2001; Fuenkajorn and Phueakphum 2011; Chen et al. 2013). Panfilov (2016) highlights the advantage of salt caverns concerning bacteria proliferation: in highly concentrated brine (salt caverns), they do not transform hydrogen into other gases.

In comparison with the storage of other gases in salt caverns, we may cite the influence of gas thermodynamics is much more pronounced in the hydrogen ones, as the cycles have high frequencies to match the market demands, in the order of days to weeks (Peng et al. 2023). In a CO<sub>2</sub> application, the effect of gas discharge becomes unnecessary, as the intention is to store and retain the gas confined in the cavern. Also, hydrogen purity gains special relevance depending on the targeted application, for instance, fuel cells. In this case, concerns about chemical reactions are necessary. Zivar et al. (2021) point out the less viscosity of hydrogen than methane, which leads to a lower chance of coning issues. From the regulation aspect, there are existing regulations regarding natural gas storage, CO<sub>2</sub> storage requires further legislation. In the case of H<sub>2</sub> storage, legal regulations need to be developed based on the experience of storing other gases (Tarkowski 2019). Hydrogen storage requires more attention to gas diffusion: air-diffusion coefficient in excess of air is 3.6 and 4.7 times higher for hydrogen than methane and carbon dioxide, respectively. Tarkowski (2019) highlights the importance of the calorific value to consider in underground storage of H<sub>2</sub> and CH<sub>4</sub> (CO<sub>2</sub> is a

non-flammable gas). Hydrogen has a high mass-energy density of 120 MJ/kg (min). For methane, this parameter is 55.6 MJ/kg. However, it has a very low energy density of 0.01079 MJ/L (0.0378 MJ/L for methane). The author also compared the different gases and site locations, as shown in Figure 3.2.

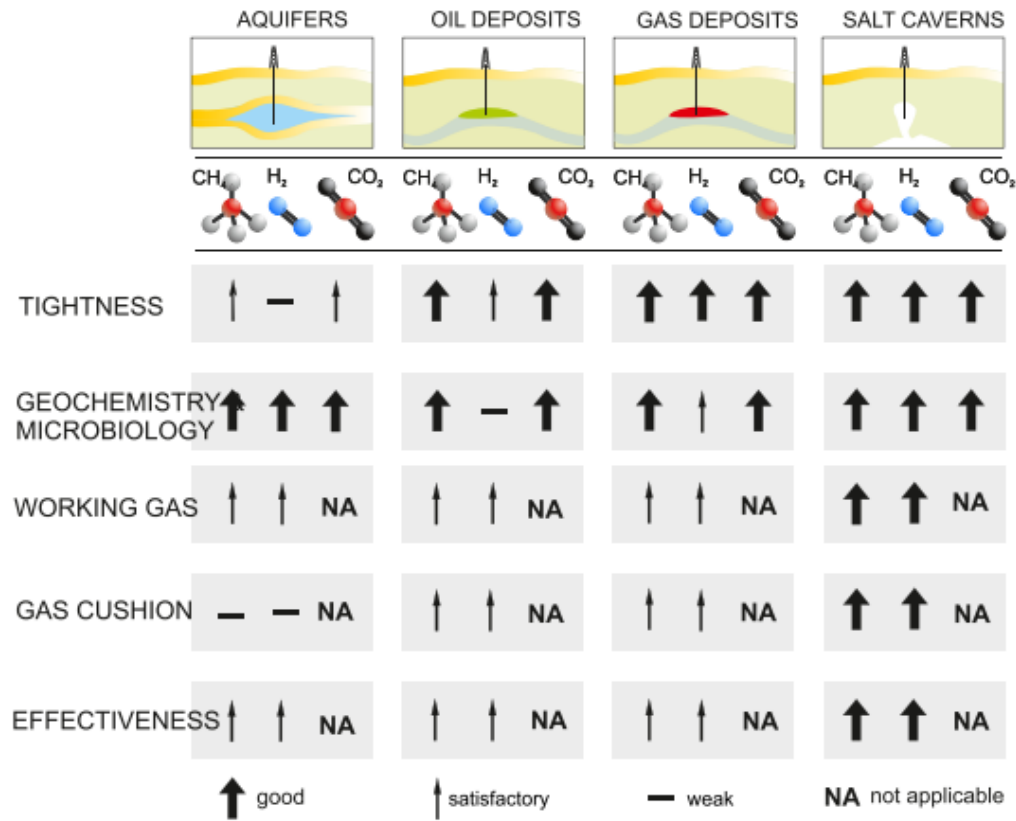


Figure 3.2 – Comparison of different gases storage (Tarkowski 2019).

We observe that the salt caverns efficiently guarantee the site tightness independent of the gas stored. They are also good for reducing the risk of microbial activity due to the high-saline concentration. A significant risk is evidenced in CO<sub>2</sub> storage: gas leakage for the environment is highly prejudicial, as it contributes to the greenhouse effect. The pros and cons of hydrogen salt caverns are listed below, according to Böttcher et al. (2017) and ENGIE (2021):

**Pros:**

- Flexibility: Salt caverns are flexible regarding injection and withdrawal cycles to meet market demands. Depending on their depth, they may be operated at pressures of 200 bars and allowing for large-volume hydrogen storage (from 9 to 6,000 tons);

- **Safety:** Salt caverns allow the safe storage of large quantities of hydrogen under pressure, because of their tightness. For instance, a hydrogen storage cavern built in the United Kingdom in 1972 is still in service.
- **Resilience:** Some existing salt caverns could be quickly converted to hydrogen storage. Storengy ( the largest storage operator in France) is developing UHS projects to anticipate the sector's needs and adapt its infrastructure through the HyPSTER and HYGREEN Provence projects;
- In comparison with CAES caverns, it has much more energy capacity. Considering a pressure of 10MPa and a temperature of about 300 K, a CAES cavern roughly contains only about 4% of the energy stored inside a hydrogen cavern of the same size.

**Cons:**

- **Purity of the hydrogen:** When hydrogen absorbs moisture, bacteriological and chemical reactions may occur, modifying the gas's overall composition. A specific treatment to purify the hydrogen may be necessary (in addition to dehydration).
- **Geographical scarcity:** Not all countries have large salt deposits for this type of project. However, in Brazil, the pre-salt fields seem to be a promissory area for installing UHS sites.

Compared to other hydrogen storage types, salt caverns' feasibility is presented in Table 3.1 (+, 0, and - are good, medium, and poor, respectively). Salt caverns presented the best results in the comparison, including the always relevant economic point of view (CAPEX).

According to Zivar, Kumar, and Foroozesh (2021), UHS projects must correctly understand all the governing mechanisms throughout the lifetime of storage cycles. The withdrawal of stored hydrogen shall be constant to supply the market necessities at a high rate. They also point out that the considerable expertise from CO<sub>2</sub> storage can be used for hydrogen, as the structures and processes have some common points. Hévin (2019) selected some potential European locations to

install new UHS sites, as shown in Figure 3.3. Spain, France, the UK, Germany, and Romania are the most favorable countries.

Table 3.1– Comparison between UHS options, Zivar, Kumar, and Foroozesh (2021).

| Types<br>Characteristics   | Depleted<br>reservoirs | Aquifer | Salt caverns | Lined rock<br>caverns | Abandoned<br>mines |
|----------------------------|------------------------|---------|--------------|-----------------------|--------------------|
| Tightness                  | +                      | +       | +            | +                     | -                  |
| Flexibility                | 0                      | 0       | +            | 0                     | -                  |
| Gas mixing                 | -                      | -       | +            | +                     | +                  |
| Diffusion and<br>fingering | -                      | -       | +            | +                     | +                  |
| In-situ reactions          | -                      | 0       | +            | +                     | 0                  |
| Hydrogen<br>embrittlement  | -                      | -       | -            | -                     | -                  |
| CAPEX                      | +                      | 0       | 0            | -                     | 0                  |
| Standard<br>practice       | -                      | -       | 0            | -                     | -                  |

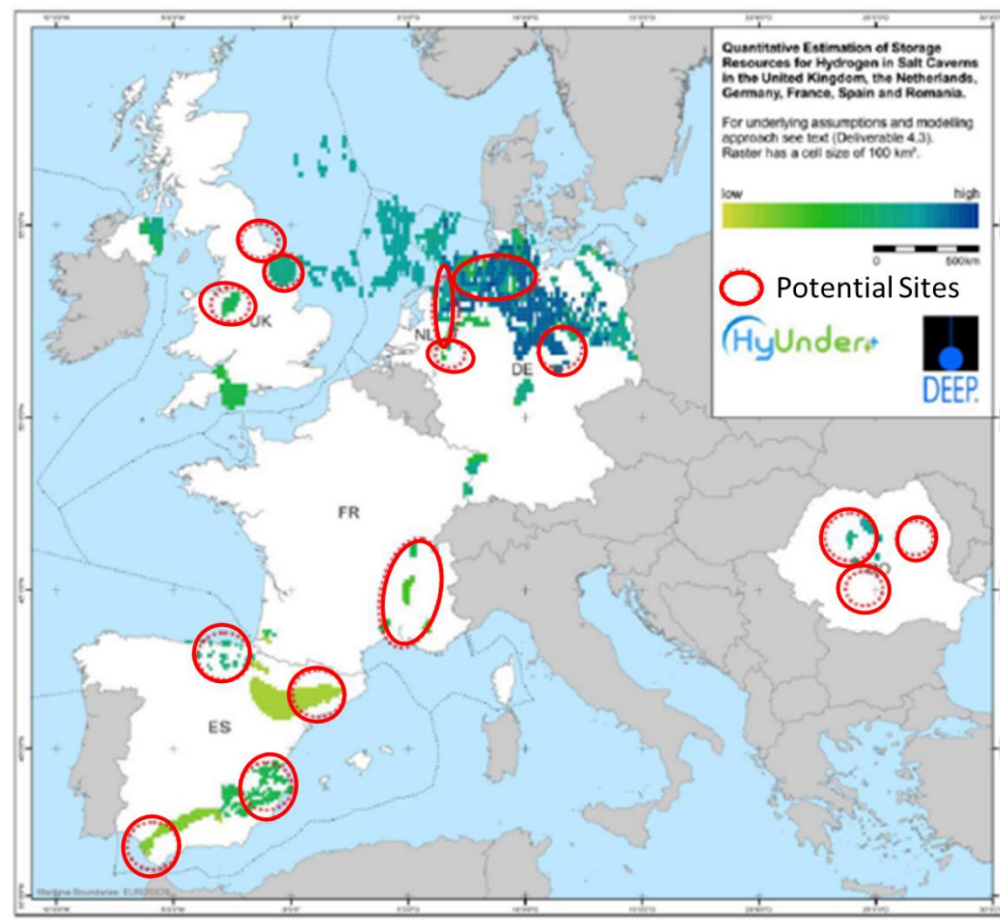


Figure 3.3 – Suggested European UHS sites, adapted from Hévin (2019).

Abdin et al. (2021) reported that the German government is funding an alliance (HYPOS alliance) of over 100 companies and institutions to build a salt cavern in the Central German Chemical Triangle Saxony-Anhalt with about 150,000 MWh of energy from wind power-generated hydrogen. Mitsubishi Power and Magnum Development have also launched the Advanced Clean Energy Storage Project in central Utah, USA, to build a storage facility for 1,000 MW/100,000 MWh of 100% green hydrogen storage in salt caverns. The gas utility Teréga and Hydrogène de France have started the HyGéo pilot project in French. It will store 1.5 GWh of energy, enough for 400 households for a year, CNBC (2020). Tractebel (2021) reported a partnership between Tractebel, DEEP.KBB GmbH, and PSE Engineering GmbH, resulted in an H<sub>2</sub> project to install offshore salt caverns in the North Sea.

In Brazil, Costa et al. (2011) discussed the great potential of the pre-salt Santos basin to be a future underground storage site. The Pre-Salt reservoirs have depths varying from 150-2200 m, and to achieve them, it is necessary to drill through 2000 m of salt rock, mainly halite, and in some places, with intercalations containing tachyhydrite and carnallite. The creep strain rate of these rocks is approximately two orders of magnitude higher than halite's rate, considering equal conditions of temperature and pressure. Figure 3.4 shows a structure map of an area in Santos basin.

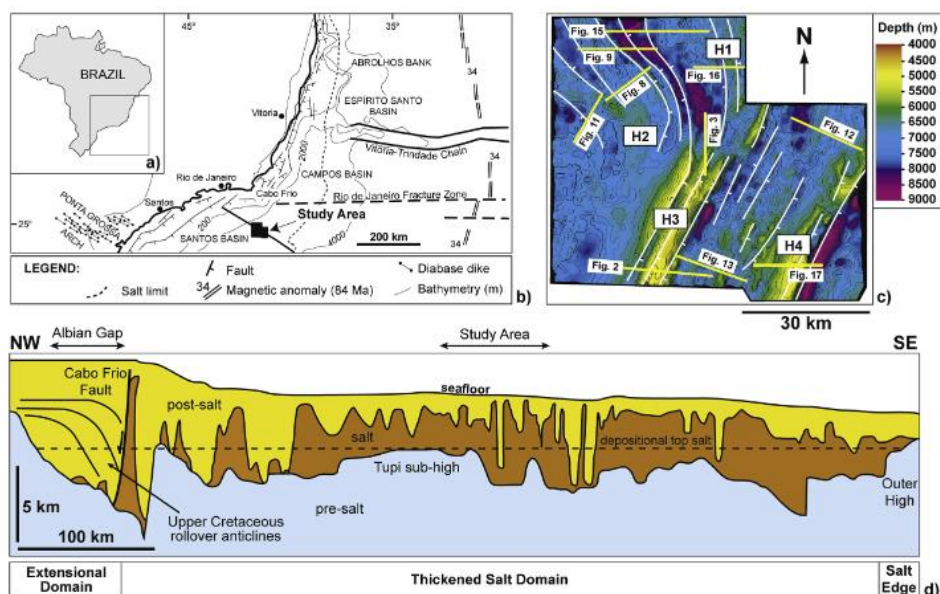


Figure 3.4 – Structure map of an area in Santos basin, Alves et al. (2017).

Costa (2015) and Costa et al. (2019) studied the viability of installing salt caverns for CO<sub>2</sub> in Brazilian salt caverns. Studies involved numerical analysis, geological, technical, and operational aspects. Figure 3.5 shows the proposed salt cavern for the Brazilian gas project.

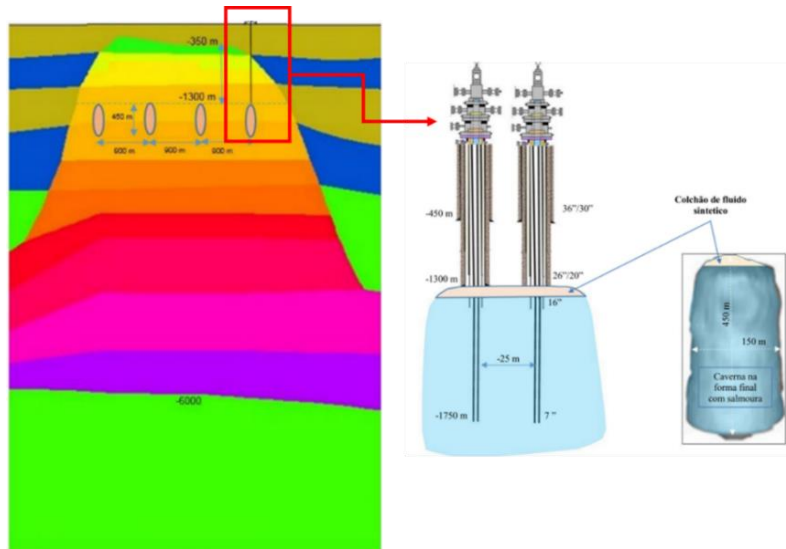


Figure 3.5 – Proposed salt caverns for CO<sub>2</sub> storage in Brazilian pre-salt, Costa (2015).

For this reason, considering the Brazilian scenario, the pre-salt fields seem to be the ideal location for installing UHS sites, as indicated in Figure 3.6 (red color). These areas are placed along the continental shelf of South America and contain a significant fraction of the world's oil and gas reserves. Most of the salt areas were formed during the Cretaceous geological area.

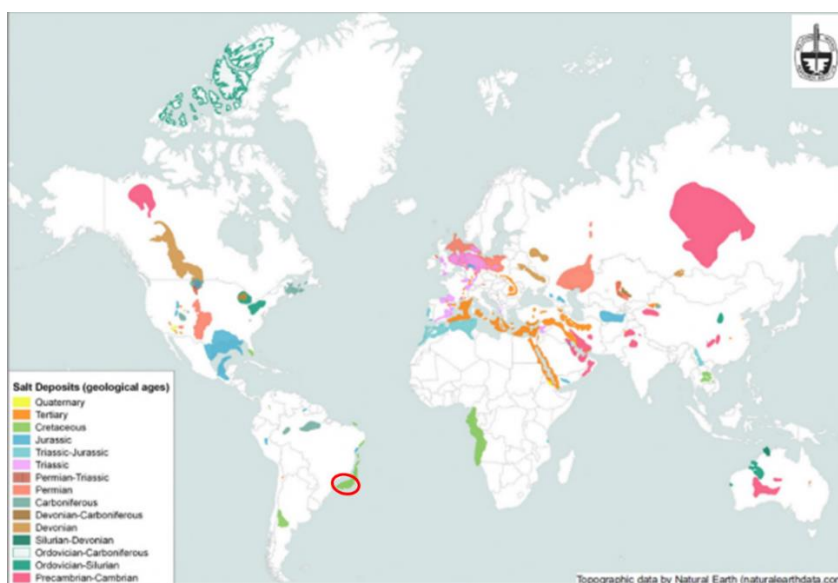


Figure 3.6 – Proposed salt caverns for H<sub>2</sub> storage in Brazilian pre-salt (Hévin 2019).

De Almeida et al. (2010) highlights the Santos basin as one of the best areas to explore in the pre-salt fields, including installing salt caverns. Considering the previous literature (Costa et al., 2011, 2015, 2019), this thesis will focus on the simulation of a UHS site in the Santos basin.

### **3.2.2. Construction of a salt cavern**

A salt cavern is subjected to different loading conditions during construction and operation. Consequently, the region presents different loading rates that must be well understood and predicted to guarantee safe conditions. Despite the particularities of storing each type of material, the solution mining process can be described by the following stages:

- Stage I - Drilling the salt deposit: A borehole is drilled up to the cavern's bottom. Two leaching pipes are concentrically suspended and inserted into the hole in the sequence. According to the material storage and geological conditions drilling depth may vary from 300 to 2000 m. This stage finishes with the cementation from the ground surface to the casing-shoe;
- Stage II – Leaching: Freshwater is injected through the leaching pipes. The water dissolves the salt, and the mixture (brine) goes to the ground surface. According to Khaledi et al. (2016), there are two different leaching modes: a) Direct leaching process: the freshwater runs through the inner leaching pipe, and the produced brine is transferred to the ground surface via the outer pipe; b) Indirect leaching: the brine runs through the inner leaching pipe, and the freshwater is injected into the rock salt medium via the outer pipe. The leaching time could range from one year to a few years. Modern techniques can reduce the leaching time (Peng et al. 2023).
- Stage III – Debrining: The brine still inside the cavern is displaced by injecting gas. The gas is injected through the outer pipe, and the brine goes out via the inner leaching pipe. The pipes are removed after this stage. It takes just a few months to extract the brine from the cavern;

- Stage IV – First filling: The pressure inside the cavern is reduced to the minimum required. Then, the cavern is ready for the cyclic loading operation. The time required for this phase could range from some hours to a few days.
- Stage IV – Operation: The cyclic pressure inside the cavern starts. It fluctuates within a predefined range due to the injection and withdrawal of storage products. For hydrogen caverns, these cycles last just a few days or weeks, as the market demands (Böttcher et al. 2017; Peng et al. 2023). Zivar, Kumar, and Foroozesh (2021) warn that the injected hydrogen should be monitored throughout the project. Furthermore, the hydrodynamic, geochemical, and microbial activities must be constantly checked to avoid loss of hydrogen or affecting its purity. Another relevant point is the efficiency of the withdrawal cycles. The operational stage will be detailed in the next chapter. Figure 3.7 shows the process of salt cavern construction:

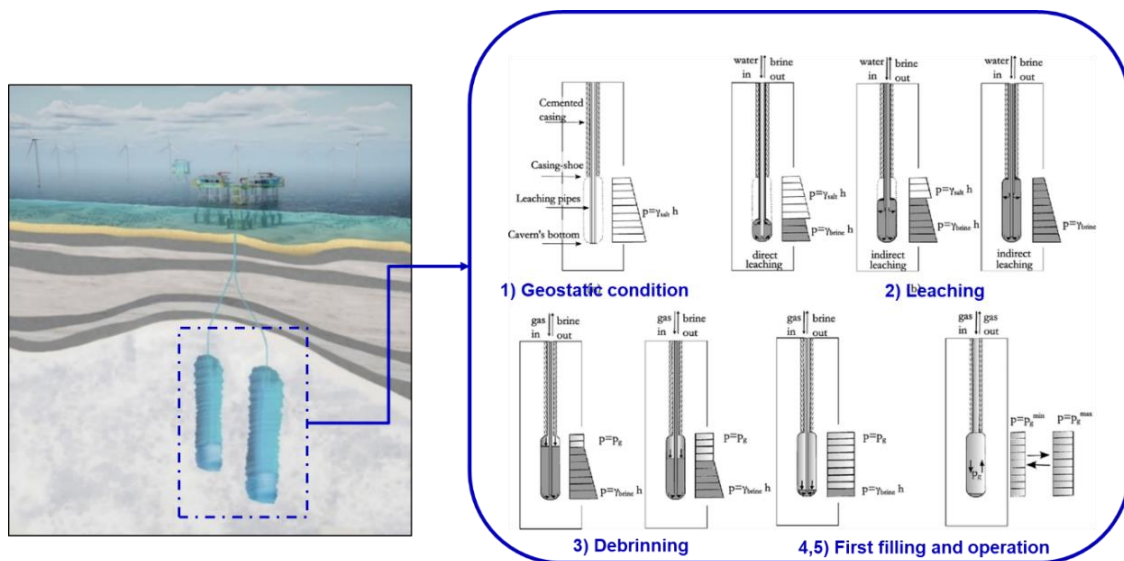


Figure 3.7 – (1) initial phase, geostatic condition (2) leaching phase, excavation using solution mining technique (3) debrining phase (4,5) first filling and cyclic loading operation, variation of the internal pressure within a predefined range, adapted from Khaleli et al. (2016).

Once the principal aspects of hydrogen in salt caverns are covered in this chapter, the next steps are related to numerical analysis and discussion of the first results considering a salt cavern in the Brazilian pre-salt (Santos Basin).

## 4 Workflow for cavern integrity analysis

The cavern integrity analysis follows a workflow that contemplates cavern geometry, identifying the repository properties, definition of allowable pressures and temperature amplitudes, constitutive models, safety criteria adopted, and the necessary time to inject and discharge the gas. All the mentioned topics are important to assure long-term stability. This chapter comprises the paper published by Dias et al. (2023).

### 4.1.Cavern geometry

Identifying the actual cavern geometry is not easy, as the sonar accuracy is typically 1%, according to Brouard et al. (2013). A three-dimensional cavern shape measured by a sonar was presented by Liu et al. (2020):

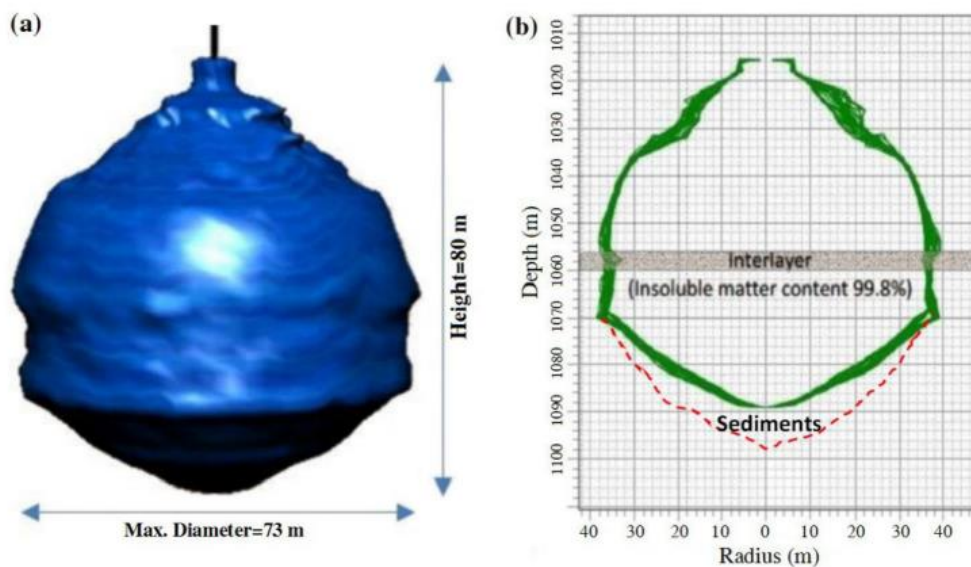


Figure 4.1 – Three-dimensional cavern shape, Liu et al. (2020).

It has roughly an ellipsoid shape, a total height of 80 m, and a maximum diameter of 73 m. However, the literature commonly simplifies the cavern shape when the sonar data is unavailable, sometimes adopting a capsular shape or circular geometries (Costa et al. 2011; Khaledi et al. 2016; Böttcher et al. 2017; Firme et al. 2019). In this proposal, we consider the capsular shape shown in Figure 4.2.

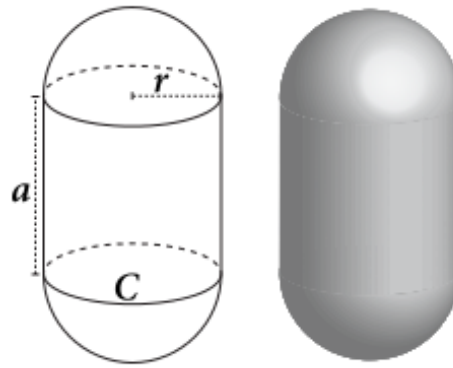


Figure 4.2 – Capsular shape adopted for the UHS salt cavern.

where  $a = 200$  m and  $r = 50$  m, the same dimensions presented in Firme, Roehl, and Romanel (2019). The volume  $V$  of a capsule is calculated by adding the volume of a ball of radius  $r$  (that accounts for the two hemispheres) to the volume of the cylindrical part. Hence, if the cylinder has a height “ $a$ ”:

$$V = \frac{4}{3}\pi r^3 + (\pi r^2 a) = \pi r^2 \left( \frac{4}{3}r + a \right) \quad (4.1)$$

and the surface area of a capsule

$$S = 2\pi r(2r + a) \quad (4.2)$$

Considering the adopted dimensions, the salt cavern has a volume of approximately  $2,090,000 \text{ m}^3$  and an area of  $94,250 \text{ m}^2$ . More complex shapes, such as irregular ones, will be verified in chapter five.

#### 4.2. Initial stress state and temperature (geostatic conditions)

The initial stress state assumes a representative scenario of the Brazilian Pre-salt deep-water environments consist of an offshore basin sited in a region where the water depth is 2,000 m. The rock formation considers a 700 m overburden followed by 1,000 m of salt (halite), where the cavern is hosted. The hypothesis of a significant horizontal continuity throughout the cavern's immediate surroundings is also adopted (salt-bedded region) - Firme et al. (2019). The cavern is situated within the interval of -3,050 to -3,350 m inside the halite layer. The slab protection at the top of the cavern is 350 m. The axisymmetric model is represented in Figure 4.3.

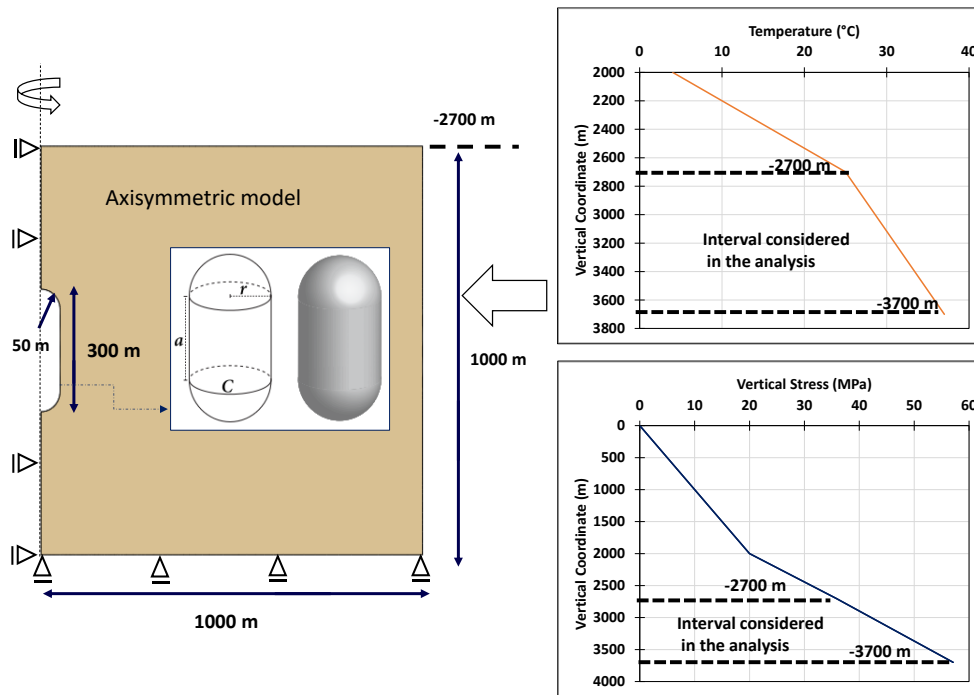


Figure 4.3 – Axisymmetric model of the salt cavern.

The geostatic stresses are isotropic ( $S_V = S_H = S_h$ ) and are assigned by the superposition of the gravitational loads ensuring the model initializes with null deformations. The overburden's specific weight is constant,  $22.56 \text{ kN/m}^3$  (Firme et al. 2015). The salt rock specific weight is  $21.30 \text{ kN/m}^3$  (Poiate 2012; Firme et al. 2016). The temperature is evaluated with the following geothermal gradients:  $30^\circ\text{C/km}$  for sedimentary rocks and  $12^\circ\text{C/km}$  for salt rock - Costa et al. (2015). The temperature of the sea bed is  $4^\circ\text{C}$ .

### 4.3. Gas pressure and temperature

The gas pressure and temperature follow the diabatic analytical solution presented by Xia et al. (2015), initially considered for CAES caverns. The authors point out two methods to evaluate the thermodynamic response: a) the adiabatic method and b) the diabatic method considering the heat exchange between cavern air and the surrounding rock. However, the adiabatic method ignores the heat exchange between cavern air and the surrounding rock, leading to more significant temperature and pressure amplitudes, more than the real ones. On the other hand, the diabatic method considers heat exchange and can accurately predict the thermodynamic response of caverns.

This solution assumes that the gas density in the cavern is constant at a given time step and that heat diffusion into the rock salt occurs fast. Likewise, air leakage is ignored when the surrounding rock is salt or low-permeability rock. From the mass conservation equation:

$$V \frac{d\rho}{dt} = \dot{m}_i(t) + \dot{m}_e(t) \quad (4.3)$$

where  $\rho$  is the gas density,  $\dot{m}_i(t)$  and  $\dot{m}_e(t)$  are a function of the injected and withdrawn air mass flow rate, respectively. The energy conservation equation is given by equation (4.4):

$$\begin{aligned} V\rho c_v \frac{dT}{dt} = & \dot{m}_i(t) \left( h_i - h + ZRT - \rho \left. \frac{\partial u}{\partial \rho} \right|_T \right) \\ & + \dot{m}_e(t) \left( ZRT - \rho \left. \frac{\partial u}{\partial \rho} \right|_T \right) + \dot{Q} \end{aligned} \quad (4.4)$$

here,  $V$  is the cavern volume,  $c_v$  is the constant volume-specific heat,  $h_i$  is the specific enthalpy of injected air,  $h$  is the specific enthalpy of air,  $u$  is the specific internal energy of air,  $Z$  is the air compressibility,  $R$  is the specific air constant, and  $\dot{Q}$  is the convective heat transfer rate. The generalized gas state equation is:

$$p = Z\rho RT \quad (4.5)$$

The heat convection at the cavern walls:

$$\dot{Q} = h_c A_c (T_{RW} - T) \quad (4.6)$$

where  $h_c$  is the heat transfer coefficient,  $A_c$  is cavern wall surface area, and  $T_{RW}$  is the cavern wall surface temperature. The heat conduction in the surrounding rock is expressed by

$$\rho_R c_{pR} \frac{dT_R}{dt} = \frac{1}{r} \frac{\partial}{\partial r} \left( k_R r \frac{\partial T_R}{\partial r} \right) \quad (4.7)$$

with  $\rho_R$ ,  $c_{pR}$ ,  $k_R$ , and  $T_R$  as the rock density, constant pressure specific heat, thermal conductivity, and temperature. The following boundary conditions are adopted:

$$\begin{aligned} r = R_w, & -k_R r \frac{\partial T_R}{\partial r} = h_c (T - T_{RW}) \\ r \rightarrow \infty, & T_R = T_0 \end{aligned} \quad (4.8)$$

The air mass flow rate into the cavern is defined as positive; otherwise, it is negative. The variation of  $\dot{m}_i(t)$  and  $\dot{m}_e(t)$  for a cavern operation is shown in Figure 4.4.

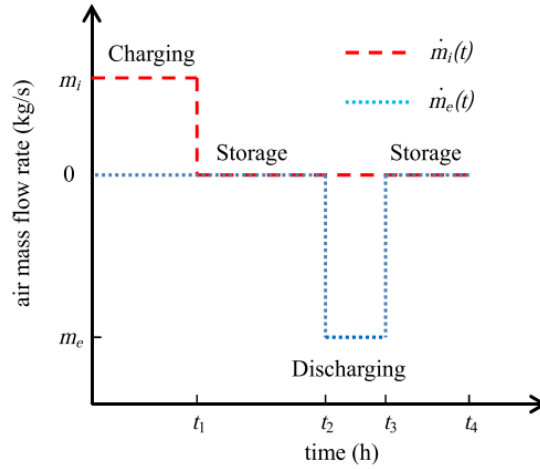


Figure 4.4 – Air mass flow rate for a cavern, Xia et al. (2015).

Xia et al. (2015) explain that the air temperature and pressure need the simultaneous solution of the equations presented above, which implies complex numerical computations. Considering the assumptions early mentioned and that a constant average value can represent the cavern air density ( $\rho_{AV}$ ) when the ratio of injected air mass to the initial cavern air mass  $m_r$  is small, we have:

$$V\rho_{AV}c_v \frac{dT}{dt} = \dot{m}_i(t)(h_i - h + RT) + \dot{m}_e(t)RT + h_c A_c (T_{RW} - T) \quad (4.9)$$

In a given period (charging, discharging, or storage), the value of the function  $\dot{m}_i(t)$  is a constant (either  $m_i$  or 0, as shown in Figure 4.4) and  $\dot{m}_e(t)$  is a constant too (either  $m_e$  or 0). The equation (4.9) becomes:

$$T = (T_0 + \alpha)e^{\beta(t-t_0)} - \alpha \quad (4.10)$$

where  $\alpha$  and  $\beta$  are charging and discharging coefficients, respectively. Thus:

$$\begin{aligned}
& \left( \frac{m_i c_p T_i + h_c A_c T_{RW}}{m_i (R - c_p) - h_c A_c} \right), t_0 \leq t \leq t_1 \text{ (charging period)} \\
\alpha = & \quad -T_{RW}, t_1 < t \leq t_2 \text{ (storage period)} \\
& \quad \frac{h_c A_c T_{RW}}{m_e R - h_c A_c}, t_2 < t \leq t_3 \text{ (discharging period)} \\
& \quad -T_{RW}, t_3 < t \leq t_4 \text{ (storage period)} \\
& \quad \frac{m_i (R - c_p) h_c A_c}{V \rho_{AV} c_v}, t_0 \leq t \leq t_1 \text{ (charging period)} \\
\beta = & \quad \frac{-h_c A_c}{V \rho_{AV} c_v}, t_1 < t \leq t_2 \text{ (storage period)} \\
& \quad \frac{m_e R - h_c A_c}{V \rho_{AV} c_v}, t_2 < t \leq t_3 \text{ (discharging period)} \\
& \quad \frac{-h_c A_c}{V \rho_{AV} c_v}, t_3 < t \leq t_4 \text{ (storage period)}
\end{aligned} \tag{4.11}$$

The present work calculated the thermodynamic and hydrogen transport properties using the REFPROP package (Lemmon et al. 2018). The gas properties are obtained through a link with REFPROP, which updates the pressure and temperature at step n+1. The material properties of salt rock and parameters for the thermodynamic analysis are presented in Table 4.1 (Xia et al. 2015; Böttcher et al. 2017; Zhu et al. 2017). The inputs from the thermodynamical simulator were fed into the GeMA Framework (Teixeira Mendes et al. 2016), an in-house multiphysics simulator based on the finite element method.

Table 4.1– Material properties for salt rock and parameters for the analytical.

| Parameter                     | Unit                              | Value                |
|-------------------------------|-----------------------------------|----------------------|
| Density                       | kg.m <sup>-3</sup>                | 2040                 |
| Thermal Conductivity          | Wm <sup>-1</sup> K <sup>-1</sup>  | 7                    |
| Thermal expansion coefficient | K <sup>-1</sup>                   | 4 x 10 <sup>-5</sup> |
| Specific heat capacity        | Jkg <sup>-1</sup> K <sup>-1</sup> | 880                  |
| Heat transfer coefficient     | Wm <sup>-2</sup> K <sup>-1</sup>  | 1.2                  |
| Cavern surface area           | m <sup>2</sup>                    | 94,250               |
| Cavern volume                 | m <sup>3</sup>                    | 2,090,000            |
| Injection temperature         | K                                 | 333                  |

Usually, the literature sets a pressure range for the analysis, approximately 30-90% of the lithostatic stress at the top of the cavern (Costa et al. 2015, 2019; Liu et al. 2020). In this study, the gas pressure will be controlled by the lower limit of 30% and 80% for the upper limit to minimize the risks of rock fracturing. If the temperature amplitude leads the pressure to exceed this range, the cycle duration, injection pressure/temperature, and gas flow mass injected/discharged will be re-evaluated. Figure 4.5 shows a flowchart for a complete cycle calculation:

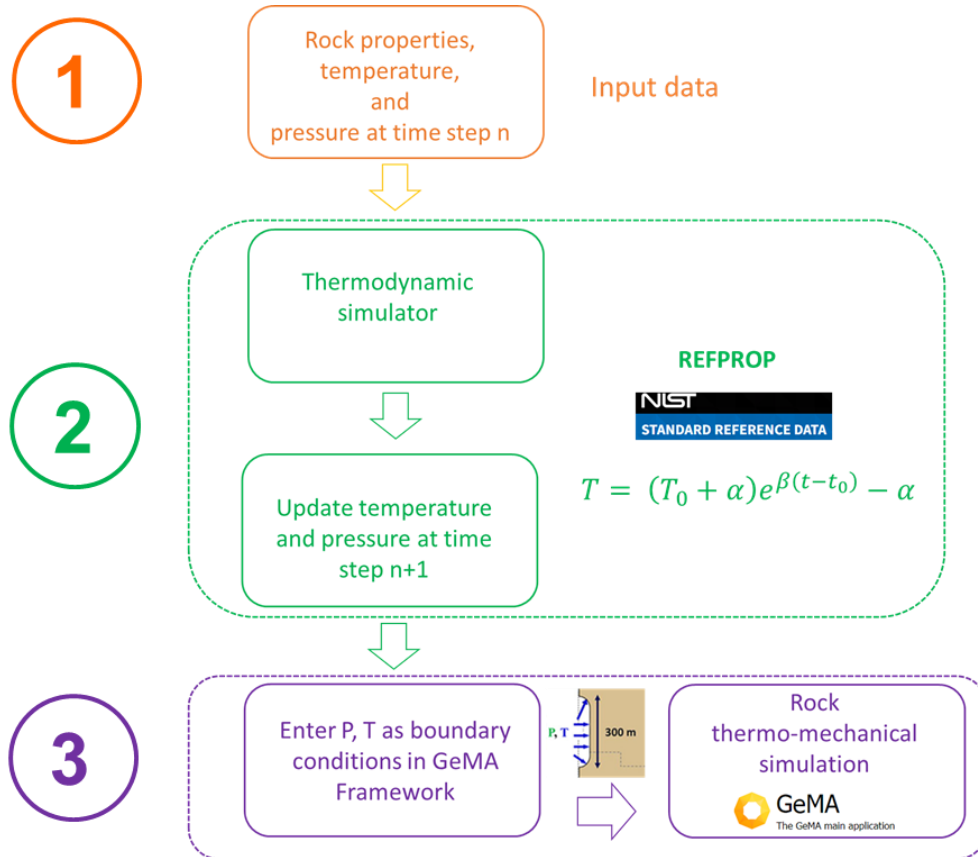


Figure 4.5 – Complete gas temperature and pressure calculation during a cycle.

Regarding the thermomechanical coupling, the incremental total strain  $\Delta\epsilon$  is given by:

$$\Delta\epsilon = \Delta\epsilon_m + \Delta\epsilon_T \quad (4.12)$$

Where  $\Delta\epsilon_m$  represents the increment of mechanical strain,  $\Delta\epsilon_T = \mathbf{m}\alpha_T\Delta T$  is the increment of thermal strain,  $\alpha_T$  stands for the thermal expansion coefficient and  $\mathbf{m} = \{1 \ 1 \ 1 \ 0 \ 0 \ 0\}$ . The soil constitutive behavior considering thermal effects results in the following:

$$\Delta\boldsymbol{\sigma} = \mathbf{D}\Delta\boldsymbol{\varepsilon} - \mathbf{D}\mathbf{m}\alpha_T\Delta T \quad (4.13)$$

$\Delta\boldsymbol{\sigma}$  is the increment of total stress, and  $\mathbf{D}$  is the elastic constitutive matrix. The last term on the right-hand side of equation (4.13) represents the change in total stress induced by temperature variation, which is the thermal effect on the mechanical equilibrium. Following the standard FEM procedure, the equilibrium equation for a coupled thermomechanical behavior of the soil results in:

$$\mathbf{K}_G\Delta\mathbf{u} - \mathbf{M}_G\Delta T = \Delta\mathbf{R}_G \quad (4.14)$$

$\mathbf{K}_G$  represents mechanical stiffness matrix,  $\mathbf{M}_G$  is the TM coupling term, and  $\Delta\mathbf{R}_G$  is the residual force vector.

$$\mathbf{K}_G = \sum_{i=1}^N \left( \int_{\Omega} \mathbf{B}^T \mathbf{D} \mathbf{B} d\Omega \right)_i \quad (4.15)$$

$$\mathbf{M}_G = \sum_{i=1}^N \left( \int_{\Omega} \mathbf{B}^T \mathbf{D} \mathbf{m} \mathbf{N}_T d\Omega \right)_i \quad (4.16)$$

Where  $\mathbf{B}$  is the matrix that relates the nodal displacement and mechanical strains,  $\mathbf{N}_T$  is the vector containing shape functions to interpolate the temperature field. Neglecting radiation and the mechanical effect on the thermal system, the governing equation of heat transfer in soils follows the law of energy conservation:

$$\rho C_p \Delta T = \nabla \cdot (k_T \nabla T) + G \quad (4.17)$$

$k_T$  is the thermal conductivity,  $\rho$  is the soil density,  $C_p$  represents the specific heat capacity, and  $G$  indicates the heat generation rate. Applying the standard Galerkin method, the finite element equation governing the heat transfer can be assembled in terms of global matrices as:

$$\mathbf{C}_G \partial T / \partial t + \boldsymbol{\Phi}_G \Delta T = \mathbf{Q}_G \quad (4.18)$$

Where  $\mathbf{C}_G$  represents the thermal expansion matrix,  $\boldsymbol{\Phi}_G$  is the conductivity and advection capacity matrix and  $\mathbf{Q}_G$  stands for the heat source or sink matrix.

$$\Phi_G = \sum_{i=1}^N \left( \int_{\Omega} \mathbf{B}_T^T \mathbf{k}_T \mathbf{B}_T d\Omega + \int_{\Gamma} h \mathbf{N}_T^T \mathbf{N}_T d\Gamma \right)_i \quad (4.19)$$

$$\mathbf{C}_G = \sum_{i=1}^N \left( \int_{\Omega} \rho C_p \mathbf{N}_T^T \mathbf{N}_T d\Omega \right)_i \quad (4.20)$$

Here,  $h$  is the convection coefficient. Assembling equation (4.14) and equation (4.18) gives the coupled TM equation system:

$$\begin{bmatrix} \mathbf{0} & \mathbf{0} \\ \mathbf{0} & \mathbf{C}_G \end{bmatrix} \begin{Bmatrix} \partial \mathbf{u} / \partial t \\ \partial T / \partial t \end{Bmatrix} + \begin{bmatrix} \mathbf{K}_G & -\mathbf{M}_G \\ \mathbf{0} & \Phi_G \end{bmatrix} \begin{Bmatrix} \Delta \mathbf{u} \\ \Delta T \end{Bmatrix} = \begin{Bmatrix} \Delta \mathbf{R}_G \\ \mathbf{Q}_G \end{Bmatrix} \quad (4.21)$$

#### 4.4. Constitutive model for creep

This study adopts the Double-Mechanism creep model for the analysis. According to Costa et al. (2011), it simplifies the equation developed by Munson in the Multi-mechanism model. It considers the creep mechanisms dislocation glide and undefined mechanism. The formulation for this constitutive model is:

$$\dot{\varepsilon} = \varepsilon_0 \left( \frac{\sigma_{ef}}{\sigma_0} \right)^n e^{\left( \frac{Q}{RT_0} - \frac{Q}{RT} \right)} \quad (4.22)$$

The material parameters were already explained during the constitutive model discussion in Chapter 3. These sensitive material parameters for Brazilian halite have been calibrated based on triaxial creep tests carried out by Poiate (2012), and they are listed in Table 4.2.

Table 4.2– Properties of the Brazilian halite (Poiate 2012).

| Parameter                              | Unit            | Value                   |
|--|-----------------|-------------------------|
| Young's modulus                        | GPa             | 25.37                   |
| Poisson's ratio                        | -               | 0.36                    |
| Thermal activation energy              | J/mol           | 50,160                  |
| Universal gas constant                 | J/mol.K         | 8.314                   |
| Threshold creep rate                   | h <sup>-1</sup> | 1.88 x 10 <sup>-6</sup> |
| Threshold deviatoric stress            | MPa             | 9.91                    |
| Threshold temperature                  | K               | 359.15                  |
| Stress power for dislocation creep     | -               | 3.36                    |
| Stress power for steady-state cracking | -               | 7.55                    |

Regarding the primary creep, Costa et al. (2011) point out that it is fully dissipated quickly and can be absorbed by the initial deformation predicted in the numerical models. The tertiary creep model is not considered, but the dilatancy effect (damage due to high volumetric expansion) will be represented by the dilatancy boundaries found in the literature.

#### 4.5. Safety criteria

Böttcher et al. (2017) highlight the most common safety criteria for underground salt caverns in the literature. They are:

- 1) The material condition must not violate the dilatancy criterion.
- 2) No cyclic failure due to loading pattern;
- 3) No tensile stresses around the cavern;
- 4) Gas pressure must not exceed the least compressive stress.
- 5) Reduced cavern convergence, below 20%;
- 6) Limited ground subsidence.

In this thesis, we adopted the criteria 1), 3), 4), and 5) to monitor the cavern safety. Regarding the rock dilatancy, we selected van Sambeek, Ratigan, and Hansen (1993) as the boundary to check the dilatancy behavior (dilatancy index) since it is one of the most utilized salt rock projects (Costa et al. 2005, 2006, 2011; Poiate 2012; Firme et al. 2014).

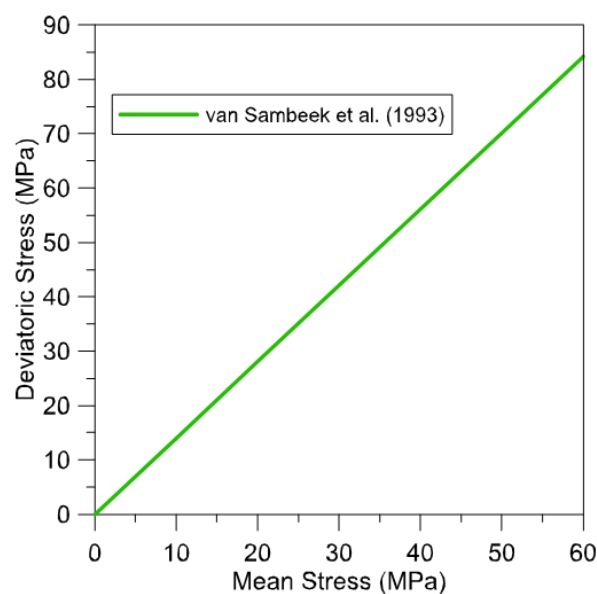


Figure 4.6 – Van Sambeek, Ratigan, and Hansen (1993) dilatancy boundary.

To evaluate if dilatancy occurs, we propose a dilatancy index (DI), the ratio between the von Mises equivalent stress obtained from the simulations ( $\sigma_d$ ) and the maximum deviatoric stress according to the dilatancy boundary ( $\sigma_{d-Sambeek}$ ). Thus:

$$DI = \frac{\sigma_d}{\sigma_{d-Sambeek}} \quad (4.23)$$

If the index achieves 1.0, the current stress state reaches the dilatancy boundary, and dilatancy occurs. For cavern safety, keeping DI below 1.0 is recommended (0.8-0.9, for instance).

#### 4.6. Load conditions before the cyclic operation

Despite the different case studies that will be carried out in this research, they all have common steps until the beginning of the cyclic operation. These steps are a) geostatic equilibrium, b) leaching, c) debrining, and d) first filling. In geostatic equilibrium, the model remains with the initial stress and temperature conditions presented in section 4.2. We adopt the fixed node methodology to ensure the equilibrium: all nodes are fixed, and the correspondent reactions are applied to nullify the displacements. Figure 4.7 shows the geostatic equilibrium with this methodology.

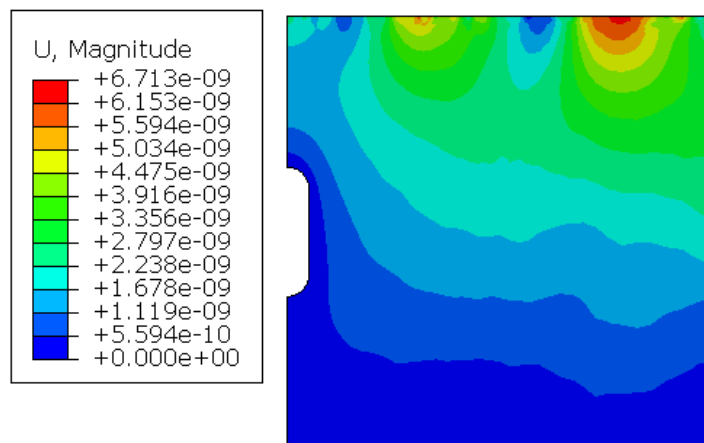


Figure 4.7 – Geostatic equilibrium with very low displacements (in meters).

Figure 4.8 shows a schematic representation of the simulation steps b) to d) and their assumptions.

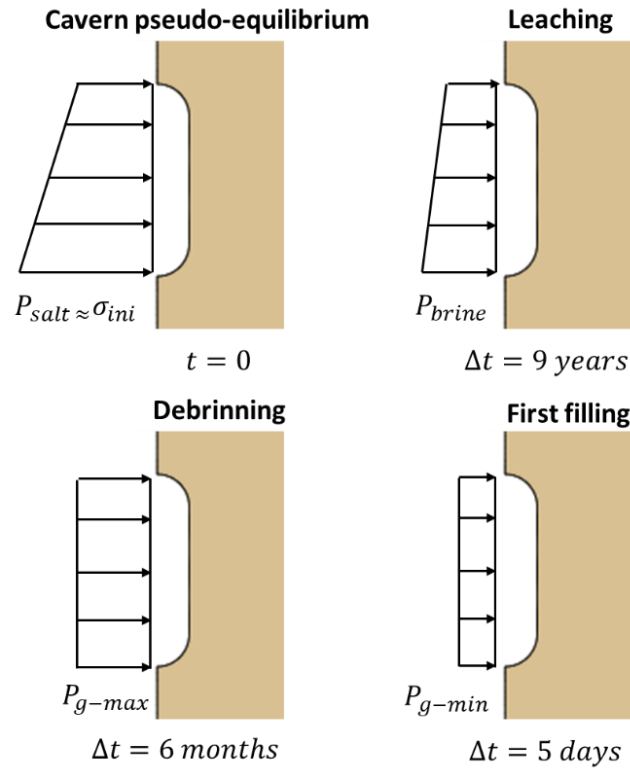


Figure 4.8 – Simulation steps and their assumptions.

Cavern pseudo-equilibrium represents an equivalent fluid pressure ( $P_{salt} = 21.30 \text{ kN/m}^3$ ) being applied upon the cavern walls to maintain the pre-existing stress state ( $\sigma_{ini}$ ) after the removal of the elements (no deviatoric stress). In the sequence, the leaching step corresponds to the salt cavern excavation, freshwater injection, and a mixture (brine) formation. The unit weight adopted in the salt-equivalent fluid pressure ( $P_{salt}$ ) is reduced from  $21.30 \text{ kN/m}^3$  (salt) to  $12 \text{ kN/m}^3$  (brine) over time, considering a realistic solution mining rate. From Khaledi et al. (2016), we considered an average dissolution rate of  $26.5 \text{ m}^3/\text{h}$ , which takes approximately nine years to complete the process. We highlight that there are more advanced techniques to reduce the leaching time, for example, high-speed levels of water injection (above  $300 \text{ m}^3/\text{h}$ ) or different techniques, such as multiple wells to water injection (Chromik and Korzeniowski 2021; Peng et al. 2023). However, as the results in this stage were less critical, the average dissolution rate ( $26.5 \text{ m}^3/\text{h}$ ) was maintained.

The next step is related to debrining, when the gas starts to be injected into the salt cavern, replacing the existing brine. Here, the control of hydrogen purity and chemical reactions gains relevance. The brine hydrostatic load ( $P_{brine}$ ) turns into a uniform load ( $P_{g-max}$ ) when the process is completed. This stage is less

time-consuming (in months) and was assumed to take six months (Khaledi et al. 2016b; Firme et al. 2019). The last step is the first filling, when the gas pressure is reduced from the maximum pressure ( $P_{g-max}$ ) to the minimum pressure ( $P_{g-min}$ ). We assumed that this stage lasts five days - Khaledi et al. (2016). Regarding the thermomechanical (TM) analysis, it is considered that temperature variation will only occur in the first filling stage due to the cavern's depressurization. Thereby, the simulation is basically mechanical until this stage.

#### 4.7.Cyclic operation

In order to better understand the effect of cyclic operation regarding the temperature and pressure amplitudes, we selected five case studies that are summarized in Table 4.3.

Table 4.3– Case studies considered in the simulations.

| Case study | Description                             |
|------------|---|
| 1          | 80-day cycle – Mechanical only          |
| 2          | 80-day cycle - TM                       |
| 3          | 20-day cycle - TM                       |
| 4          | 20-day cycle with reduced pressure - TM |
| 5          | 320-day cycle - TM                      |

The cycle duration was determined to cover long and short supply periods (Böttcher et al. 2017; Abreu et al. 2023; Peng et al. 2023). The hydrogen to be stored in the salt cavern is expected to come from a sustainable process – green hydrogen production. In Brazil's first years of technology implementation, case 5 is expected to be dominant. However, the country can soon assume leadership in hydrogen storage with the support of the expertise acquired from the exploration into ultra-deep waters and the demand for renewable energies in South America. In this scenario, medium and short periods will be a reality, and cases 1 to 4 require investigation.

Case 1 is a mechanical analysis used as a reference for case 2, a TM simulation with the same cycle time to evaluate how temperature affects cavern creep and its safety. Case 3 represents a short cycle (four times shorter than case 2). Cavern closure is expected to increase, and the safety criteria will become more

relevant. In case 4, the injection pressure drops from 80 % to approximately 70 % of the lithostatic pressure at the cavern top. The objective of this case study is to evaluate the impact of pressure reduction on the temperature amplitudes and, consequently, the rock integrity. The last case study has a long-term cycle. Thus, the results are expected to be less critical. Figure 4.9 shows the gas pressure (case studies 1 and 2) and temperature (case studies 2 to 4).

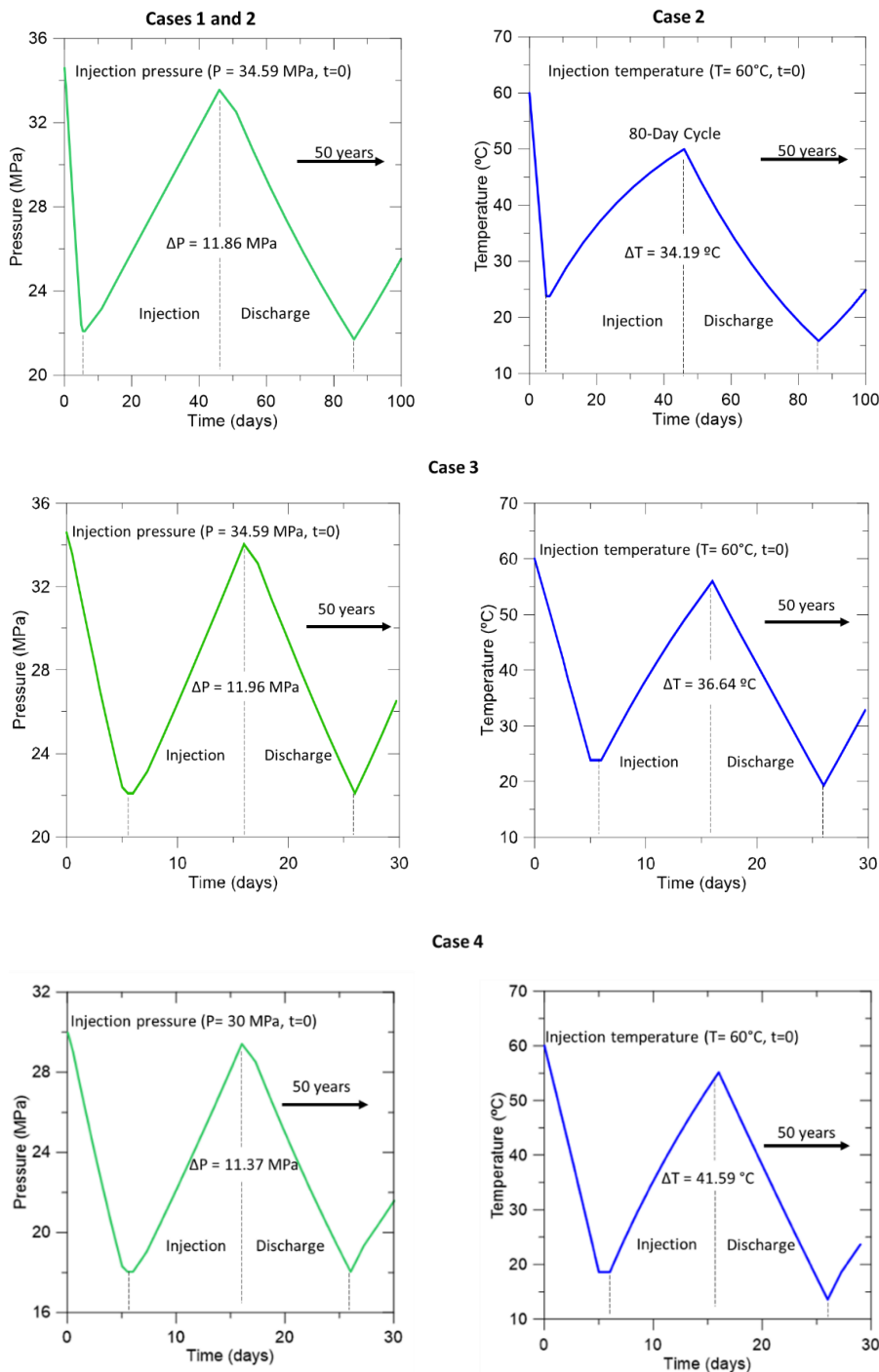


Figure 4.9 – Gas pressure and temperature for case studies 1 to 4.

Figure 4.10 shows the gas pressure and temperature for case study 5.

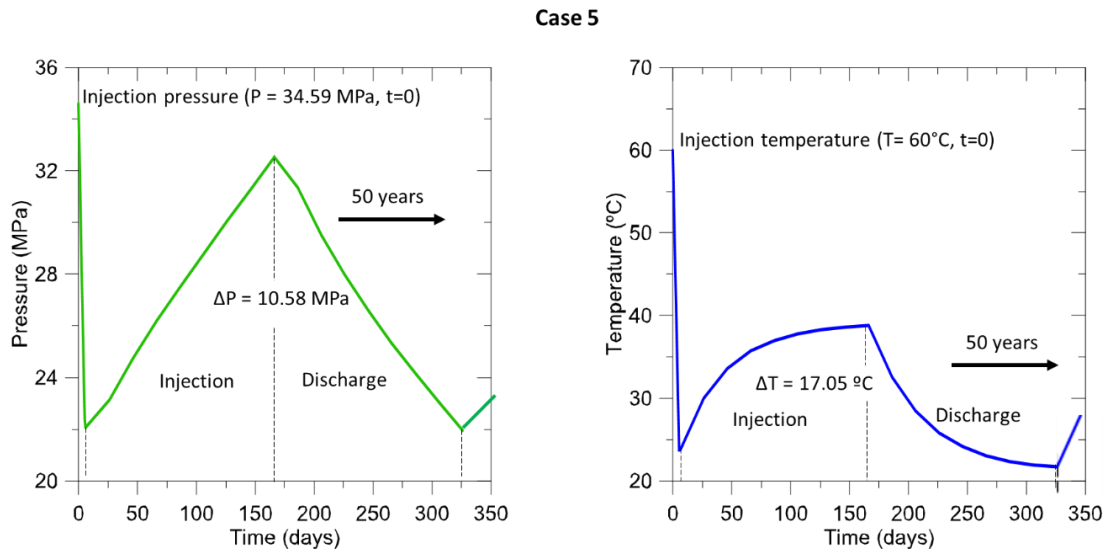


Figure 4.10 – Gas pressure and temperature for case study 5.

#### 4.8. Permeability measurement

The low permeability of the salt rock is important to guarantee the safety and tightness of the caverns. Zivar et al. (2021) pointed out that due to the lower density, viscosity, and molecule size of hydrogen, the leakage issue and hence the loss of hydrogen is common and severe.

According to Peach's (1991) laboratory measurements, salt has a very low permeability, in the order of  $10^{-20}$  m<sup>2</sup> or less. However, if dilatancy occurs, the permeability is expected to increase, and the sealing may be compromised. In this context, correctly assessing operational pressures and temperature is crucial for maintaining the cavern's safety.

The literature has presented studies during the past decades that attempt to predict the evolution of salt rock permeability (Peach 1991; Chan et al. 2001; Schulze et al. 2001; Alkan 2009). This research will adopt the criterion proposed by Peach (1991), where the permeability is expressed as a power function of the volumetric strains – equation (4.24):

$$k = \alpha \varepsilon_{vol}^{\beta} \quad (4.24)$$

where  $\alpha = 2.13 \times 10^{-8}$  and  $\beta = 3.0$ . The permeability evolution is shown in Figure 4.11.

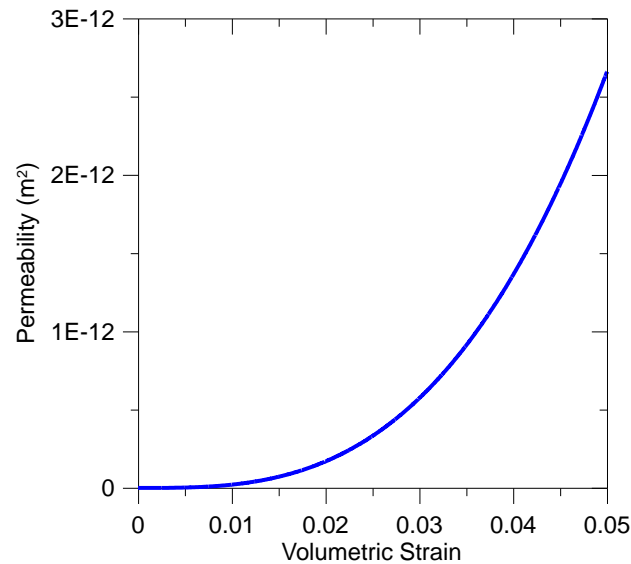


Figure 4.11 – Permeability evolution in salt rock according to Peach's (1991) criterion.

The permeability measured in this study refers only to salt rock damage without considering further interaction with the medium, such as dissolution. The gas/rock interaction and how it affects the rock's mechanical and hydraulic properties requires considering coupled hydromechanical or chemical effects.

#### 4.9. Simulation summary

The flowchart below resumes the cavern's construction and operation steps discussed in the previous topics. We emphasize that the last item (interventions) occurs when the cavern's integrity is not guaranteed. In this case, the operator must act to avoid significant risks to the project and the environment.

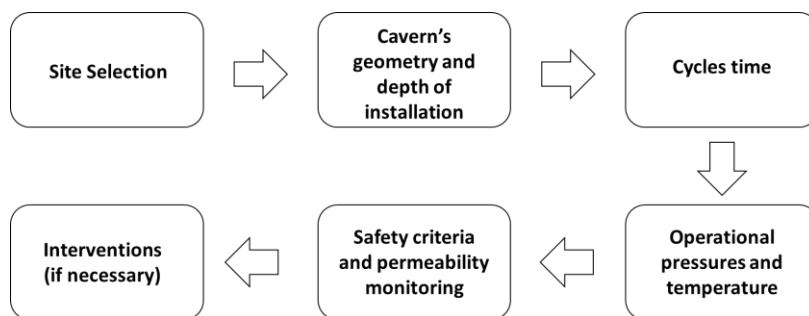


Figure 4.12 – Complete procedure for salt cavern installation and monitoring.

#### 4.10. Validations in GeMA framework

Before analyzing the several proposed case studies, we implemented a series of C++ and Lua orchestrations to make the thermomechanical simulations possible using the GeMA framework. The first step was to define functions to carry out the REFPROP inputs (pressure and temperature) into GeMA, as shown in Figure 4.13.

```

-----
-- Functions
-----
local results = io.open('C:/Tese/GeMA/Caverna/TM/10_Days_LP/Mechanical/Results.txt', "w+")
local results_temp = io.open('C:/Tese/GeMA/Caverna/TM/10_Days_LP/Mechanical/Results_temp.txt', "w+")

NodeFunction { id = 'inito',
               parameters = { {src = 'coordinate', dim = 2, unit = 'm'} },
               method = function(y)
                 local Ti = 298 + 0.012*(1000-y)
                 --local topT = 273+0.03*700
                 --local Yref = -2700
                 return Ti--topT + 0.012*(Yref-y)
               end
             }

NodeFunction { id = 'cycles',
               parameters = { {src = 'coordinate', dim = 2, unit = 'm'},
                              {src = 'time', unit = 's'} },
               method = function(y,t)
                 if (t>=31160) then
                   local tab_temp = {
                     for i=1,#tab_temp-1 do
                       local time_initial = tab_temp[i][1]
                       print(initial)
                       --
                       local time_final = tab_temp[i+1][1]
                       local temp_initial = tab_temp[i][2]
                       local temp_final = tab_temp[i+1][2]

                       if (t > time_initial and t <= time_final) then
                         local rate = (temp_final-temp_initial)/(time_final-time_initial)
                         print(rate)
                         local update_temp = temp_initial + rate*(t-time_initial)
                         results_temp:write(tostring(t), " ", tostring(update_temp), "\n")
                         return update_temp
                       end
                     end
                   else
                     local temp = 298 + 0.012*(1000-y)
                     results_temp:write(tostring(t), " ", tostring(y), " ", tostring(temp), "\n")
                   end
                 end
               end
             }

```

**Inputs from REFPROP  
are carried out in GeMA  
as a table**

Figure 4.13 – Orchestration to carry out REFPROP inputs into GeMA.

Therefore, pressure and temperature are updated each time step and loaded as a boundary condition during steps 3 and 4, first filling and cycles, respectively. In this way, the research overcomes the current gap regarding thermomechanical coupling simulations for gas storage in the Brazilian literature. Subsequently, we also implemented an orchestration to evaluate the dilatancy index in the salt rocks. It was chosen the Van Sambeek, Ratigan, and Hansen (1993) dilatancy boundary. Regarding permeability, we orchestrated the Peach (1991) criterion associated with the volumetric strains.

We selected the commercial simulator ABAQUS® software to provide a comparison with GeMA. The tests considered the thermomechanical coupling contemplating all the premises explained in the previous sections. The validations were: stresses (S11, S22, and Mises), displacements, and permeability. The first results are shown in Figure 4.14.

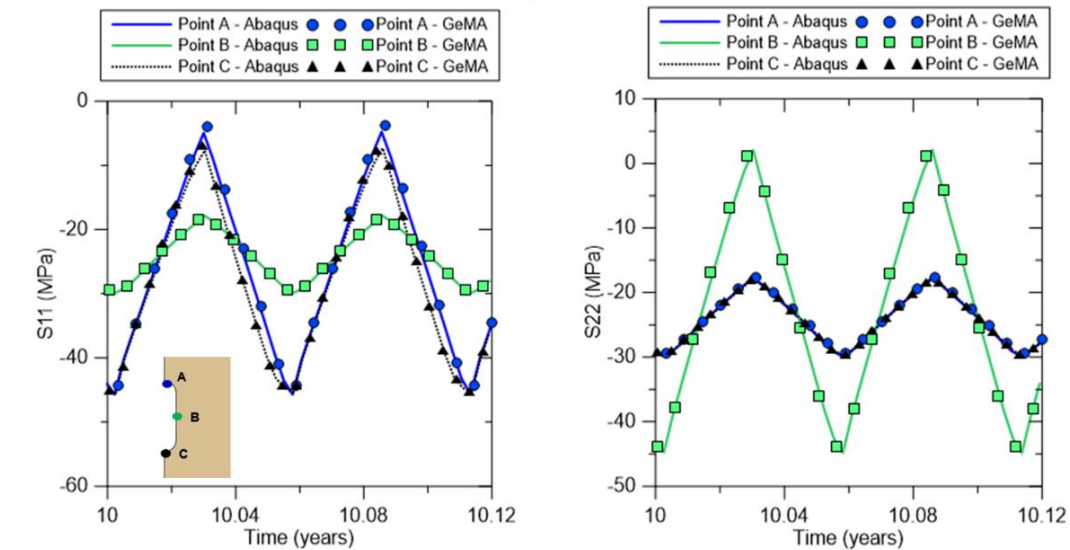


Figure 4.14 – S11 and S22 stress components validations in GeMA.

And the results for the von Mises equivalent stress and displacements are shown in Figure 4.15.

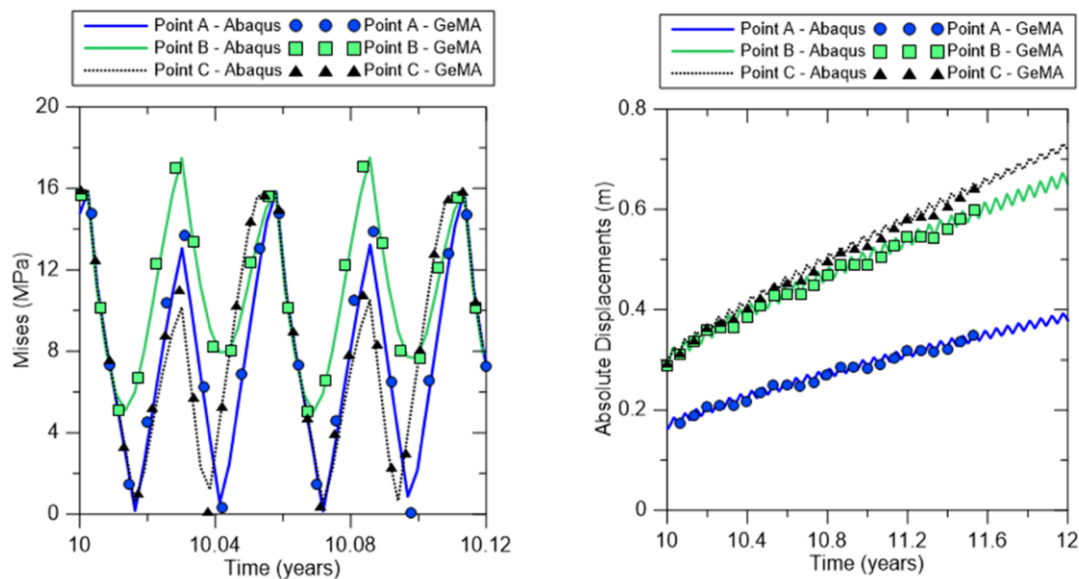


Figure 4.15 – von Mises equivalent stress and displacement validations in GeMA.

These results showed an excellent agreement with those obtained by the commercial simulator. Both software's cyclic peaks and downs are almost identical, so the thermomechanical coupling implementation and its connection with the thermodynamic inputs may be considered successful. The last validation was the permeability, presented in Figure 4.16.

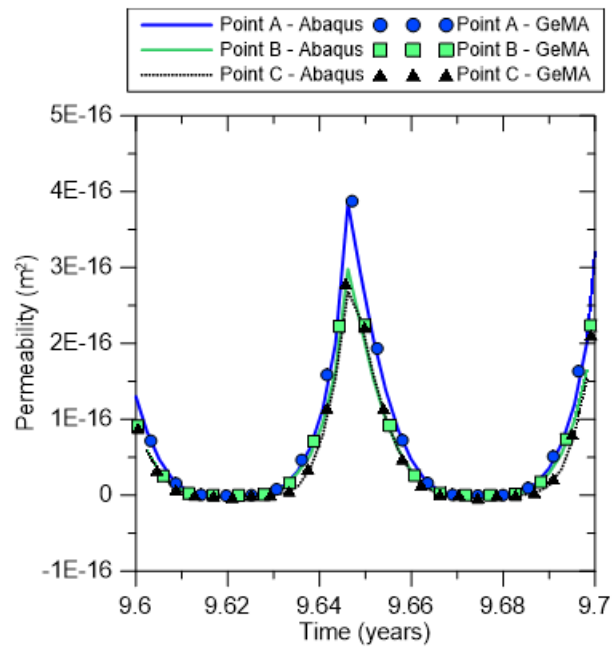


Figure 4.16 – Permeability validation in GeMA.

Therefore, the set of validations provided by GeMA is in accordance with the commercial simulator, and the next steps are related to the continuity of investigations of hydrogen storage under different conditions.

#### 4.11. Results and discussion

Three cavern points (A, B, and C) will monitor the stresses, dilatancy index, permeability evolution, and displacements. Figure 4.17 shows the evaluated points and axis orientation.

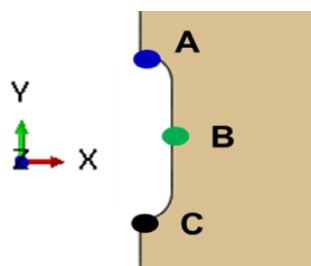


Figure 4.17 – Evaluated points in the salt cavern and the axis orientation.

Figure 4.18 exhibits the results considering only the mechanical analysis (steps 1 and 2). Steps 3 and 4 vary from case to case.

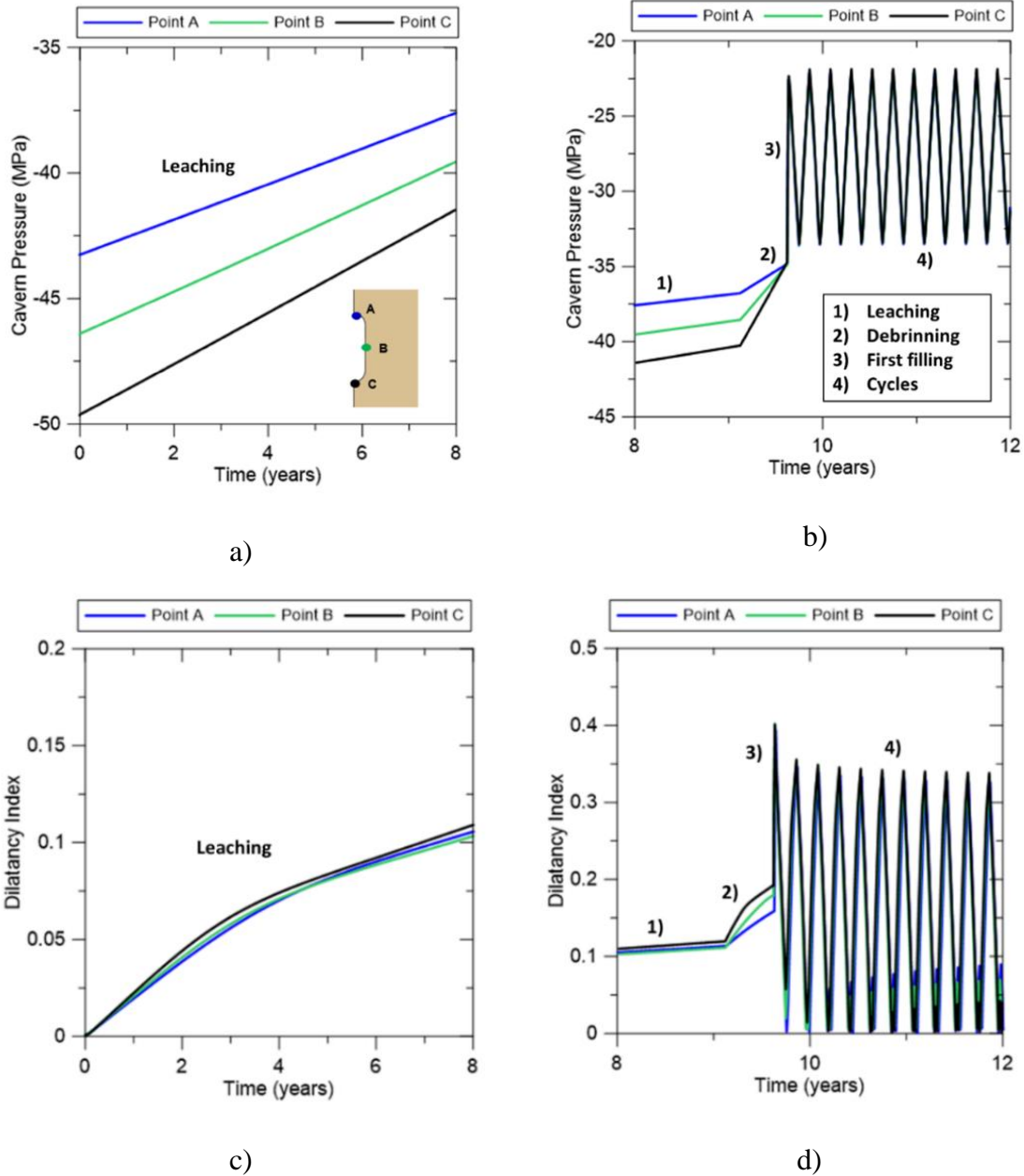


Figure 4.18 – a) Cavern pressure during the leaching stage; b) Cavern pressure during the subsequent stages; c) Dilatancy index during the leaching stage; d) Dilatancy index during the subsequent stages.

We emphasize that the simulations are purely mechanical until the first filling stage. Figure 4.23 shows the maximum values found during the simulations regarding the principal stresses.

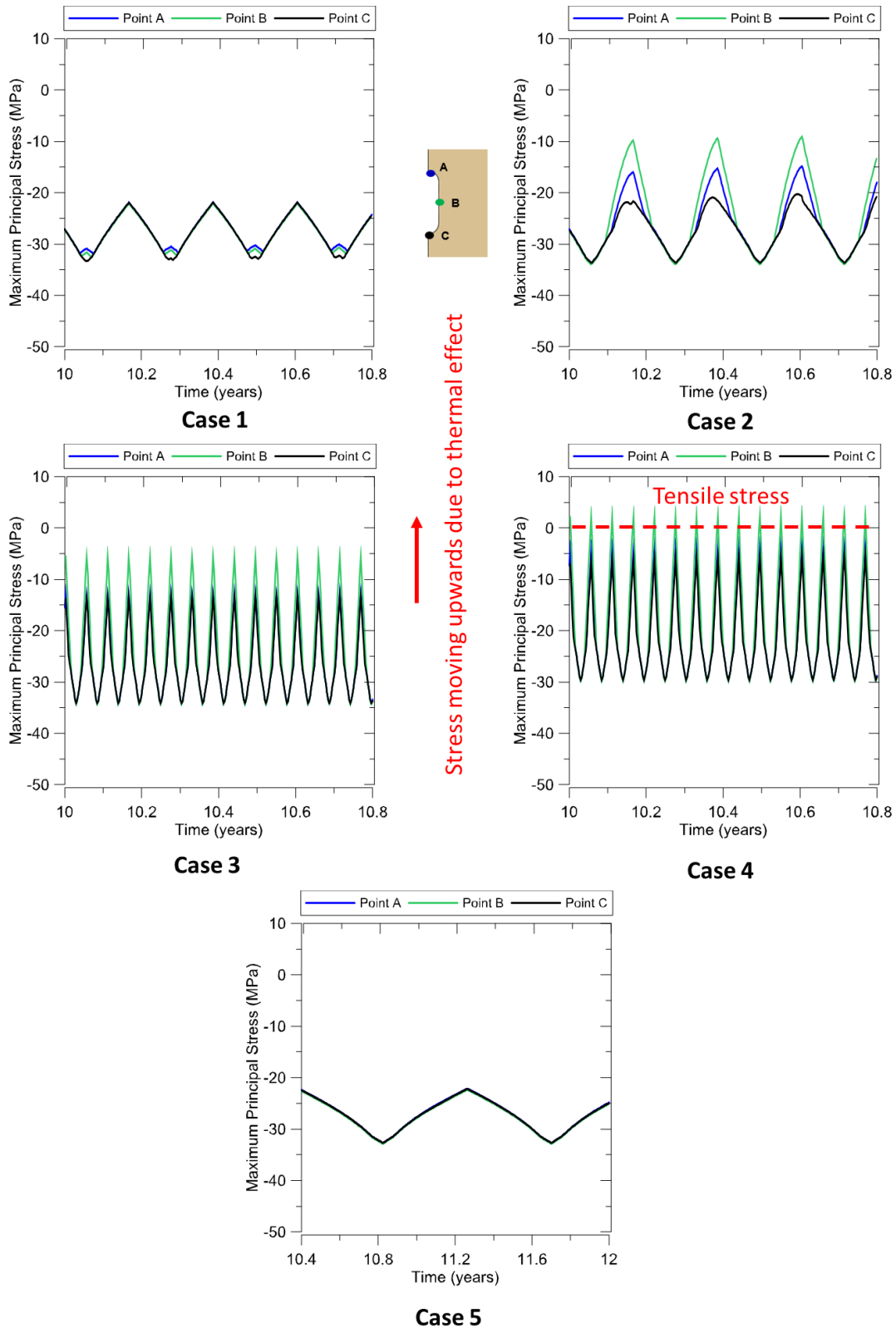


Figure 4.19 – Maximum principal stresses for cases 1 to 5.

The thermal effect was more significant at point B, as tensile stresses occurred during case 4 simulations. However, for case 5, the thermal effect is less critical. It demonstrates that the thermal effect becomes minimum for large cycles,

and the results are very close to the mechanical ones. Regarding short cycles, Case 2 showed us a stress increase, which presented a tendency of moving upwards to appear tensile stresses. It confirmed in case 4 - we noticed a tensile stress of 2.4 MPa at point B, above the halite tensile strength of approximately 1.80 MPa (Poiate 2012). Furthermore, the stress state violated the zero-tensile stress criterion, and cavern integrity was not assured. During field operation, Böttcher et al. (2017) recommend: 1) interrupting the cyclical storage scheme to dissipate effects accumulated during cycling and restore natural temperature levels; 2) increasing the cycle durations (accompanied by a reduction in mass fluxes) to reduce pressure and temperature rates. This example confirmed the expectation of high-temperature amplitude ( $\Delta T = 41.59\text{ }^{\circ}\text{C}$ ) inducing tensile stresses. We point out that a slight reduction in the injection pressure (10 %) drastically changed the loading scenario, warning the operators of the importance of a good assessment of the initial stress condition. Case 1 had less critical results, as expected. It confirms that the mechanical case may lead to a scenario of stress underestimation and put at risk the cavern integrity. For example, case 2 is a TM simulation with the same cycle duration as case 1. There, we could observe a stress increase, achieving approximately -10 MPa. Aiming to determine how important the thermomechanical analysis is, we performed an additional comparison: run a mechanical simulation of case 4. The results are shown in Figure 4.20.

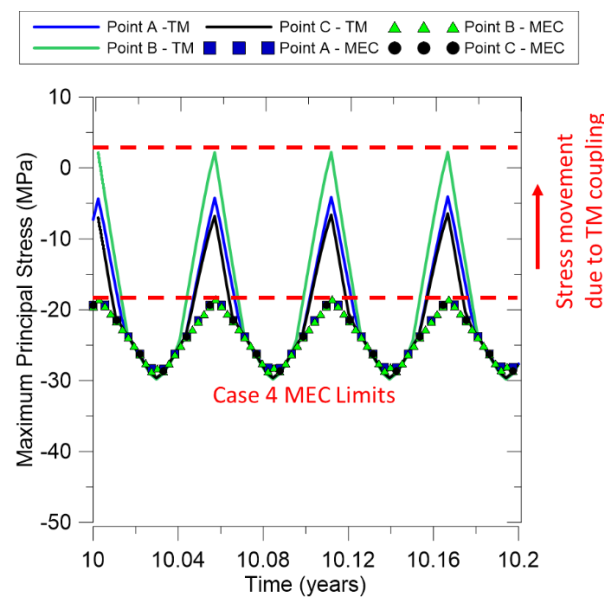


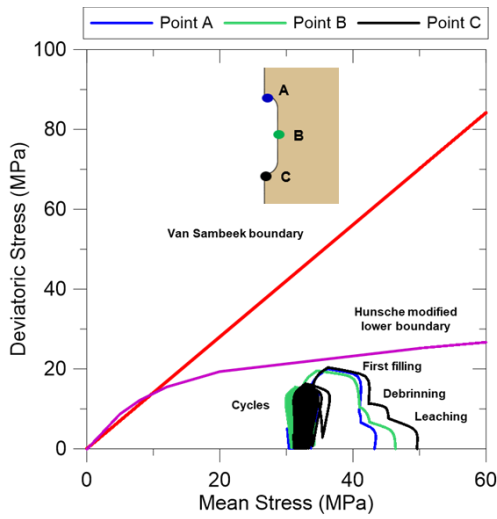
Figure 4.20 – Comparison between case 4 mechanical and TM analysis.

The study demonstrated that the mechanical analysis underestimated the stresses leading to an unrealistic scenario regarding short cycles of hydrogen storage. Thus, unsafety conditions are ignored when we only consider the mechanical aspects. For example, the maximum principal stress in the mechanical simulation was approximately -20 MPa of compression. However, during the TM coupling, the stress increased to a tensile of 2.4 MPa. If the mechanical simulation had been adopted to evaluate the cavern's integrity, the answer would be that safety was guaranteed once the tensile stress was not perceived. Unfortunately, the main problems would occur during the operation in the field. In this context, this thesis clarified how important TM coupling is during hydrogen storage analysis. We emphasize that the Brazilian literature often neglects the thermal influence of any gas storage (Poiate 2012; Costa et al. 2015; Firme et al. 2016, 2019; Maia da Costa et al. 2019; Abreu et al. 2023). Table 4.4 provides the stress increase (%), taking case 4 as a reference.

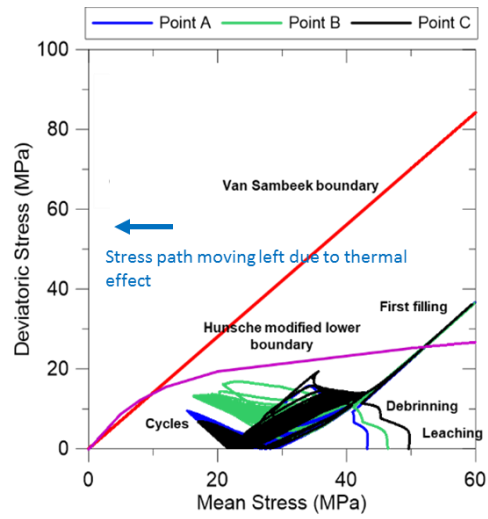
Table 4.4 – Comparison of maximum stress in case 4 against cases 1 to 5.

| <b>Case study</b> | <b>% Stress increase</b> |
|-------------------|--------------------------|
| 01                | 110 %                    |
| 02                | 124 %                    |
| 03                | 148 %                    |
| 05                | 108 %                    |

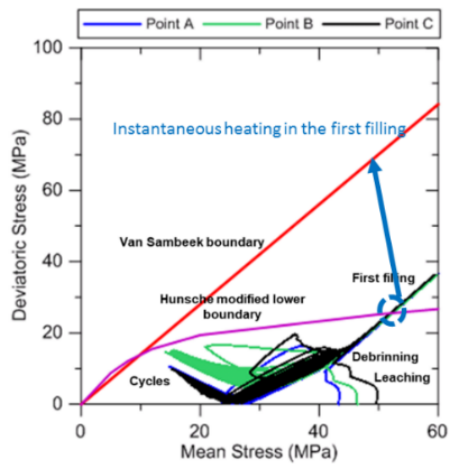
Case 4 showed a significant stress increase once the percentual overcame 100% compared to all the previous examples. To avoid damage in the salt cavern, reducing the frequency of the storage cycles may be a viable alternative (Böttcher et al. 2017). The numerical results of the p-q stress path are analyzed considering two dilatancy boundaries. The first was proposed by van Sambeek, Van Sambeek, Ratigan, and Hansen (1993) – red line, and the second is the modified Hunsche lower boundary (Hunsche 1993), which is a more critical – pink line, as shown in Figure 4.21.



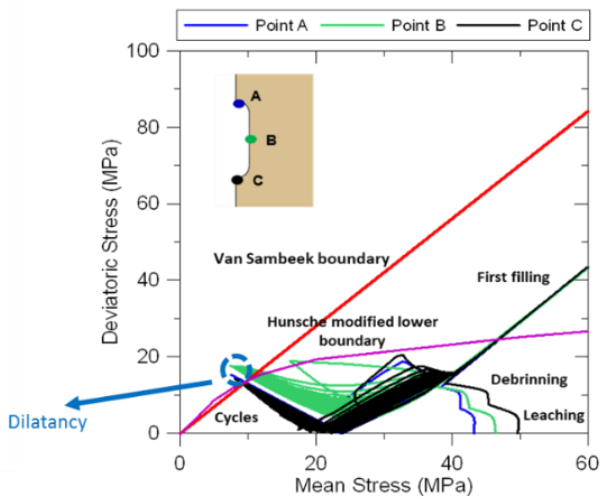
Case 1



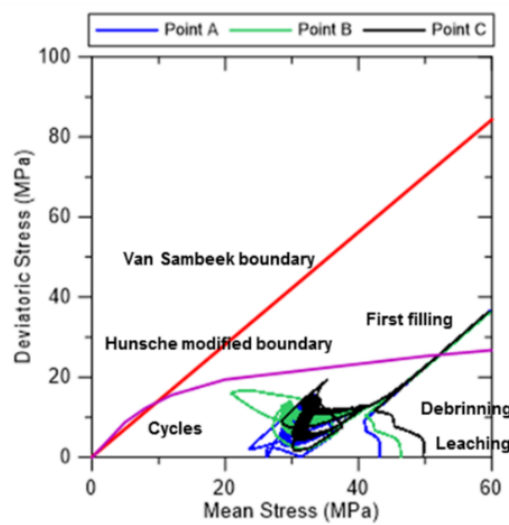
Case 2



Case 3



Case 4



Case 5

Figure 4.21 – Stress trajectory  $p \times q$  for cases 1 to 5.

The stress path comparative between cases 1 and 2 shows that the thermomechanical coupling provokes a movement in the left direction (a tendency of occurring tensile stresses). We observe the path very close to both dilatancy boundary limits in case 2. There are successive stress path peaks corresponding to each simulation step. It remains inside the compression domain for the mechanical and TM analyses (cases 2, 3, and 5). However, all TM cases violate Hunsche's boundary during the first filling stage. This peak stress occurs due to the high-temperature gas injection (60°C), while the salt layer has an average temperature of 30°C. The sudden heating raises the stresses abruptly. To mitigate this effect, the gradual heating of the cavern wall is recommended. In the cyclic loads, the stress path moved fast to the left. Dilatancy was observed in case 4 for both boundaries at all monitored points (A, B, and C), indicating that injection pressure reduction is a warning of cavern integrity loss. Cavern damage can compromise the permeability of the salt layer, and gas migration into the surrounding salt rock is inevitable. We point out that the current constitutive model does not evaluate the interaction between the dilatancy and self-healing phenomena. Thus, this is a more conservative approach, as healing can counterbalance damage propagation into the host rock. The analysis demonstrated that point B presented the most critical results, for instance, tensile stresses. Thus, Figure 4.22 shows a dilatancy index overview referring to all the case studies.

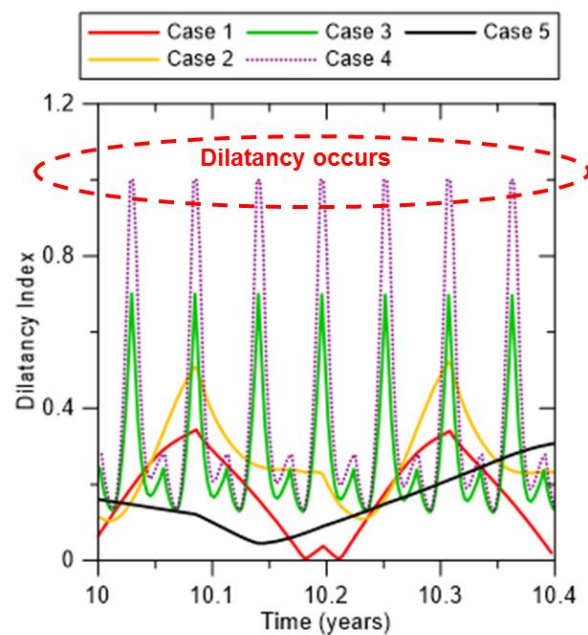


Figure 4.22 – Dilatancy index overview for all the case studies.

As expected, the mechanical analysis (case 1) presented the lowest DI, highlighting the importance of coupled simulations (TM). The less critical TM analysis (case 5) had a DI of approximately 0.35, demonstrating that a large cycle does not impact the cavern integrity, and the temperature effect can be neglected. On the other hand, in the most critical TM analysis (case 4), DI increased by 185% regarding the same reference. We notice how the injection pressure affects the results; for example, DI in case 4 is approximately 30% higher than in case 3.

Regarding the DI zone of influence inside the salt rock, the mechanical simulation showed an affected region of approximately 130 m measured radially from the cavern wall. However, we noticed a further advance of more than 50 m into the host rock for the TM simulation in case 4 (the most critical). In the zone where DI equals 1.0, the damage is restricted to the cavern wall. Figure 4.23 exhibits a comparison between cases 1 and 4.

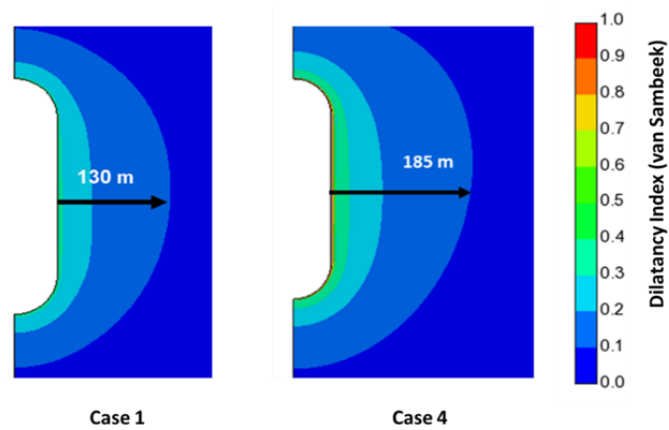


Figure 4.23 – Comparison of DI disturbed zones between cases 1 and 4.

The thermal diffusion for case 4 through a segment called “path” ( $L=1000$  m) is shown in Figure 4.24

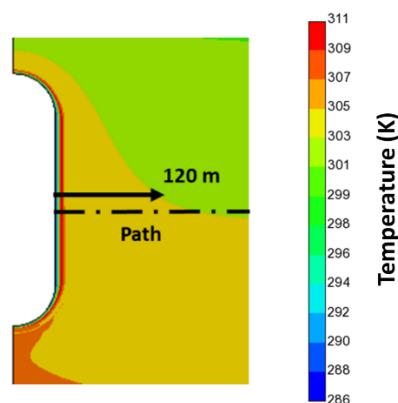


Figure 4.24 – Thermal diffusion for case study 4.

We observed an extension of 120 m, where the temperature returned to the geostatic values. The temperature x distance from the wall plot is shown in Figure 4.25.

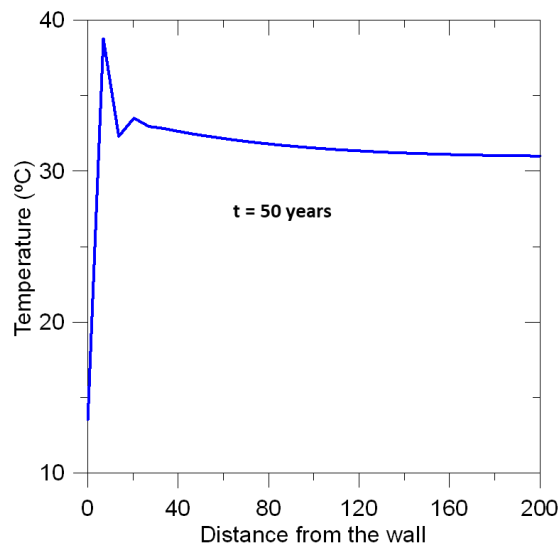


Figure 4.25 – Temperature distribution measured from the cavern’s wall for case study 4

Regarding permeability, it remains low in case studies 1 and 5, and cavern tightness is still assured. During the TM simulations, the potential for leakage was verified. For instance, the maximum permeability in cases 3 and 4 was approximately  $3.5 \times 10^{-16}$ . As expected, the most critical cases are 3 and 4, when the cycles happen fast. However, the permeability in case 3 is slightly higher than in case 4, even with the reduced injection pressure. The criterion adopted to measure permeability in terms of the volumetric strains is highly influenced by cavern heating. In the TM analyses, cases 3 and 4 reach similar temperatures, with a more pronounced effect in the cooling stage (cavern depressurization) for case 4. Table 4.5 presents the maximum permeability obtained in all simulations.

Table 4.5 – Permeability summary after the simulations.

| Case study | Maximum permeability (m <sup>2</sup> ) |
|------------|--|
| 01         | $5 \times 10^{-18}$                    |
| 02         | $1.7 \times 10^{-16}$                  |
| 03         | $3.7 \times 10^{-16}$                  |
| 04         | $3.5 \times 10^{-16}$                  |
| 05         | $2 \times 10^{-17}$                    |

In case 3, the initial permeability of the host rock is affected at a distance of approximately 20 m, as shown in Figure 4.26. Since problems involving hydrogen leakage are frequent - Zivar et al. (2021), a hydraulic investigation may be necessary to evaluate better how the gas propagates into the host rock.

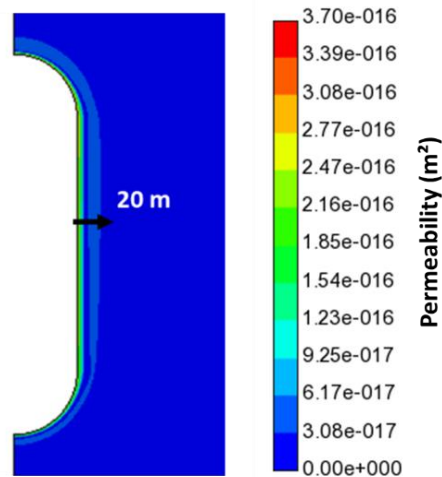


Figure 4.26 – Permeability changes in the host rock.

Finally, Figure 4.27 shows the cavern displacements for all cases. Results are plotted for each monitored point. Cavern creep closure was expressive at point C. As already observed, the mechanical analysis (case 1) presented the lowest displacements. However, compared to all TM simulations, it makes evident how the temperature accelerates closure and, consequently, volume losses, an undesirable effect (Böttcher et al. 2017). According to Khaledi et al. (2016), when the volume decreases, the storage capacity of the cavern reduces, affecting the serviceability of the whole storage system. Volume reduction also affects gas thermodynamics, making the process more complex to be realistically represented (Xia et al. 2015). In case 4, displacements were above 6 m for points B and C. It is almost twice that of case 3 with the same cycle duration. The injection pressure is a warning to operators and must be constantly monitored. Comparing TM cases with the same injection pressure (cases 2 and 3), we observed that the cycle frequencies had a minor influence on the displacements, a similar effect evidenced by Böttcher et al. (2017). Case 5 had the lowest displacements between the TM case studies. It shows that the thermal contribution was minimum, and the cavern integrity is guaranteed for large cycles.

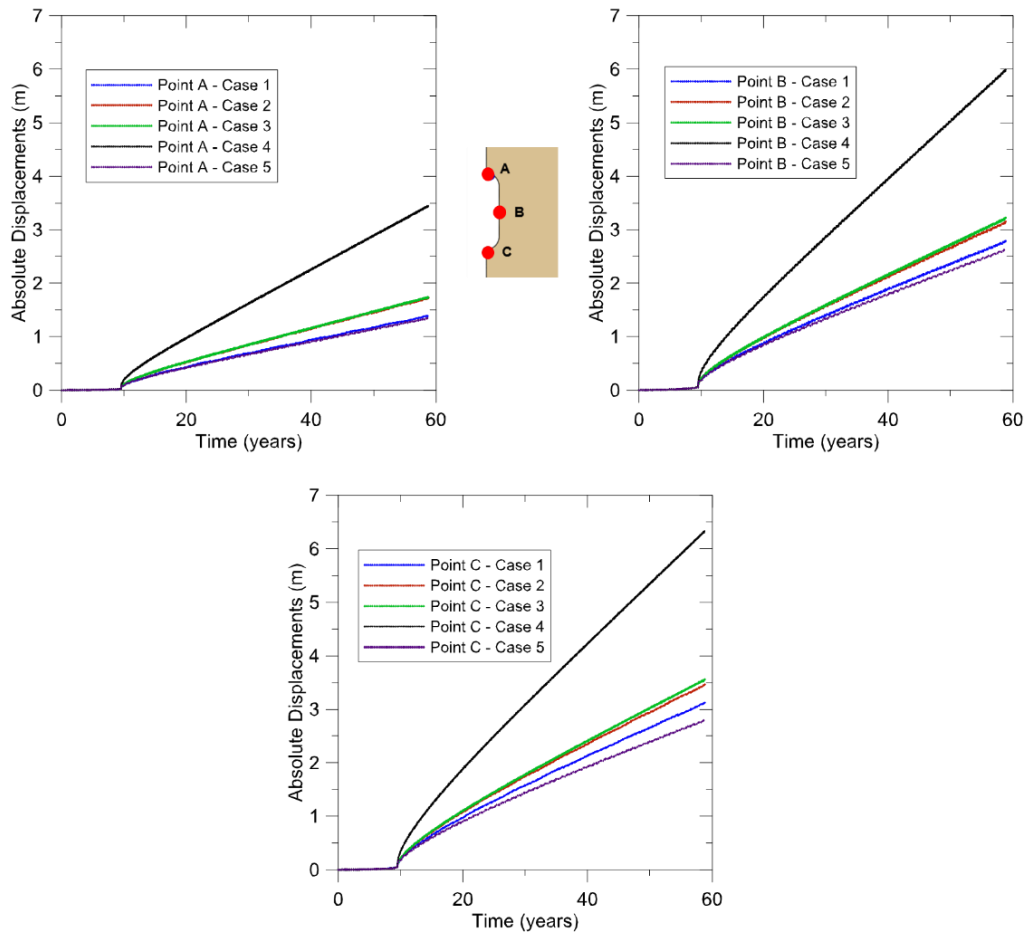


Figure 4.27 – Cavern displacements at all the monitored points for all the case studies.

In order to ease the comprehension of all the case studies results, we provided a table summary (Table 4.6) with the most important information observed from the simulations. Results were collected during the cyclic load.

Table 4.6– Relevant results during the case studies.

| Case study | Maximum DI | Maximum Permeability (m <sup>2</sup> ) | Maximum Closure in point A (m) | Maximum Closure in point B (m) | Maximum Closure in point C (m) | Tensile Criterion |
|------------|------------|--|--------------------------------|--------------------------------|--------------------------------|-------------------|
| 01         | 0.35       | $5 \times 10^{-18}$                    | 1.3                            | 2.6                            | 3.1                            | Ok                |
| 02         | 0.55       | $1.7 \times 10^{-16}$                  | 1.6                            | 2.9                            | 3.4                            | Ok                |
| 03         | 0.70       | $3.7 \times 10^{-16}$                  | 1.7                            | 3.0                            | 3.5                            | Ok                |
| 04         | 1.00       | $3.5 \times 10^{-16}$                  | 3.5                            | 5.7                            | 6.3                            | Violated          |
| 05         | 0.35       | $2.7 \times 10^{-17}$                  | 1.3                            | 2.6                            | 2.7                            | Ok                |

#### 4.12. Partial conclusions

From the five cases analyzed, the main conclusions are:

- ✓ The temperature may significantly vary during hydrogen storage and influence the pressure inside the cavern. Thus, the best representation must consider the associated thermodynamics. The simulations in case study 4 demonstrated that the mechanical analysis underestimated the stresses leading to an unrealistic scenario for short cycles of hydrogen storage, and unsafe conditions are ignored when we only consider the mechanical aspects. For example, the maximum principal stress in the mechanical simulation was approximately -20 MPa of compression. However, in the TM analysis, the stress increased to a tensile value of 2.4 MPa;
- ✓ If the tensile stress criterion is violated, the field operator must provide the following responses: 1) interrupt the cyclical storage scheme to dissipate effects accumulated during cycling and restore natural temperature levels; 2) increase the cycle durations (accompanied by a reduction in mass fluxes) to reduce pressure and temperature rates;
- ✓ This research developed a thermodynamic simulator based on Xia et al. (2015) diabatic solution. This solution considers the heat exchange between cavern gas and the surrounding rock, leading to realistic responses. It also updates the gas pressure and temperature at each time step ( $t_{n+1}$ ), considering the previous results ( $t_n$ ). The gas properties are obtained through a link with the REFPROP gas library (Lemmon et al. 2018). Therefore, a realistic solution for hydrogen storage makes it possible to evaluate the cavern's integrity under the conditions faced during its operation;
- ✓ Five case studies with different time cycles and injection pressure were considered to comprehend this problem better. Results demonstrated that faster cycles provoke higher temperature amplitudes, making the safety criteria more difficult to guarantee. Longer time cycles showed similar results to the mechanical model, as the temperature amplitude is low. Our simulations demonstrated that cycles above 20 days are less critical for cavern integrity;

- ✓ The gas injection pressure also takes an important role: a reduction of just 10% induced the occurrence of tensile stresses, occasioned the dilatancy phenomenon, and significantly increased the cavern's convergence (100% in point A).

## 5 Analysis of field applications

Although the last chapter clarifies different ways to store hydrogen in salt caverns, there is still a gap in the literature regarding the effect of heterogeneous layers and real cavern shapes on the cavern integrity - Ramesh Kumar et al. (2021). As also demonstrated, the permeability evolves during the heating/cooling process, and an additional study is necessary to understand and assess the risks of gas migration into the host rock.

### 5.1.Heterogeneous salt cavern

The Brazilian pre-salt fields are a challenging scenario for exploration, because of the particular structural salt behavior with intercalations of halite, anhydrite, and in some places, tachyhydrite and carnallite (Costa et al. 2011). According to Costa et al. (2005), the oil industry has reported several operational problems, such as casing collapse, stuck pipes, and fluid losses when drilling through and near salt layers. However, these evaporitic sections are a favorable environment for gas storage due to the intrinsic characteristics of salt rock, such as low porosity and permeability, self-healing, and creep deformation, which make possible to tolerate high levels of strain without developing structural damage of its mineral skeleton (Poiate 2012; Costa et al. 2015). From Firme et al. (2014), a typical pre-salt lithology is shown in Figure 5.1.

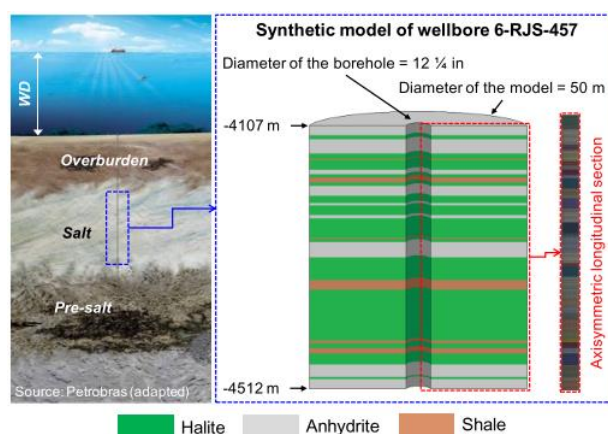


Figure 5.1 – Typical pre-salt lithology, Firme et al. (2014).

The Santos Basin is located in Brazil's offshore southeast. Costa et al. (2011) point out that it is one of the Brazilian basins that is receiving considerable industry attention, with the discovery of the giant oil fields known as Pre-Salt reservoirs. The water depth varies from 150 m to 2200 m, and the salt stratifications are about 2000 m of extension. Figure 5.2 shows a representation of the Santos Basin location. It is Brazil's largest offshore sedimentary basin, ranging for a total area of over 350,000 square kilometers, from Cabo Frio (state of Rio de Janeiro) to Florianópolis (state of Santa Catarina) and the first investments in exploration and production studies for this basin started in the 1970s - Petrobras (2023).

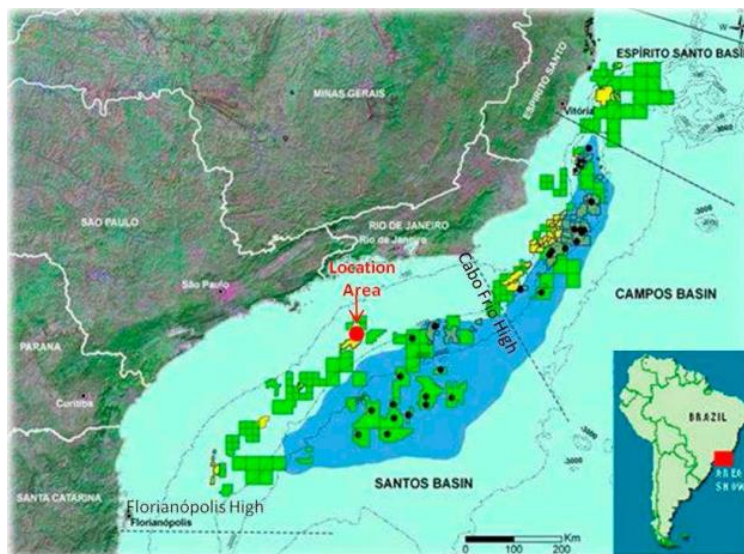


Figure 5.2 – Santos Basin location, Petrobras (2023).

In particular, the Tupi field seems to be an interesting area for investigating the effect of heterogeneous salt layers, as the Brazilian National Agency of Petroleum, Natural Gas and Biofuels (ANP) has an extensive database from the drilled wells in this region.

The Tupi field is located in the Santos Basin, 250 kilometers from the coast of Rio de Janeiro state. The nickname was in honor of the Tupi people and was later named after the mollusk. It is considered the Western hemisphere's largest oil discovery in the last 30 years - Koning (2015). Figure 5.3 shows a stratification from the Tupi field.

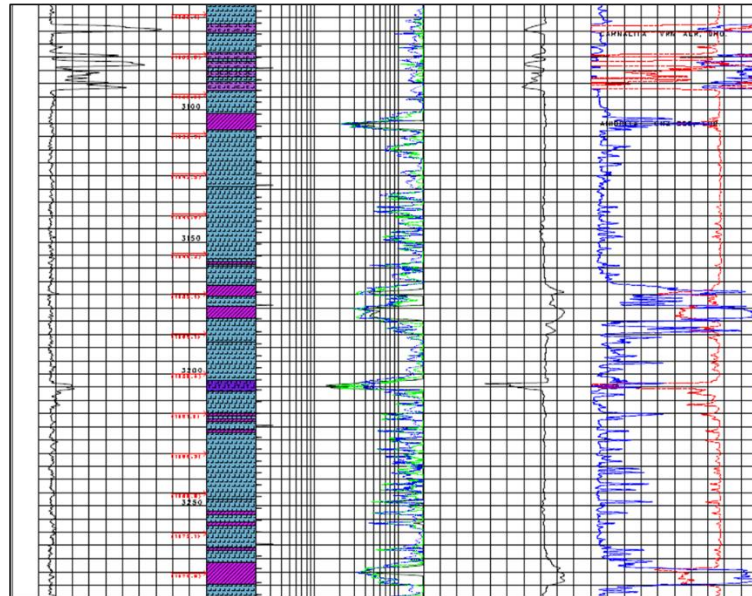
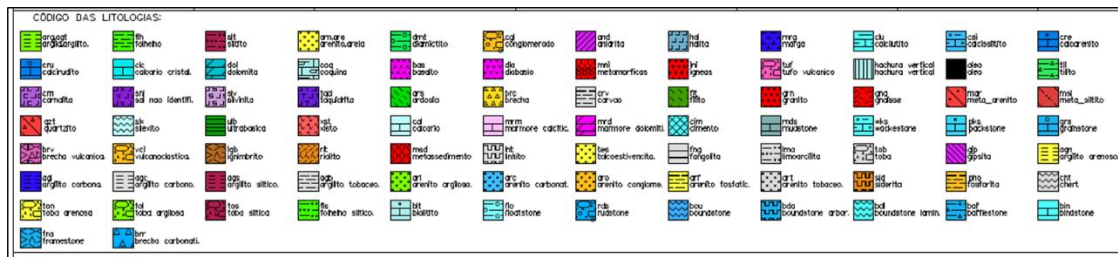


Figure 5.3 – Stratification from the Tupi field.

It demonstrates how heterogeneous the lithology is in some regions of the field. In this case, assuming a full-filled halite area may lead to a non-representative simulation of the site where the salt cavern will be installed. Ramesh Kumar et al. (2021) highlight the gap in the Brazilian literature related to caverns with complex geometries and different creep governing mechanisms for heterogeneities, such as carnallite. From Poiate (2012), we observe that the creep phenomenon is much more pronounced in carnallite and tachyhydrite salt rocks and minimum in anhydrite. This combination of different salt rocks may impact the cavern displacements with an expressive or reduced closure tendency.

### 5.1.1. Region for the salt cavern installation

Based on the ANP's database, we selected the log file from well 9-BRSA-716-RJS in the Lula Field, part of the Santos Basin. The salt cavern will have the same premises presented in the fourth chapter (geometry and depth),

which makes it possible to adopt the geothermal and stress gradients shown in Section 4.3. Figure 5.4 exhibits the heterogeneous lithology.

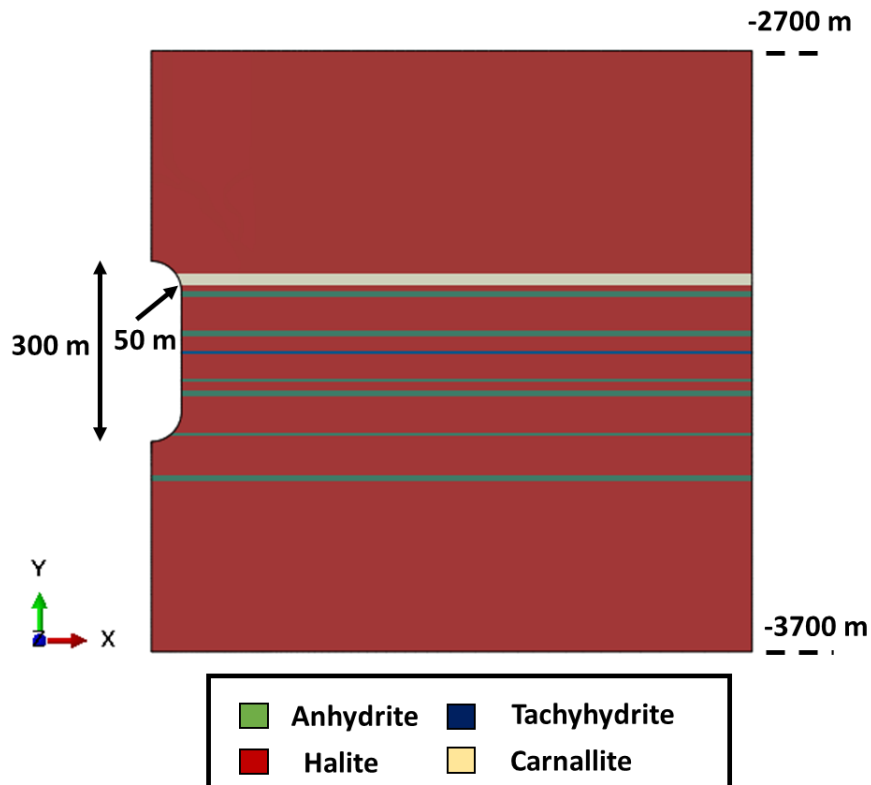


Figure 5.4 – Salt cavern lithology in the Tupi field.

It can be observed an intense combination of halite-anhydrite layers, as well as two intercalations of carnallite and tachyhydrite that may impact the creep phenomenon along the 50-years cycle.

### 5.1.2. Rock properties

The salt rock properties follow those in the Brazilian literature (Costa et al. 2005, 2011; Poiate 2012; Firme et al. 2014, 2018, 2019), part of experimental and numerical studies realized in Brazil. In order to ease comprehension, Table 5.1 provides the elastic and elasto-plastic properties of the different salt rocks.

Table 5.1– Salt rock properties.

| <b>Salt rock<br/>Parameter</b> | <b>Unit</b> | <b>Halite</b> | <b>Carnallite</b> | <b>Anhydrite</b> | <b>Tachyhydrite</b> |
|--------------------------------|-------------|---------------|-------------------|------------------|---------------------|
| Young's modulus                | GPa         | 25.37         | 4.2               | 55.11            | 4.92                |
| Poisson's ratio                | -           |               | 0.36              |                  | 0.33                |
| Cohesion                       | MPa         | -             |                   | 0.9              | -                   |
| Friction angle                 | °           | -             |                   | 37               | -                   |
| Dilatancy angle                | °           | -             |                   | 17               | -                   |

Moreover, the creep parameters for the visco analysis (Poiate 2012; Lira et al. 2015) are given in Table 5.2.

Table 5.2– Creep parameters for the salt rocks.

| <b>Salt rock<br/>Parameter</b> | <b>Unit</b>     | <b>Halite</b>           | <b>Carnallite</b>      | <b>Tachyhydrite</b>    |
|--------------------------------|-----------------|-------------------------|------------------------|------------------------|
| Thermal activation energy      | J/mol           |                         | 50,160                 |                        |
| Universal gas constant         | J/mol.K         |                         | 8.314                  |                        |
| Threshold creep rate           | h <sup>-1</sup> | 1.88 x 10 <sup>-6</sup> | 1.55x 10 <sup>-4</sup> | 2.99x 10 <sup>-4</sup> |
| Threshold deviatoric stress    | MPa             | 9.91                    | 5.71                   | 8.14                   |
| Threshold temperature          | K               | 359.15                  | 403.15                 | 359.15                 |
| $n_1$                          | -               | 3.36                    | 2.87                   | 2.59                   |
| $n_2$                          | -               | 7.55                    | 7.17                   | 7.49                   |

Halite, carnallite, and tachyhydrite are modeled as visco-elastic materials. Anhydrite is an evaporite with negligible creep behavior. Thereby, it is an elasto-plastic material. We selected the Mohr-Coulomb constitutive model to evaluate plasticity. The other salt rocks adopt the Van Sambeek, Ratigan, and Hansen (1993) dilatancy boundary (only for post-processing).

The material properties of the different salt rocks and parameters for the analytical solution for gas temperatures are presented in Table 5.3 (Lira et al. 2015; Xia et al. 2015; Böttcher et al. 2017; Zhu et al. 2017).

Table 5.3– Material properties for salt rock and parameters for the analytical.

| Salt rock<br>Parameter           | Units                             | Halite | Carnallite           | Anhydrite | Tachyhydrite           |
|----------------------------------|-----------------------------------|--------|----------------------|-----------|------------------------|
| Density                          | kg.m <sup>-3</sup>                | 2040   | 1600                 | 2918      | 1667                   |
| Thermal Conductivity             | Wm <sup>-1</sup> K <sup>-1</sup>  |        |                      | 7         |                        |
| Thermal expansion<br>coefficient | K <sup>-1</sup>                   |        | 4 x 10 <sup>-5</sup> |           | 4.2 x 10 <sup>-5</sup> |
| Specific heat capacity           | Jkg <sup>-1</sup> K <sup>-1</sup> |        | 880                  |           | 900                    |
| Heat transfer coefficient        | Wm <sup>-2</sup> K <sup>-1</sup>  |        |                      | 1.2       |                        |

### 5.1.3. Load conditions

Figure 5.5 shows a schematic representation of pressure and temperature ups and downs along a cycle.

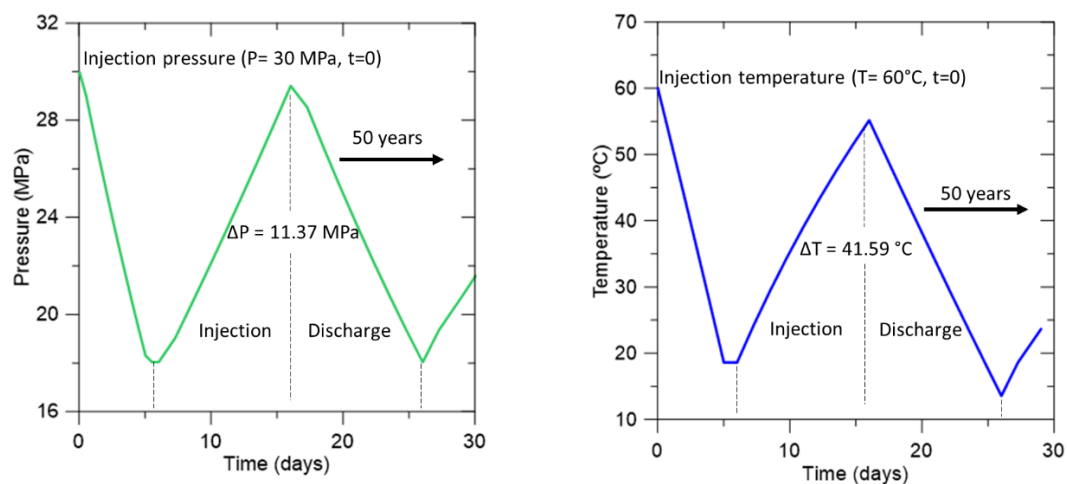


Figure 5.5 – Gas pressure and temperature along a cycle.

The load conditions follow the same presented in Figure 4.8 for the pre-cyclic operation. Regarding the cyclic stage, we selected the hypothesis evaluated in case study 4, which was demonstrated to be the most critical example analyzed.

### 5.1.4. Results and discussion

Six cavern points (A to F) will monitor the stresses, dilatancy or Mohr-Coulomb ratio, permeability evolution, and displacements. The same safety criteria explained in the previous chapter will be considered here. The first results are shown in Figure 5.6. The maximum principal stress plot shows that points E

and F (halite layer) have positive stresses, which means tensile occurring. Thus, the safety criteria of not having tensile stresses (Böttcher et al. 2017) was violated. Although point A does not exceed the tensile domain, it is very close and represents a region requiring attention. As expected, the layers of Carnallite and tachyhydrite (points B and D) remain under compression. In fact, these rocks have an accentuated creep property, which contributes to dissipating the stresses and, consequently, makes them less prone to integrity concerns. The anhydrite (point C) also presented only compression stresses, as the creep properties are negligible. The accumulated stresses provoke plastic strains, as seen in the following topics.

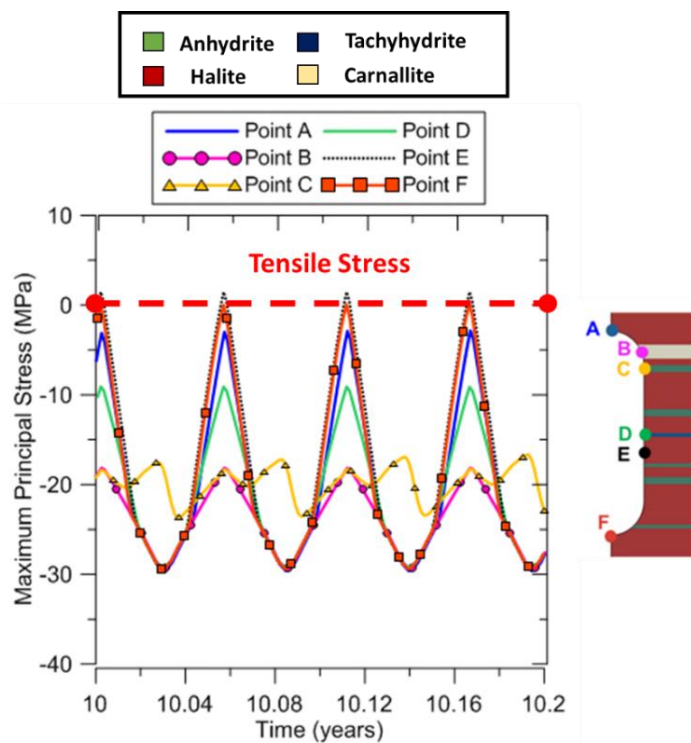


Figure 5.6 – Evaluated points in the salt cavern and axis orientation.

The stress trajectory ( $p \times q$ ) for halite, carnallite, and tachyhydrite points is plotted in Figure 5.7. We considered two dilatancy boundaries: the first was proposed by Van Sambeek, Ratigan, and Hansen (1993) – the red line, and the second is the modified Hunsche lower boundary (Hunsche 1993), the pink line. Excepted points B (carnallite) and D (tachyhydrite), all the others overcame both boundaries during the cyclic stage. As expected, carnallite and tachyhydrite are rocks with high mobility, so stresses can be quickly dissipated. During the first filling (when hydrogen is injected for the first time), all the monitored points crossed Hunsche's boundary limit. It occurs due to the fast temperature change at

the cavern walls. A similar phenomenon was observed during the chapter four analysis.

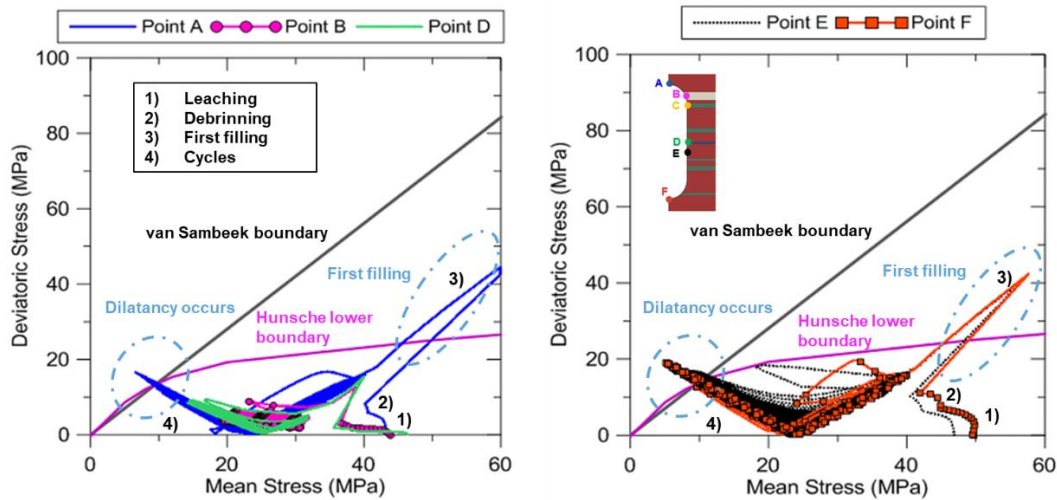


Figure 5.7 – Stress trajectory  $p \times q$  for points A, B, D, E, and F.

The dilatancy index, which represents a criterion to check if the points exceed or not the dilatancy boundary (van Sambeek), is shown in Figure 5.8. From the same conclusions achieved before, we noted that when DI is equal to 1, it represents the dilatancy boundary being crossed in Figure 5.7. In this case, the operator must control the cycle frequency to dissipate stress and reduce pressure/temperature rates. The rocks with high mobility had a DI in a range of 0.2-0.4 during the cyclic peak.

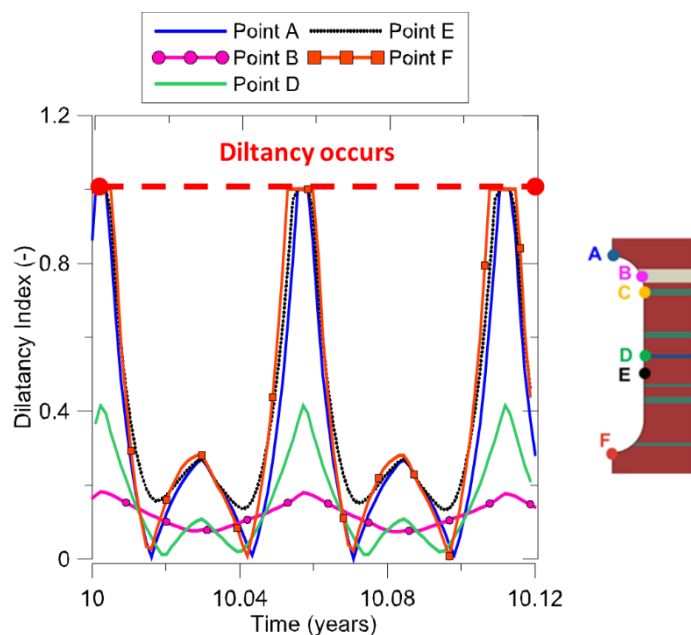


Figure 5.8 – Dilatancy index for points A, B, D, E, and F.

The Mohr-Coulomb (MC) constitutive model is adopted for anhydrite to evaluate plasticity during the analysis. Thus, we propose an MC ratio to express when the current stress state overcomes the envelope limits. For a general stress state, the yielding function is given below:

$$F = R_{MC}q - p \tan \varphi - c = 0 \quad (5.1)$$

Where  $q$  is the von Mises equivalent stress,  $p$  represents the equivalent pressure stress,  $\varphi$  is the friction angle, and  $c$  is the cohesion.  $R_{MC}$  means the MC deviatoric stress measure defined as:

$$R_{MC} = \frac{1}{\sqrt{3} \cos \varphi} \sin \left( \theta + \frac{\pi}{3} \right) + \frac{1}{3} \cos \left( \theta + \frac{\pi}{3} \right) \tan \varphi \quad (5.2)$$

$\theta$  is the deviatoric polar angle (Chen and Han 2007):

$$\cos(3\theta) = \left( \frac{r}{q} \right)^3 \quad (5.3)$$

Where  $r$  is the third invariant of the deviatoric stress. The material's friction angle controls the yield surface's shape in the deviatoric plane. If  $\varphi = 0^\circ$ , the model reduces to the pressure-independent Tresca model. However, if  $\varphi = 90^\circ$ , the model turns into the “tension cutoff” Rankine model with a triangular deviatoric section (ABAQUS 2011). Figure 5.9 exhibits the Mohr-Coulomb yield surface in meridional and deviatoric planes.

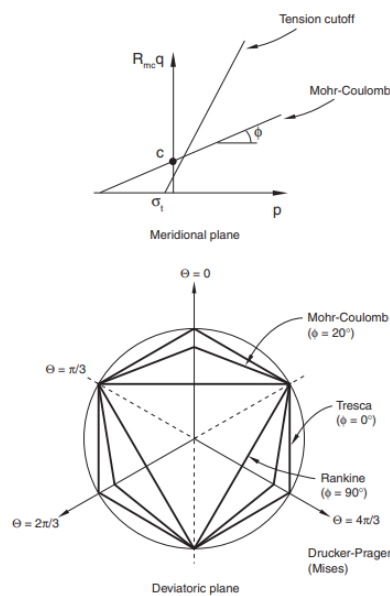


Figure 5.9 – Mohr-Coulomb yield surface in meridional and deviatoric planes (ABAQUS 2011).

Thus, the yielding function can be rewritten to determine the maximum von Mises equivalent stress that guarantees to stay inside the elastic domain:

$$q_{max} = \frac{p \tan \varphi + c}{R_{MC}} \quad (5.4)$$

The MC ratio can be expressed in terms of the current deviatoric stress ( $\sigma_d$ ) divided by the maximum von Mises equivalent stress allowed according to the referred constitutive model:

$$MC \text{ ratio} = \frac{\sigma_d}{q_{max}} \quad (5.5)$$

Figure 5.10 shows a general overview of the dilatancy index or MC ratio during a cycle peak. The closer the value is to 1, the closer the current stress state is to exceeding the envelope limits. All the salt rocks overcame the safety criterion, with a significant horizontal extension for anhydrite. However, it is well-known that one of the most interesting characteristics of salt rock is its self-healing capacity, which may counter-balance damage.

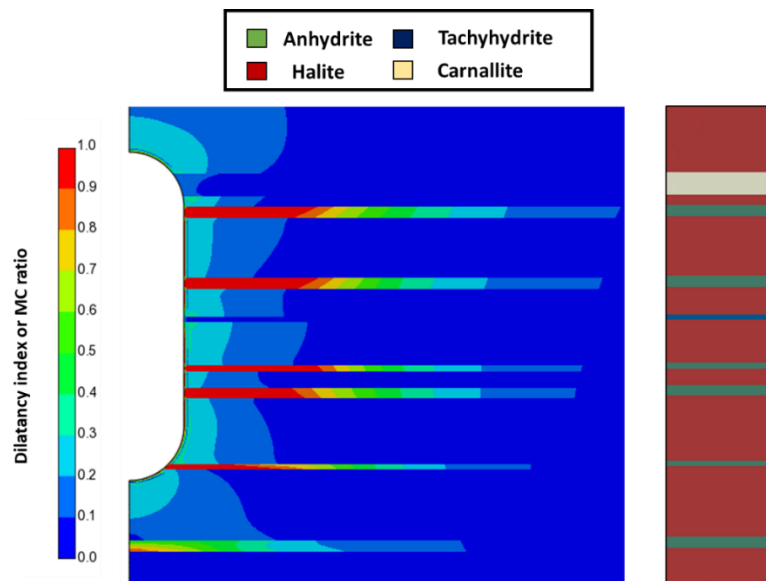


Figure 5.10 – Dilatancy index or MC ratio for the salt rocks.

In order to verify the extension of the zone where the current stress state crosses the envelope limits, we decided to plot six paths along the salt layers, as shown in Figure 5.11. Paths 1 and 4 are in the middle of the high mobility salt rocks: carnallite and tachyhydrite. Paths 2 and 5 cross the halite layers, and Paths 3 and 6, the anhydrite.

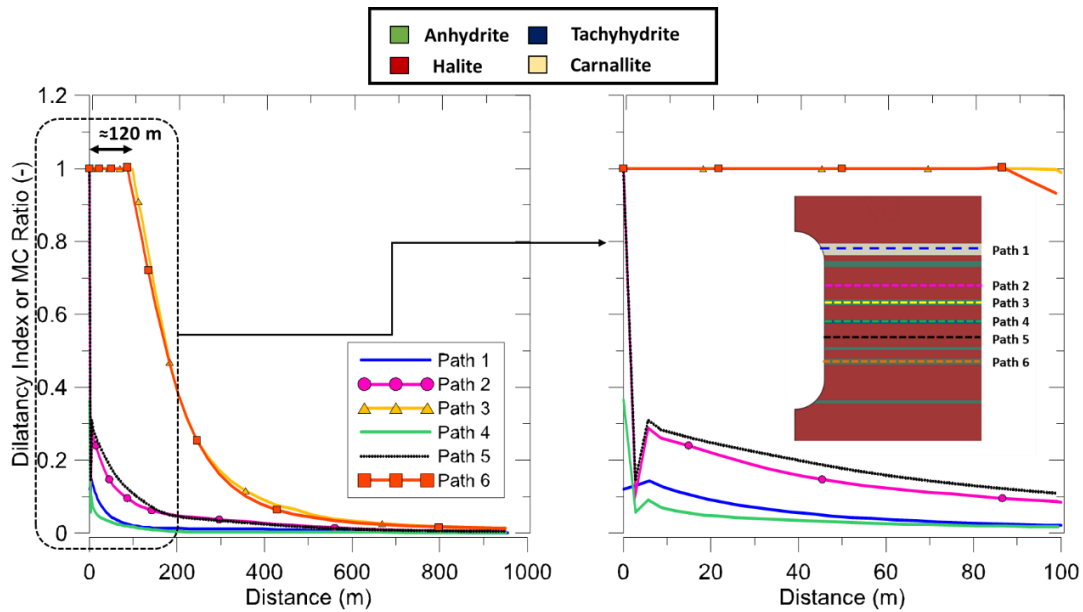


Figure 5.11 – Dilatancy index or MC ratio for the salt rocks.

The anhydrite layers exceed the MC envelope by at least 120 m from the cavern's wall. It means the critical zone where hydrogen migration is possible into the host rock (to be evaluated further). Carnallite and tachyhydrite paths are still inside the van Sambeek's envelope during the cycle peak. However, the halite layers presented a DI of 1 in all paths (2 and 5). Despite the safety criteria not having been attended to, we point out its limited region, approximately limited to the walls ( $\approx 2$  m).

The next step is to compare the heterogeneous model with the homogeneous one (from chapter four), aiming to understand best how the heterogeneity affects the rock cavern integrity during the hydrogen operation. Figure 5.12 shows that the homogeneous model has the entire wall crossing the dilatancy envelope during a cycle peak. At the same time, the heterogeneous one tends towards being less critical if the layers are carnallite or tachyhydrite. Thus, it seems interesting to have this type of rock with respect to the dilatancy criterion. At a significant distance from the cavern wall ( $\approx 100$  m), the heterogeneity, particularly the presence of anhydrite layers, has a negative effect: the MC envelope is crossed by the current stress state along the entire vertical depth. The distance dissipates the deviatoric stresses for the homogeneous model, and the rock integrity is guaranteed.

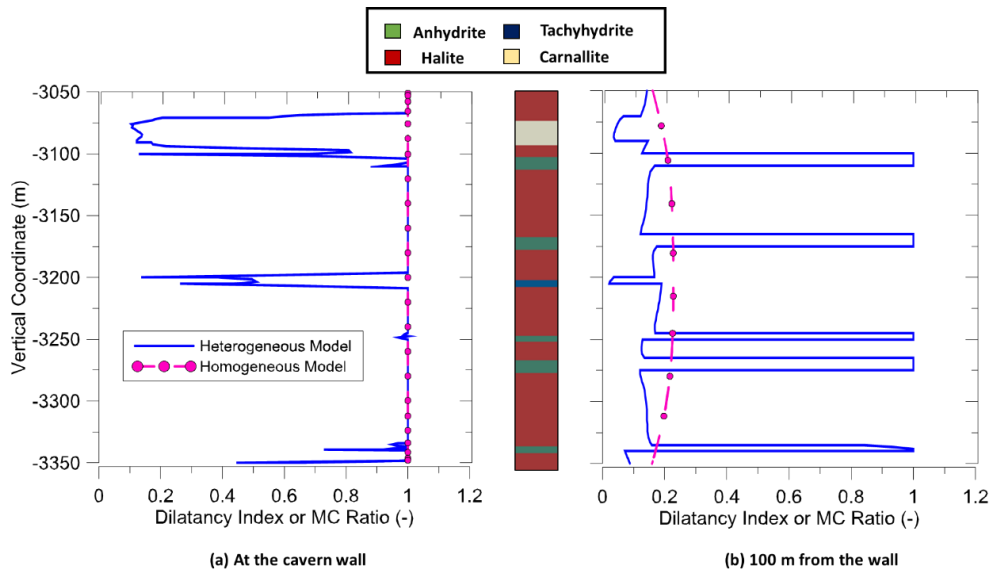


Figure 5.12 – Comparison of dilatancy index or MC ratio between the heterogeneous and homogeneous models.

We observed the shear stress concentrated in the interface regions between the anhydrite and halite layers – Figure 5.13. Due to the anhydrite's minimum creep properties, the halite tends to slip, and the shear effect is hugely majorated.

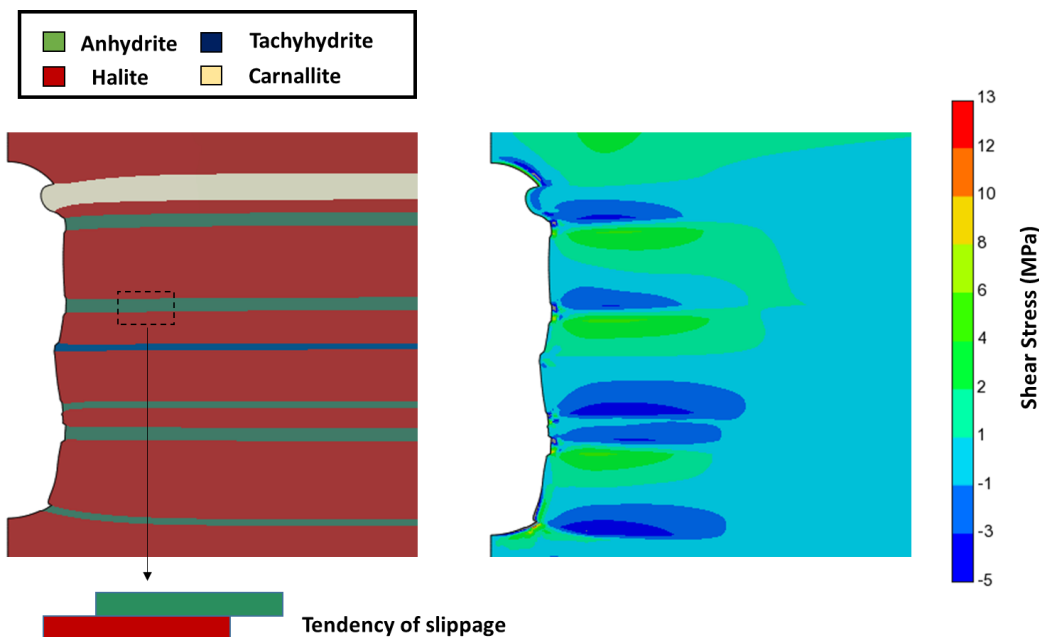


Figure 5.13 – Shear stresses in the salt cavern.

The permeability evolution along a cycle is shown in Figure 5.14. Carnallite and tachyhydrite are high-mobility salt rocks that directly influence the volumetric strains. As already demonstrated, Peach's law for determining the permeability in salt rocks is a function of the volumetric strains. Therefore, the results follow what

was expected: points B and D with the highest permeability increase. Unlike the dilatancy evaluation, these rocks assume a warning factor: the higher the permeability, the higher the possibility of gas migration into the host rock. Therefore, it highlights the importance of providing a hydraulic study to verify whether hydrogen migrates to the salt rock interior.

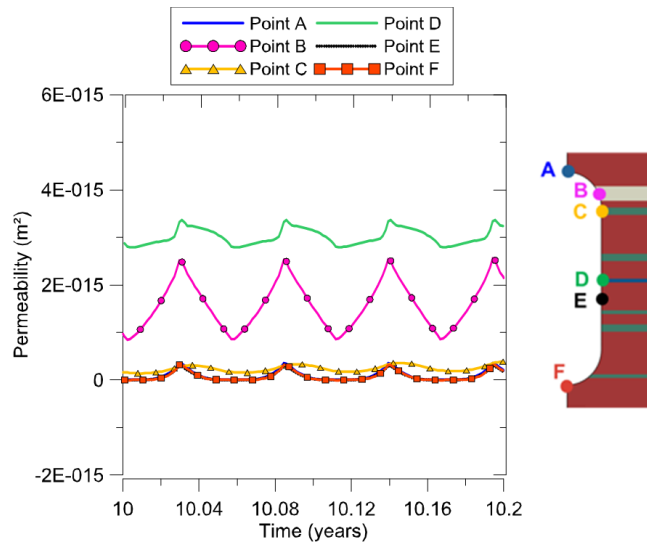


Figure 5.14 – Permeability evolution at different points.

Subsequently, a comparison between the heterogeneous and homogeneous models is performed and shown in Figure 5.15. We selected two points from the heterogeneous model: B and D, to have the permeability also evaluated in the homogeneous model.

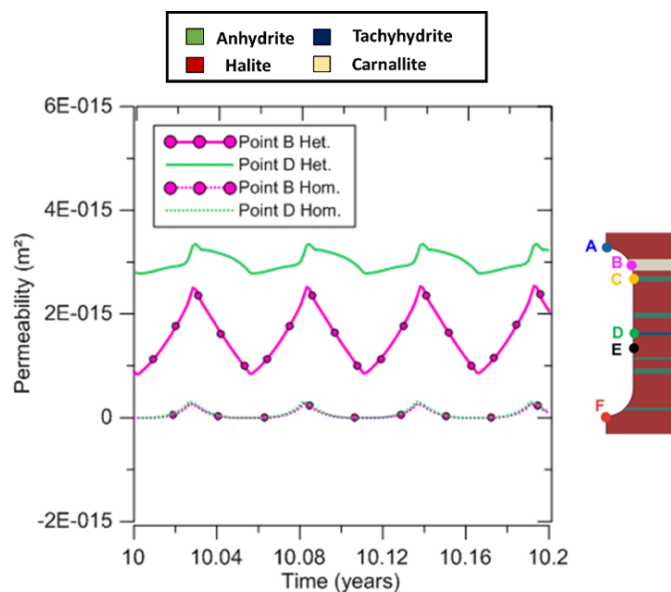


Figure 5.15 – Comparison of the permeability evolution at different points between the heterogeneous and homogeneous models.

The results highlight the importance of heterogeneities. Carnallite and tachyhydrite significantly increase the permeability in these regions, while the homogeneous model cannot represent it with fidelity. A similar conclusion was observed by Ramesh Kumar et al. (2021): a local heterogeneity in the domain, a large amount of deformation could occur, causing the failure of the salt cavern and permeability majorization.

The displacements were also monitored and are shown in Figure 5.16. Point B presented the higher absolute displacement among the salt rocks. One of the reasons is the relevant creep properties of carnallite and its location in this model, an area very propitious to accumulate stresses. On the other hand, point C had the lowest displacements, as expected. The creep properties of anhydrite are negligible; consequently, the displacements are minimal compared to other rocks. Tachyhydrite (point D) and halite (E) had almost the same displacements, which may be explained by their connection, like a sandwich structure. The displacements over the cavern lifespan are exhibited in Figure 5.17.

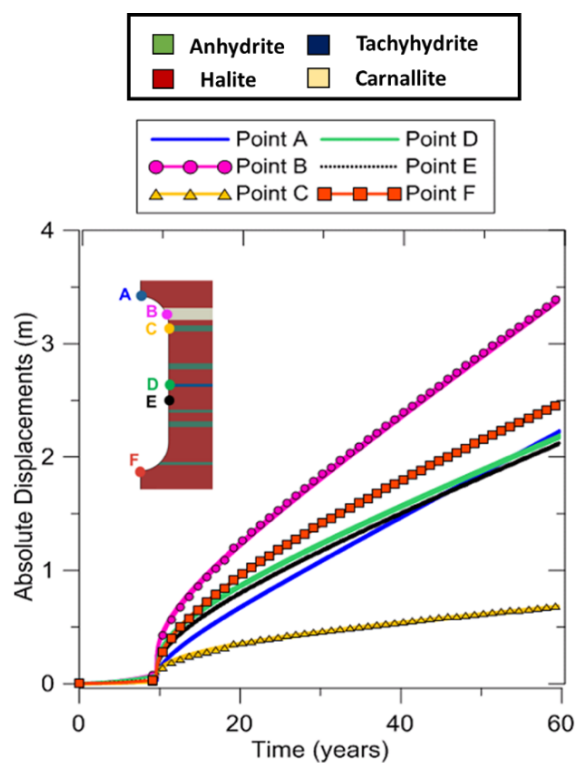
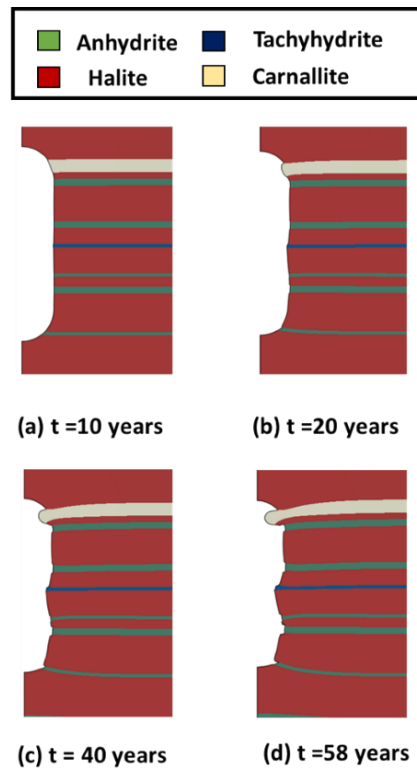


Figure 5.16 – Displacements at the different points.



**Note: Plot of displacements is scaled in 10x.**

Figure 5.17 – Displacements during the cavern lifespan

Despite the displacements being important to monitor the cavern's closure, another index provides the best understanding and comparison with the homogeneous model – the analysis of volume loss during the cavern's lifespan (approximately 60 years). According to Liu et al. (2020), the volume loss rate reflects the behaviors of stability, tightness, and serviceability of a salt cavern. Böttcher et al. (2017) point out the difficulty of assessing a reasonable value for the acceptable volume loss of a salt cavern. However, in the literature, we found it in the range of 5-20% (Khaledi et al. 2016a; Böttcher et al. 2017; Liu et al. 2020; Ramesh Kumar et al. 2021). Besides, the volume loss assumes relevance to maintaining the thermodynamic solution's applicability (Xia et al. 2015). Therefore, the volume loss (VL) can be expressed below:

$$VL = 1 - \frac{V}{V_0} \quad (5.6)$$

here,  $V$  is the volume measured during the current time of analysis and  $V_0$  is the volume before the operation given in Table 4.1. The process of collecting the node displacements and calculating the updated volume of the alt cavern is made through

a code developed in Python and MATLAB®. Thereby, the volume loss comparison is presented in Figure 5.18.

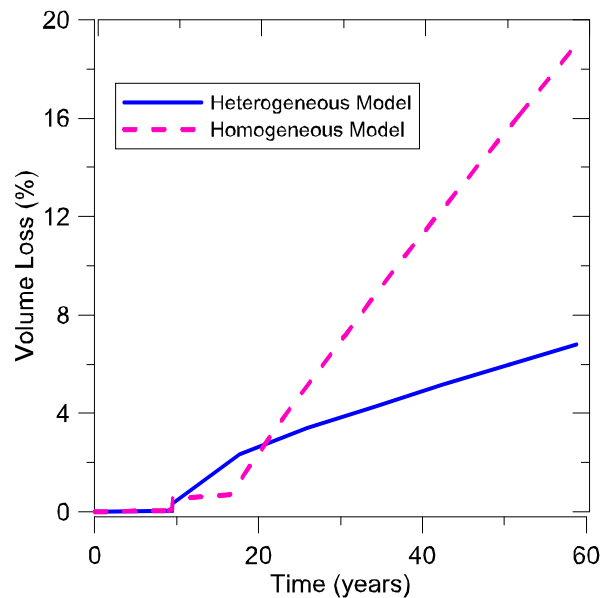


Figure 5.18 – Volume losses comparison.

The heterogeneities positively affect the cavern's closure: the anhydrite layers contribute to mitigating the creep response. Despite the several halite layers and the presence of some carnallite and tachyhydrite (as the structure is connected like a sandwich), we observe that the final displacements are lower than the homogeneous model (approximately 13% of difference). The homogeneous model had a volume loss of about 20%, representing a rate of 0.34% per year, not so much different from those found in the reference literature (Khaledi et al. 2016a; Böttcher et al. 2017; Wang et al. 2018; Liu et al. 2020; Ramesh Kumar et al. 2021).

### 5.1.5. Partial conclusions

From the heterogeneous model analysis, the main conclusions are:

- ✓ Anhydrite seems to have a beneficial effect regarding the cavern volume losses. Due to its low mobility, the entire system has reduced displacements. In this hypothesis, the cavern closure is expected to be less critical;
- ✓ However, the anhydrite layers plasticize in a significant extension ( $\approx 120$  m). Rock failure enhances the permeability in these areas, and gas leakage may

occur. As a direct consequence of leakages, the cavern will significantly depressurize, and the temperature will get colder (risk of tensile stresses);

- ✓ Carnallite and tachyhydrite have the highest mobility between the salt rocks. Regarding integrity, they can dissipate more stresses; consequently, neither tensile stresses nor dilatancy happens. The layer's permeability increases in these regions due to the relevant creep properties, and a hydraulic study is recommended to investigate the possibility of gas migration.
- ✓ The volume losses are higher in the homogeneous model, approximately 20%. The presence of anhydrite layers contributes positively to minimizing the tendency of the cavern closure in the heterogeneous model, which had a loss of about 7%, in consonance with the literature. On the other hand, the anhydrite tends to accumulate stresses and plasticizes;
- ✓ In terms of cavern operation, a cavern hosted in a heterogenous layer may require some points of attention: a) rocks with high mobility avoid plasticization, but the permeability is enhanced; b) anhydrite layers have reduced creep, which is beneficial for mitigating the volume losses. During a field application, if DI is close to 0.8-0.9, we recommend: 1) interrupting the cyclical storage scheme to dissipate effects accumulated during cycling and restore natural temperature levels; 2) increasing the cycle durations (accompanied by a reduction in mass fluxes) to reduce pressure and temperature rates.

## 5.2. Real salt cavern

Most salt cavern studies in the literature usually adopt a circular or capsular shape. Identifying the actual cavern geometry is not easy, as the sonar accuracy is typically 1%, according to Brouard et al. (2013). Another factor that makes it challenging to access salt cavern data is the monopoly of information by just a few companies and governments. In this thesis, we will adopt the shape provided by Liu et al. (2020).

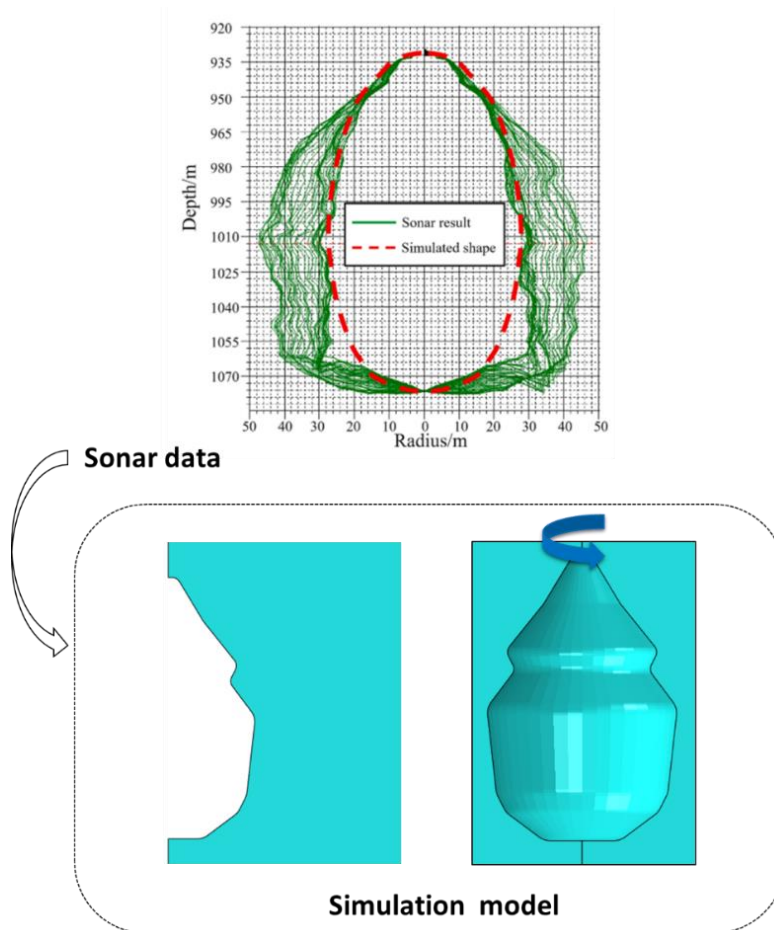


Figure 5.19 – Simulation model of the real salt cavern, based on Liu et al. (2020).

The adopted real salt cavern has a different shape from those simulated until now. There are points very propitious to concentrate stresses, such as concavities. We expected them with some problems regarding the rock integrity during the simulations.

### 5.2.1. Region for the salt cavern installation

The salt cavern will have the same premises presented in the fourth chapter regarding its installation area. The initial stress state as temperature assumes a representative scenario of the Santos Basin - Brazilian Pre-salt deep-water environment. The water depth is 2,000 m. The rock formation considers a 700 m overburden followed by 850 m of salt (halite), where the cavern is hosted. The cavern is situated within the interval of -3,050 to -3,200 m inside the halite layer. The slab protection at the top of the cavern is 350 m. The axisymmetric model is represented in Figure 5.20.

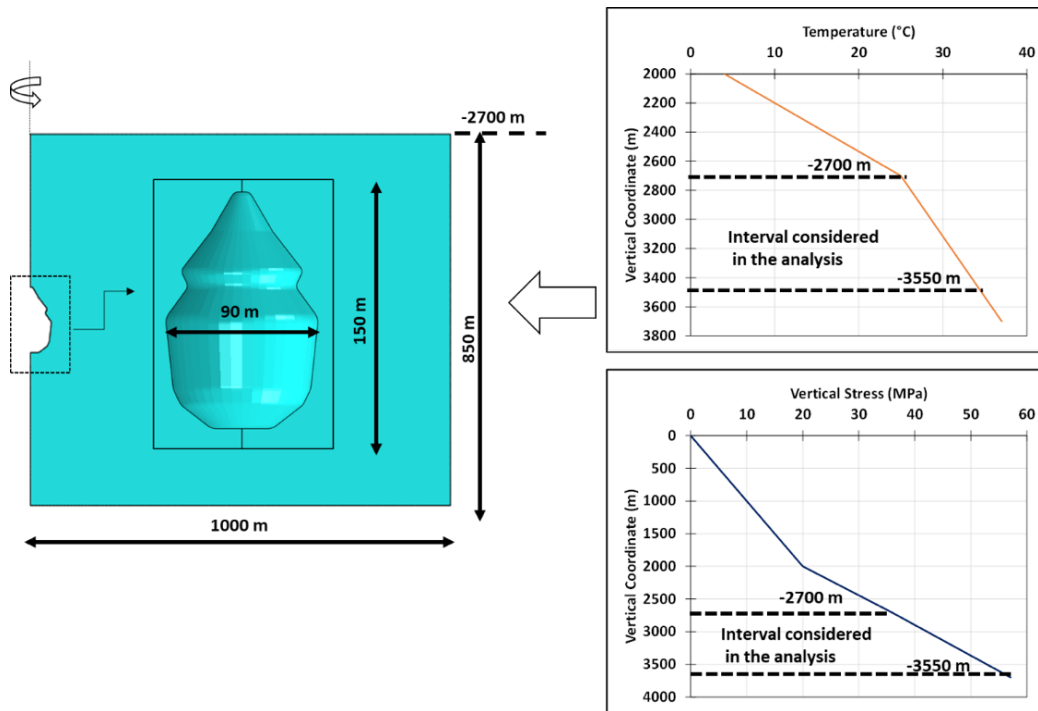


Figure 5.20 – Axisymmetric model of the real salt cavern.

### 5.2.2. Rock properties

The salt rock properties follow those in the Brazilian literature (Costa et al. 2005, 2011; Poiate 2012; Firme et al. 2014, 2018, 2019) and are given in Table 4.2. The parameters for the analytical solution for gas temperatures are presented in Table 5.4 (Xia et al. 2015; Zhu et al. 2017; Böttcher et al. 2017).

Table 5.4 – Material properties for salt rock and parameters for the analytical solution.

| Parameter                     | Unit                              | Value                |
|-------------------------------|-----------------------------------|----------------------|
| Density                       | kg.m <sup>-3</sup>                | 2040                 |
| Thermal Conductivity          | Wm <sup>-1</sup> K <sup>-1</sup>  | 7                    |
| Thermal expansion coefficient | K <sup>-1</sup>                   | 4 x 10 <sup>-5</sup> |
| Specific heat capacity        | Jkg <sup>-1</sup> K <sup>-1</sup> | 880                  |
| Heat transfer coefficient     | Wm <sup>-2</sup> K <sup>-1</sup>  | 1.2                  |
| Cavern surface area           | m <sup>2</sup>                    | 39,175               |
| Cavern volume                 | m <sup>3</sup>                    | 663,620              |
| Injection temperature         | K                                 | 333                  |

### 5.2.3. Load conditions

The load conditions follow those presented in Figure 4.8 for the pre-cyclic operation. Due to the reduced volume compared to the other examples, the leaching time is almost four times faster – only 2.5 years.

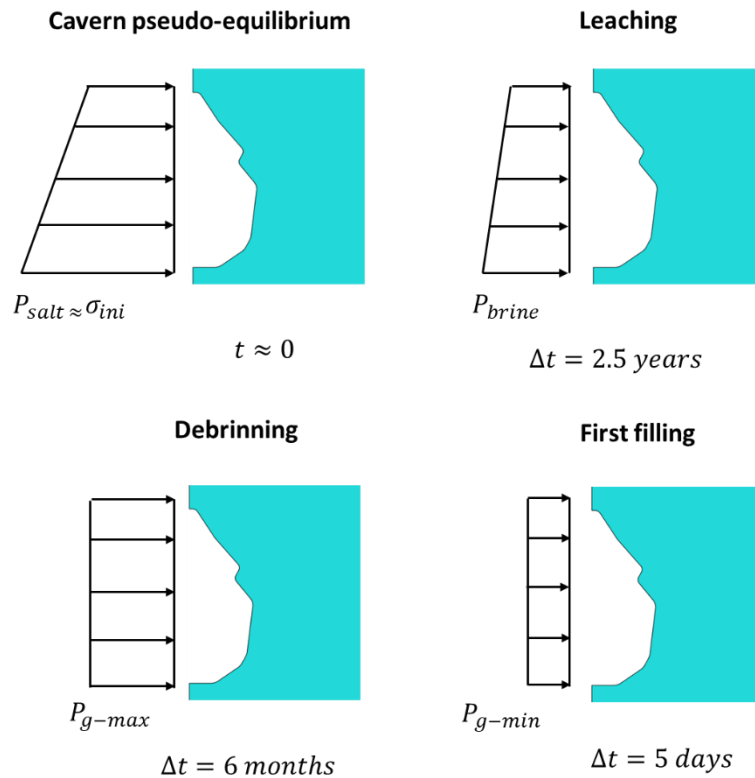


Figure 5.21 – Simulation steps and their assumptions.

Regarding the cyclic stage, we selected the hypothesis evaluated in case study 4, a cycle of 20 days with an injection pressure of 30 MPa - Figure 5.22. The thermal amplitude is 51°C, the highest among all the examples already simulated. The reduced volume of the salt cavern is the principal reason - it gets warm or cold very fast compared to the big caverns studied in the previous sections.

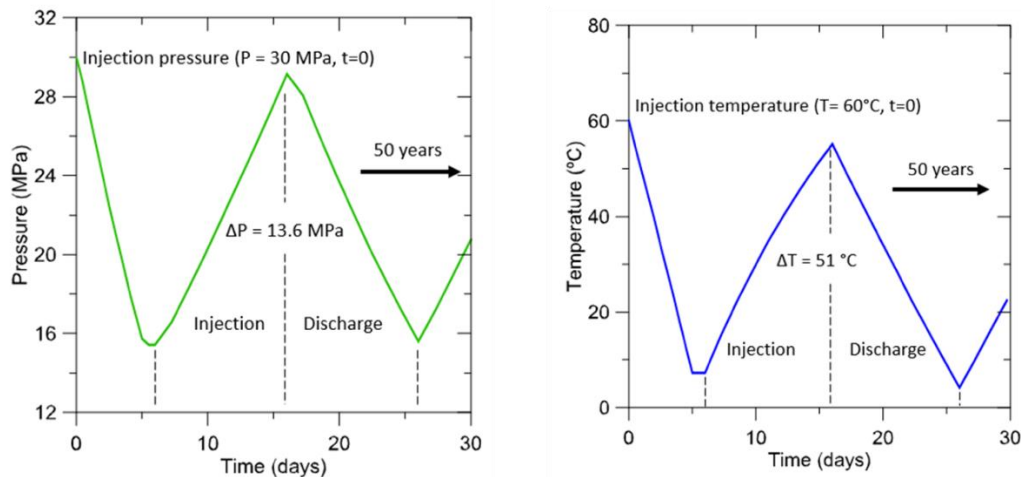


Figure 5.22 – Gas pressure and temperature along a cycle.

#### 5.2.4. Results and discussion

Five cavern points (A to E) will monitor the stresses, dilatancy index, permeability evolution, and displacements. The safety criteria are the same as in the previous examples. They are shown in Figure 5.23.

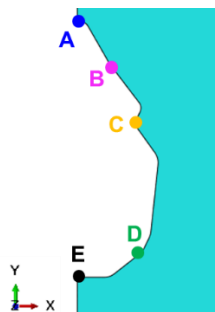


Figure 5.23 – Points of monitoring in the salt cavern.

The first results are shown in Figure 5.6. The maximum principal stress plot shows that almost all the points have positive stresses, which means tensile stresses occurring. Thus, the safety criteria of not having tensile stresses (Böttcher et al. 2017) was violated. Only point A remains in the compression domain, which may be explained by the soft transition at the cavern's roof, not propitiating considerable stress concentration. The real cavern also demonstrated the importance of considering the irregular shape: the tensile stresses are above 5 MPa, approximately three/four times the halite tensile strength (Poiate 2012).

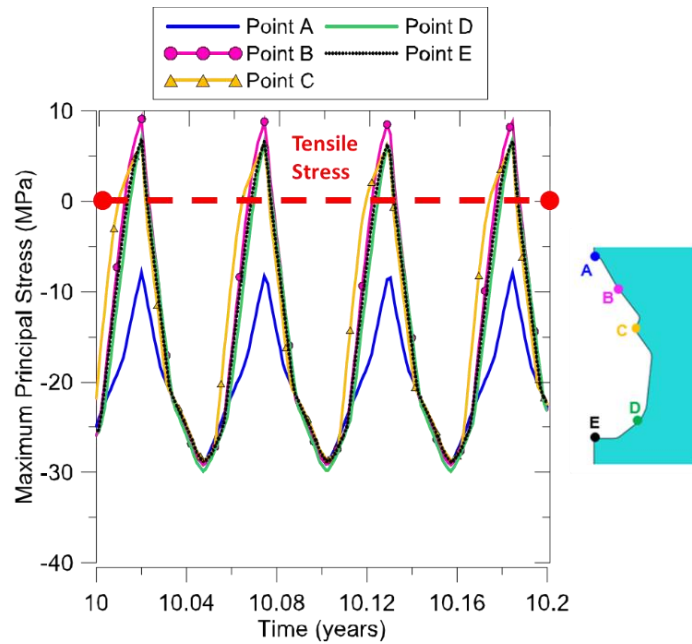


Figure 5.24 – Evaluated points in the salt cavern and axis orientation.

The stress trajectory ( $p \times q$ ) is plotted in Figure 5.25.

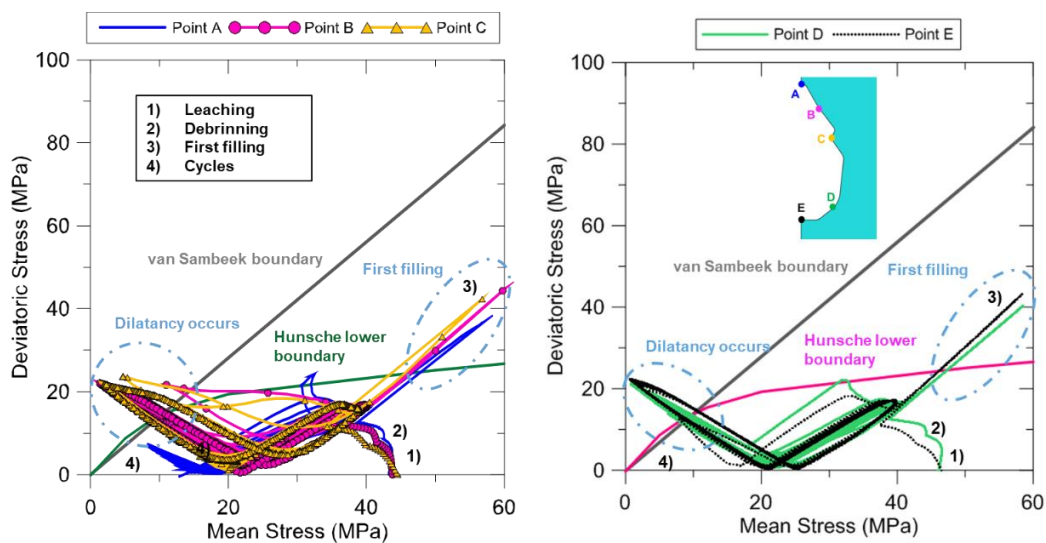


Figure 5.25 – Stress trajectory  $p \times q$  for points A to E.

We considered two dilatancy boundaries: the first was proposed by Van Sambeek, Ratigan, and Hansen (1993), and the second is the modified Hunsche lower boundary (Hunsche 1993), the pink line. During the first filling (when hydrogen is injected for the first time), all the monitored points crossed Hunsche's boundary limit. It occurs due to the fast temperature change at the cavern walls. Except for point A, all the other points crossed the dilatancy boundaries. It highlights how critical can be a real cavern due to its concavities and irregular

shape, which propitiates large stress concentration. The Dilatancy index plot is shown in Figure 5.26.

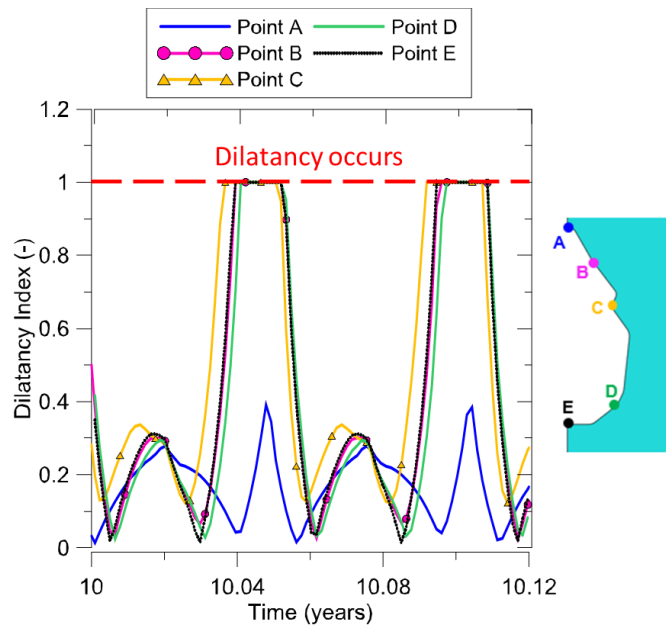


Figure 5.26 – Dilatancy index for points A to E.

Figure 5.27 shows a general overview of the dilatancy index during a cycle peak. The closer the value is to 1, the closer the current stress state is to exceeding the envelope limits.

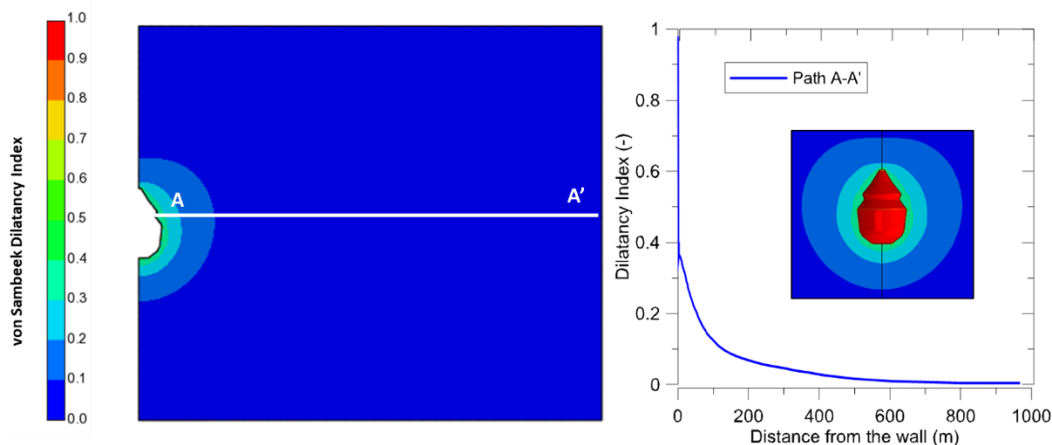


Figure 5.27 – Dilatancy index for points A to E.

The critical region is limited to the cavern wall, similar to the conclusions already achieved in chapter four. Therefore, the risk of failure along the host rock extension is minimized. It is also well-known that one of the most interesting characteristics of salt rock is its self-healing capacity, which may counter-balance damage. Figure 5.28 reinforces that only the wall is the region where most points

cross the dilatancy boundary. The stresses are dissipated at a significant distance from the cavern wall ( $\approx 100$  m), and the rock integrity is guaranteed.

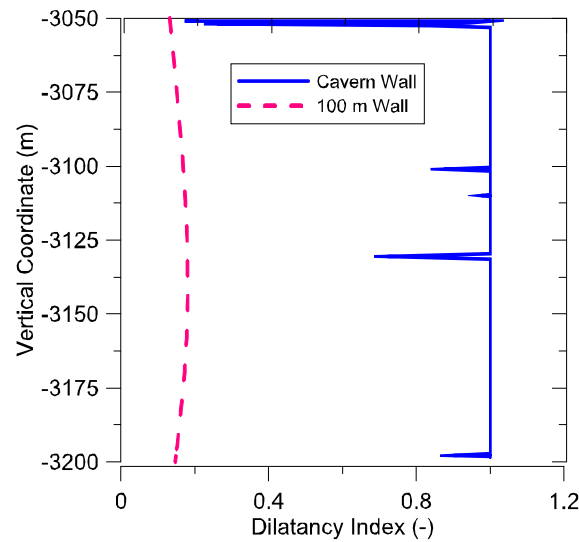


Figure 5.28 – Comparison of dilatancy for different distances from the wall.

The permeability evolution along a cycle is shown in Figure 5.29. As expected, point C is located at a region favorable to concentrate stresses and had the highest permeability increase. We also noted that the values are in the same range as those presented in chapter four (homogenous model). The next objective is to perform a hydraulic study to evaluate whether hydrogen propagates into the host rock.

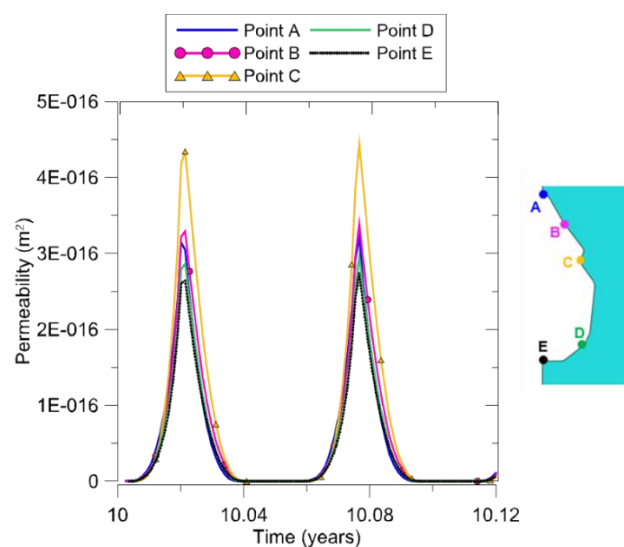


Figure 5.29 – Permeability evolution at different points.

The displacements for the five points are plotted in Figure 5.15.

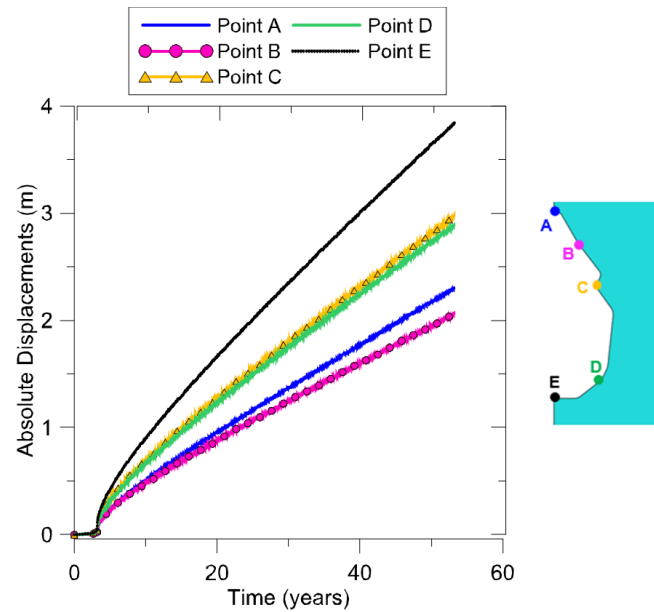


Figure 5.30 – Displacements at the different points.

Point E (basis) presented the highest absolute displacement, representing a strong tendency of closure from the basis. Point C, which concentrates stresses, also presented expressive displacements, approximately 3 m. In order to evaluate better how much volume the salt cavern has lost over the years, we provided the same methodology from the heterogeneous model to calculate it. The results are demonstrated in Figure 5.31.

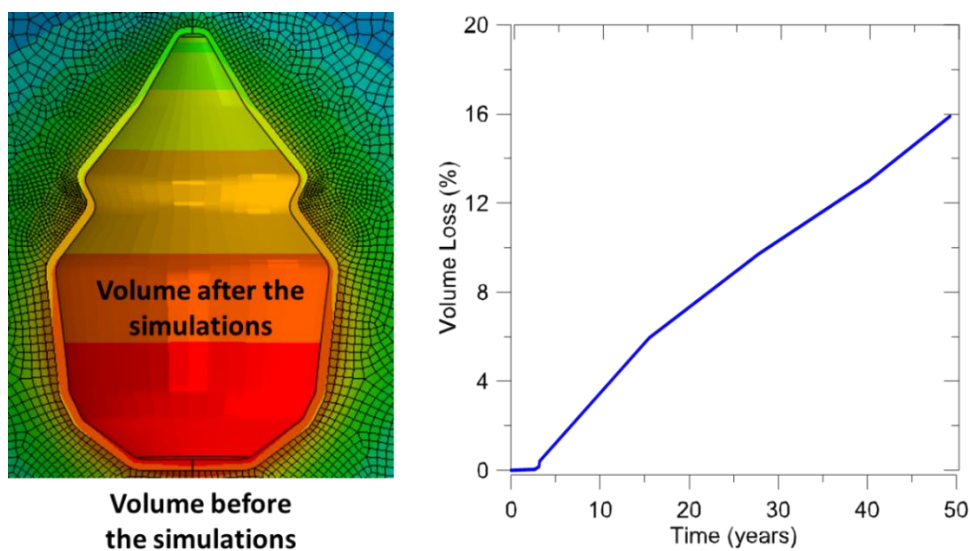


Figure 5.31 – Volume loss of the real salt cavern.

The total volume loss is about 16%, once again very close to those observed in the reference literature (Khaledi et al. 2016a; Böttcher et al. 2017; Wang et al. 2018; Liu et al. 2020; Ramesh Kumar et al. 2021). It indicates that the real salt

cavern remains under normal volume conditions compared to others worldwide.

### 5.2.5. Partial conclusions

From the real cavern analysis, the main conclusions are:

- ✓ Reduced salt cavern volume affects the thermal amplitude. It gets warm or cold very fast compared to the big caverns;
- ✓ From all the examples studied in this thesis, we observed that a minimum temperature of 15°C seems to be the limit for avoiding tensile stresses. The operator must constantly check the inputs from the thermodynamical simulator to control the temperature range;
- ✓ The critical areas (dilatancy or tensile stress) are limited to approximately one meter from the cavern wall. Thus, the possibility of gas migration into the host rock is significantly minimized;
- ✓ Considering a real cavern geometry makes it possible to evaluate better how the stresses and displacements impact its integrity during the cyclic stage. As demonstrated, determined areas are revealed to be more critical (point C) and warn that specific shapes must be monitored carefully with the support of the SONAR data. The tensile stresses were excessively high compared to the other examples, at least three times the halite limit (Poiate 2012). The cavern would be approved for operation under the following conditions: 1) interrupting the cyclical storage scheme to dissipate effects accumulated during cycling and restore natural temperature levels; 2) increasing the cycle durations (accompanied by a reduction in mass fluxes) to reduce pressure and temperature rates;
- ✓ The cavern's total volume loss was around 16%, in consonance with the average values in the reference literature. In this case, we do not expect significant problems with gas pressurization or operational volume losses.

### 5.3. Hydraulic analysis

The salt cavern literature often neglects the increase of salt rock's permeability (Costa et al. 2005, 2006, 2015; Poiate 2012; Abreu et al. 2023) or calculates it without further analysis to understand if the stored gas can migrate to the host rock (Khaledi et al. 2016b; Ramesh Kumar et al. 2021). As demonstrated during the homogeneous, heterogeneous, and real cavern model simulations, the permeability of salt rock changes and evolves along the cyclic operation. Resuming, we found the following values given in Table 5.5.

Table 5.5– Maximum permeabilities during the simulations.

| Case study | Description                              | Permeability (m <sup>2</sup> ) |
|------------|--|--------------------------------|
| 1          | 80-day cycle – Mechanical only           | 5 x 10 <sup>-18</sup>          |
| 2          | 80-day cycle - TM                        | 1.7 x 10 <sup>-16</sup>        |
| 3          | 20-day cycle - TM                        | 3.7 x 10 <sup>-16</sup>        |
| 4          | 20-day cycle with reduced pressure - TM  | 3.5 x 10 <sup>-16</sup>        |
| 5          | 320-day cycle - TM                       | 2 x 10 <sup>-17</sup>          |
| 6          | Heterogeneous model (cycles like case 4) | 3.5 x 10 <sup>-15</sup>        |
| 7          | Real cavern model (cycles like case 4)   | 4.2 x 10 <sup>-16</sup>        |

Thus, it urges a comprehensive study to analyze the gas migration into the host rock. This section will take the maximum permeability found during the several case studies,  $k = 3.5 \times 10^{-15} \text{ m}^2$ .

#### 5.3.1. Salt rock porosity

The salt rock porosity is calculated through the link between permeability and porosity given by the Kozeny-Carman (KC) model (Carman 1937). According to Chan et al. (2001), this model can be derived by assuming Hagen-Poiseuille flow through a network of tubular pores. Its equation is:

$$K = C_{KC} \left[ \frac{\varphi^3}{(1 - \varphi)^2} \right] \quad (5.7)$$

Where  $\varphi$  is the rock porosity and  $C_{KC}$  is a constant that will be defined, in this thesis, according to the WIPP calibration methodology - Chan et al. (2001). There, its value was  $1 \times 10^{-14} \text{ m}^2$ . Therefore, Figure 5.32 exhibits different permeabilities values calculated from the KC model.

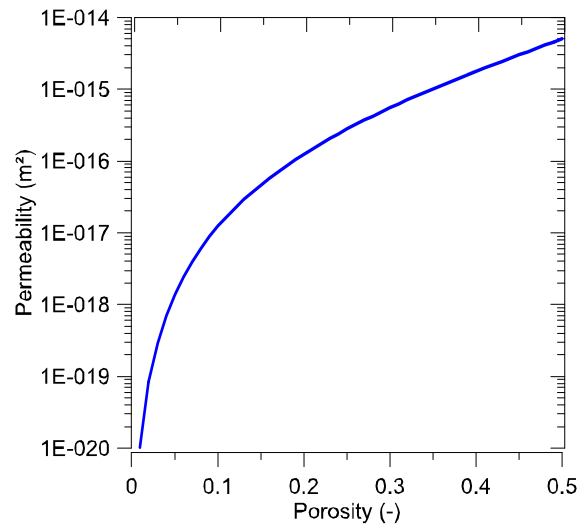


Figure 5.32 – Permeability and porosities according to the KC model.

Here, we want to obtain the updated salt rock porosity from a given permeability ( $3.5 \times 10^{-15} \text{ m}^2$ ), which leads to  $\varphi = 0.46$ . In fact, the permeability increase requires an update on porosity to reflect the hydraulic phenomenon accurately.

### 5.3.2. Salt rock and hydrogen hydraulic properties

The other salt rock and hydrogen properties were obtained from the reference literature (Weast and Astle 1984; Co 1988; Poiate 2012; Zivar et al. 2021), given in Table 5.6.

Table 5.6 – Salt rock and hydrogen properties.

| Parameter                 | Unit | Value                |
|---------------------------|------|----------------------|
| Young's modulus           | GPa  | 25.37                |
| Poisson's ratio           | -    | 0.36                 |
| Bulk Modulus of salt rock | GPa  | 30                   |
| Bulk Modulus of hydrogen  | kPa  | 140                  |
| Viscosity of hydrogen     | Pa.s | $8.9 \times 10^{-6}$ |

### 5.3.3. Load conditions and simulation details

We highlight that the hydraulic analysis does not run simultaneously with the thermomechanical one. It is not a thermo-hydro-mechanical (THM) coupling. After the TM simulation and calculating the permeability, the subsequent step is to

run the hydraulic analysis with: a) maximum permeability obtained, b) updated porosity, and c) pore pressure based on the gas pressure from the thermodynamic simulator. The flowchart in Figure 5.33 resumes the process of analysis.

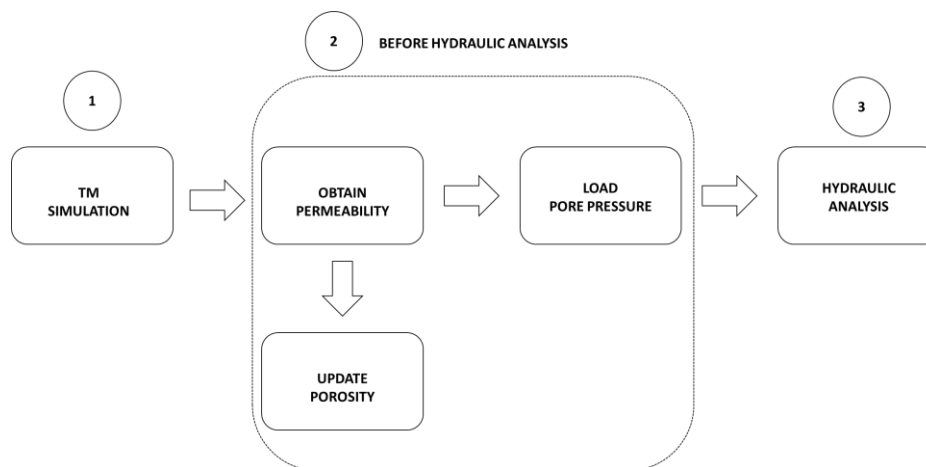


Figure 5.33 – Process to run the hydraulic analysis.

The inputted pore pressure follows the one presented for case study 4 in the fourth chapter. It represents the most critical case simulated in all the examples, as tensile stresses occurred and the permeability significantly increased. The gas flow into the host rock is evaluated under 50 years. Initially, the permeability is considered to be constant during all the analysis and the same along the entire model (critical hypothesis).

#### 5.3.4. Results and discussion

The pore pressure disturbance around the salt rock medium is shown in Figure 5.34. The region is very limited to the cavern walls, indicating a reduced risk of gas migration into the host rock. At approximately 20 m from the wall, the pore pressure tends to stabilize to the initial conditions ( $P \approx 0$ ). Considering the horizontal model extension ( $L = 1000$  m), only 2% of the length has some disturbance. These conclusions match the ones presented by Grgic et al. (2022). The authors pointed out that fractures and increased permeability close to the cavern wall could promote hydrogen leakage because the excavation induces high deviatoric stress and the gas pressure (high-frequency) cycles. However, during the experimental tests with salt rock samples, they observed that the thickness of this excavation-damaged zone is relatively small. The self-recovery from damage allied

to the good creep properties of rock salt also prevents any significant long-term permeability increase. The laboratory analysis demonstrated that the gas leakage through cavern walls should be negligible and is expected to have an excellent perspective for the future exploitation of salt caverns for UHS.

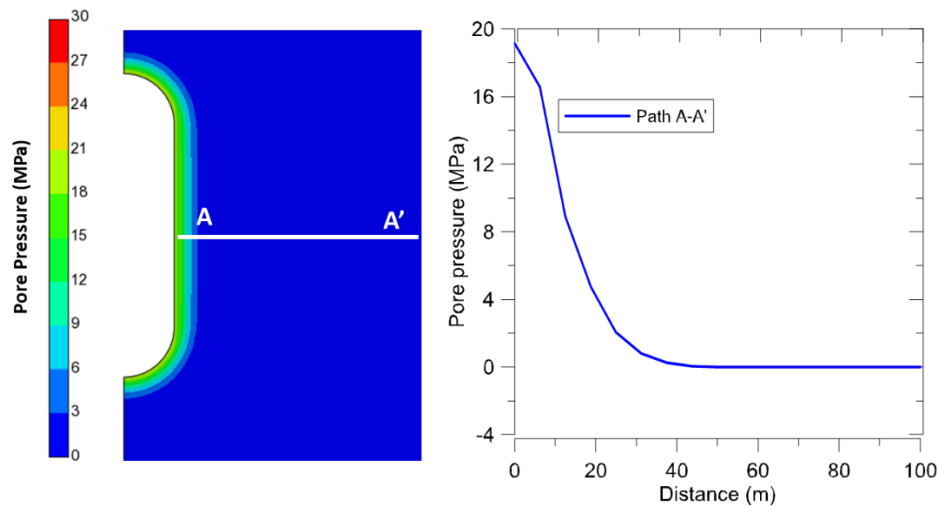


Figure 5.34 – Pore pressure variation during the hydraulic analysis ( $t = 50$  years).

Finally, Figure 5.35 exhibits the pore pressure distribution during the cavern lifespan. The pore pressure starting point may vary according to the time, as demonstrated during the hydrogen pressure plot in Figure 4.10. During the first years, pore pressure is slightly negative (suction) due to the medium disturbance and high cycle frequency. Over the years, this effect is dissipated, and the pore pressure changing zone increases until an extension of about 20 m from the wall. As already discussed, the possibility of gas migration into the host rock is small. Thereby, the salt cavern can be considered safe for exploitation.

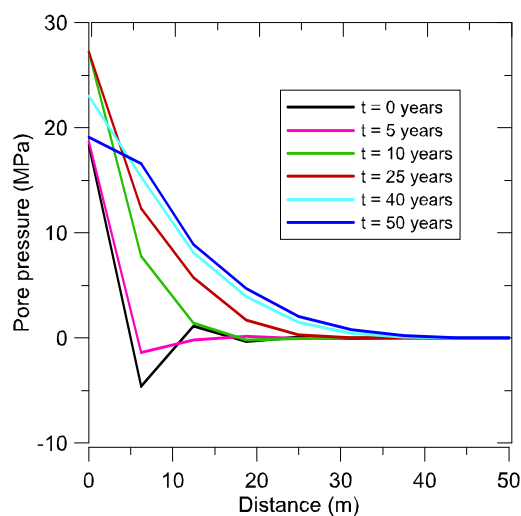


Figure 5.35 – Pore pressure variation during the hydraulic analysis ( $t = 50$  years).

### 5.3.5. Partial conclusions

The hydraulic study provided further comprehension regarding the possibility of gas leakages into the salt rock. The main conclusions are:

- ✓ There was a gap in the geomechanical literature about the effect of the permeability increase on gas-rock interaction;
- ✓ The hydraulic study overcame this gap and made it possible to understand that the maximum permeability obtained ( $3.5 \times 10^{-15} \text{ m}^2$ ) did not affect the medium sealability. After 50 years of simulation, the pore pressure disturbance zone was only 20 m from the cavern wall (approximately 2% of the model extension).
- ✓ These conclusions are on the same line as those presented by Grgic et al. (2022), which provided a series of laboratory analyses with salt rock samples under different loading conditions. The authors observed a minimal area where the permeability changed and the simultaneous effect of self-healing counter-balancing damage. Thus, the risk of gas leakage can be considered negligible.

## 6 Conclusions

This thesis brought an innovative exploration perspective to the pre-salt fields: underground hydrogen storage. Hydrogen is a powerful energy source used in the USA and Europe to supply different economic sectors.

Analyzing Brazilian's perspectives, the expertise acquired from exploring wells in the pre-salt fields is a differential to make this challenging project possible once operations in ultra-deep waters require advanced engineering techniques and simulations. For example, the proposed UHS salt caverns would be the deepest in the world, putting Brazil into a protagonist role in the future hydrogen market. From an economic aspect, this work highlights some advantages in adopting salt caverns as hydrogen storage: a) the possibility of multiple cycles per year, turning it into a rentable option to match the market demands, and b) less concern about gas leakage, minimizing the necessary investments to guarantee site tightness.

This research covered the entire lifespan of a salt cavern: from construction to the operational stage. The thermodynamical simulator provided the updated hydrogen temperature and pressure as input to the GeMA framework, allowing analysis with similar conditions to those found in the field, which overcame a gap in the Brazilian literature of focusing exclusively on the mechanical aspects of gas storage. Regarding the geomechanical analysis of hydrogen storage in pre-salt caverns, this is the first study to provide a complete discussion of different aspects, such as the effect of inhomogeneities in the salt rock layers.

The study demonstrated that the mechanical analysis underestimates the stresses leading to an unrealistic scenario when short cycles of hydrogen storage are adopted. Thus, some risk conditions are ignored if we only consider the mechanical aspects. For example, the maximum principal stress in the mechanical simulation results in compressive states. However, tension stresses arise with the TM coupling. Thus, a purely mechanical solution is inadequate. Further, this work showed how the different injection/discharge cycles might affect cavern integrity: the results evidenced that shorter cycles provoke higher temperature amplitudes and

increase damage and leakage risks - Dias et al. (2023). The gas injection pressure also plays an important role. A 10 % reduction of the injection pressure induced tensile stresses, dilatancy, and significantly increased cavern closure, approximately 100 % at point A. The disturbed zone was 185 m into the rock mass in the most critical case. However, the area where the dilatancy index achieved the limit of 1.0 is restricted to the cavern wall. On the other hand, longer cycles have a negligible impact on temperature amplitudes, and the analysis gives almost the same results as the mechanical one. Temperature amplitudes also affect permeability, which follows Peach's criterion (Peach 1991), based on a power law of the volumetric strain. The numerical results demonstrate that permeability significantly increases during TM simulations. However, the literature is inconclusive if this permeability increase will compromise the cavern tightness. Subsequent research was provided in this thesis to answer the question.

In order to understand how inhomogeneities in the salt layer could affect rock integrity, we selected the log file from well 9-BRSA-716-RJS in the Lula Field, part of the Santos Basin. We observed that the anhydrite layers seem to have a beneficial effect regarding the cavern volume losses. Due to its low mobility, the entire system has reduced displacements. In this hypothesis, the cavern closure is expected to be less critical. However, the anhydrite layers plasticized in a significant extension ( $\approx 120$  m). Rock failure enhances these areas' permeability, and gas leakage may occur. Carnallite and tachyhydrite have the highest mobility between the salt rocks and dissipate more stresses. Consequently, neither tensile stresses nor dilatancy happens. The layer's permeability increases in these regions due to the relevant creep properties. A comparison with a homogeneous model was provided to comprehend better the real impact of different salt layers in the results. The conclusions indicate that volume losses are higher in the homogeneous model, approximately 20%. The presence of anhydrite layers contributes positively to minimizing the tendency of the cavern closure in the heterogeneous model, which had a loss of about 7%, in consonance with the literature (Khaledi et al. 2016a; Böttcher et al. 2017; Wang et al. 2018; Liu et al. 2020; Ramesh Kumar et al. 2021). From a field perspective, the inhomogeneities reduce the volume losses when there are many anhydrite layers. It is beneficial for avoiding overpressurization and

maintaining hydrogen under normal working conditions. However, high-mobility salt rocks are a warning regarding creep response and permeability enhancement.

The importance of considering a real cavern geometry was also highlighted in this research. The example followed the geometry presented by Liu et al. (2020), a very irregular shape based on SONAR data. From the thermodynamics perspective, we noted that this small cavern had a higher temperature amplitude than the other models due to its reduced volume and surface area. It gets cold or warm fastly. As expected, the concavities accumulated stresses and dilatancy occurs in different regions of the salt cavern. From an operational perspective, avoiding such irregularities during the cavern construction is recommended. The extension of this critical area (dilatancy or tensile stress) is limited to approximately one meter from the cavern wall. Thus, the possibility of gas migration into the host rock is minimized. The cavern's total volume loss was around 16%, not so much different from the others presented in the literature (Böttcher et al. 2017).

Although some salt cavern literature has monitored the permeability enhancement (Khaledi et al. 2016b; Ramesh Kumar et al. 2021), it remains a gap in evaluating if this majorization is significant or not to compromise the medium sealability. This thesis conducted a hydraulic study to answer this question: the main objective is to assess whether the hydrogen propagates into the host rock and the correspondent extension. We selected the maximum permeability obtained ( $3.5 \times 10^{-15} \text{ m}^2$ ) during the simulations and considered a total time of 50 years. The results evidenced that the pore pressure disturbance zone was only 20 m from the cavern wall (approximately 2% of the model extension). These conclusions follow those Grgic et al. (2022) reached during a series of laboratory analyses with salt rock samples under different loading conditions. The authors observed a minimal area where the permeability changed and the simultaneous effect of self-healing counter-balancing damage. The risk of gas leakage can be considered negligible. Therefore, the hydraulic study provides more confidence to explore the salt caverns, and it overcomes an existing gap in the literature related to understating how the gas propagates and its effects on medium sealability. Resuming, these are the following contributions/innovations of this Ph.D. Thesis:

- ✓ A complete workflow for checking the salt cavern integrity covering the entire process: construction to operation. It is the first simulation of this type (hydrogen storage) realized in Brazil;  
The gas pressure and temperature are updated at each time step based on a thermodynamic solution. These inputs from the thermodynamic simulator are incorporated into the GeMA framework and provide a simulation close to the conditions that will occur during cavern operation;
- ✓ Extensive report considering different time cycles, which cover a range of future strategies for Brazil;
- ✓ Analysis of a salt cavern excavated into a heterogeneous layer (real data from well 9-BRSA-716-RJS situated in the Lula Field);
- ✓ Results for a real cavern geometry (based on SONAR data) and its effects on simulation;
- ✓ Investigating permeability increase in salt caverns and the consequences based on a hydraulic simulation (TM + H coupling);

This research could enhance new perspectives for pre-salt exploration, such as hydrogen storage in salt caverns. The different case studies approached in this thesis covered extensive scenarios that will undoubtedly be found during cavern operation. Some existing gaps in the literature could be clarified or finally answered, for example, the effect of permeability evolution on the medium integrity from a hydraulic simulation. As a subsequent step in this research line, we recommend a deep study of the following points:

- a) An improvement on the constitutive model for creep in salt rock: including the tertiary stage. The tertiary creep considers damage and could provide a better understanding of the dilatancy evolution in salt rocks;
- b) Assessment of the abandonment of hydrogen salt caverns: different techniques and how they could affect the medium integrity and sealability;
- c) The effect of multiple caverns: is there a minimum distance between them to guarantee safe operation? In addition, we recommend evaluating the impact of caverns running into different cycle frequencies;

- d) Experimental studies with Brazilian salt rocks to provide further comprehension of its permeability evolution and perform advanced studies with coupled physics (THM analysis).

## References

- ABAQUS A. 6.11 Theory Manual. Dessault Syst. 2011;
- Abreu JF, Costa AM, Costa PVM, Miranda ACO, Zheng Z, Wang P, et al. Carbon net zero transition: A case study of hydrogen storage in offshore salt cavern. *J Energy Storage*. 2023 Jun 1;62:106818.
- Aftab A, Hassanpouryouzband A, Xie Q, Machuca LL, Sarmadivaleh M. Toward a Fundamental Understanding of Geological Hydrogen Storage. *Ind Eng Chem Res* [Internet]. 2021 [cited 2022 Apr 12];2022:3233–53. Available from: <https://pubs.acs.org/doi/abs/10.1021/acs.iecr.1c04380>
- Alkan H. Percolation model for dilatancy-induced permeability of the excavation damaged zone in rock salt. *Int J Rock Mech Min Sci*. 2009;46(4):716–24.
- de Almeida AS, de Tarso Cerqueira Lima S, Rocha PS, de Andrade AM, Branco CC, Pinto AC. CCGS Opportunities in the Santos Basin Pre-Salt Development [Internet]. *SPE International Conference on Health, Safety and Environment in Oil and Gas Exploration and Production*. 2010. p. SPE-126566-MS. Available from: <https://doi.org/10.2118/126566-MS>
- Altenbach H. Topical problems and applications of creep theory. *Int Appl Mech* [Internet]. 2003 [cited 2019 Mar 20];39(6):631–55. Available from: <http://link.springer.com/10.1023/A:1025737707488>
- Alves TM, Fetter M, Lima C, Cartwright JA, Cosgrove J, Gangá A, et al. An incomplete correlation between pre-salt topography, top reservoir erosion, and salt deformation in deep-water Santos Basin (SE Brazil). *Mar Pet Geol* [Internet]. 2017 Jan 1 [cited 2022 Apr 14];79:300–20. Available from: <http://creativecommons.org/licenses/by/4.0/>
- An H, Wilhelm WE, Searcy SW. Biofuel and petroleum-based fuel supply chain research: A literature review. *Biomass and Bioenergy*. 2011 Oct;35(9):3763–74.
- Andersson J, Grönkvist S. Large-scale storage of hydrogen. *Int J Hydrogen Energy* [Internet]. 2019 May 3 [cited 2022 May 9];44(23):11901–19. Available from: <https://doi.org/10.1016/j.ijhydene.2019.03.063>
- Aydan Ö. *Time-Dependency in Rock Mechanics and Rock Engineering* [Internet]. Vol. 91. CRC Press; 2017. Available from: <https://www.taylorfrancis.com/books/9781498777001>
- Baar CA. *Applied Salt-Rock Mechanics 1 .The in-situ behavior of salt rocks*. Elsevier. 1977;294.
- Bardelin C. Impactos do Racionamento de Energia Elétrica de 2001 e 2002 no Brasil [Internet]. 2003. Available from: <http://www.seeds.usp.br/pir/arquivos/congressos/CLAGTEE2003/Papers/EU E B-066.pdf>
- Bays CA. Use of salt solution cavities for underground storage. In: *Symp Salt North Ohio Geol Soc*. 1963. p. 564–78.
- Bérest P. Heat transfer in salt caverns. *Int J Rock Mech Min Sci* [Internet]. 2019 Aug 1 [cited 2022 Apr 8];120:82–95. Available from: <https://doi.org/10.1016/j.ijrmms.2019.06.009>
- Bérest P, Bergues J, Brouard B, Durup JG, Guerber B. A salt cavern abandonment

- test. *Int J Rock Mech Min Sci*. 2001 Apr 1;38(3):357–68.
- Beutel T, Black S. Salt deposits and gas cavern storage in the UK with a case study of salt exploration from Cheshire. *Oil Gas Eur Mag*. 2005;1(2005):31–5.
- Botelho FVC. Análise Numérica do Comportamento Mecânico do Sal Em Poços de Petróleo [Internet]. [Rio de Janeiro, Brazil]: PPontifícia Universidade Católica do Rio De Janeiro; 2008. Available from: [http://www.maxwell.vrac.puc-rio.br/Busca\\_etds.php?strSecao=resultado&nrSeq=12391@1](http://www.maxwell.vrac.puc-rio.br/Busca_etds.php?strSecao=resultado&nrSeq=12391@1)
- Böttcher N, Görke U-J, Kolditz O, Nagel T. Thermo-mechanical investigation of salt caverns for short-term hydrogen storage. *Environ Earth Sci* [Internet]. 2017 Feb 23 [cited 2022 Apr 8];76(3):98. Available from: <http://link.springer.com/10.1007/s12665-017-6414-2>
- Boucher, M, Boucly, P, and Carriere JF. Mechanical behaviour problems encountered in the creation and control of salt cavern storage. In: 14th Int Gas Union World Gas Conf Prepr; (Canada). 14th Int. Gas Union World Gas Conf. Prepr.(Canada); 1979.
- Britto EC de. Rochas Evaporíticas e sua Caracterização através de Perfis em Poços de Petróleo. Universidade Fderal da Bahia; 2013.
- Brouard B, Bérest P, De Greef V, Béraud JF, Lheur C, Hertz E. Creep closure rate of a shallow salt cavern at Gellenoncourt, France. *Int J Rock Mech Min Sci*. 2013 Sep 1;62:42–50.
- Caglayan DG, Weber N, Heinrichs HU, Linßen J, Robinius M, Kukla PA, et al. Technical potential of salt caverns for hydrogen storage in Europe. *Int J Hydrogen Energy* [Internet]. 2020 Feb 28 [cited 2022 Apr 19];45(11):6793–805. Available from: [www.sciencedirect.com](http://www.sciencedirect.com)
- Cai Z, Zhang K, Guo C. Development of a novel simulator for modelling underground hydrogen and gas mixture storage. *Int J Hydrogen Energy* [Internet]. 2022 Feb 15 [cited 2022 Apr 12];47(14):8929–42. Available from: [www.sciencedirect.com](http://www.sciencedirect.com)
- Carman PC. Fluid flow through a granular bed. *Trans Inst Chem Eng London*. 1937;15:150–6.
- Cella PRC, da Silva A, Azuaga L. Desenvolvimento e execução de ensaios triaxiais de fluência estacionária em rocha salina sob altas pressões e temperaturas. 2003;
- Chan KS, Bodner SR, Fossum AF, Munson DE. A constitutive model for inelastic flow and damage evolution in solids under triaxial compression. *Mech Mater*. 1992;14(1):1–14.
- Chan KS, Bodner SR, Munson DE. Permeability of WIPP Salt during Damage Evolution and Healing. *Int J Damage Mech* [Internet]. 2001a Oct 13 [cited 2019 Feb 6];10(4):347–75. Available from: <https://journals.sagepub.com/doi/pdf/10.1106/H3UV-1URA-AFUY-FX49>
- Chan KS, Bodner SR, Munson DE. Permeability of WIPP Salt during Damage Evolution and Healing. *Int J Damage Mech* [Internet]. 2001b Oct 13 [cited 2019 Feb 6];10(4):347–75. Available from: <https://journals.sagepub.com/doi/pdf/10.1106/H3UV-1URA-AFUY-FX49>
- Chan KS, Brodsky NS, Fossum AF, Bodner SR, Munson DE. Damage-induced nonassociated inelastic flow in rock salt. *Int J Plast*. 1994;10(6):623–42.
- Chen F, Ma Z, Nasrabadi H, Chen B, Saad Mehana MZ, Van Wijk J. Capacity assessment and cost analysis of geologic storage of hydrogen: A case study in Intermountain-West Region USA. *Int J Hydrogen Energy* [Internet]. 2023

- Mar;48(24):9008–22. Available from: <https://linkinghub.elsevier.com/retrieve/pii/S0360319922056348>
- Chen J, Jiang D, Ren S, Yang C. Comparison of the characteristics of rock salt exposed to loading and unloading of confining pressures. *Acta Geotech* [Internet]. 2016 Feb 3 [cited 2018 Nov 14];11(1):221–30. Available from: <https://link.springer.com/content/pdf/10.1007%2Fs11440-015-0369-9.pdf>
- Chen J, Ren S, Yang C, Jiang D, Li L. Self-Healing Characteristics of Damaged Rock Salt under Different Healing Conditions. *Materials (Basel)* [Internet]. 2013 Aug 12;6(8):3438–50. Available from: <http://www.mdpi.com/1996-1944/6/8/3438>
- Chen W-F, Han D-J. *Plasticity for structural engineers*. J. Ross publishing; 2007.
- Chromik M, Korzeniowski W. A Method to Increase the Leaching Progress of Salt Caverns with the Use of the Hydro-Jet Technique. *Energies* [Internet]. 2021 Sep 15;14(18):5833. Available from: <https://www.mdpi.com/1996-1073/14/18/5833>
- CNBC. How salt caverns may trigger \$11 trillion hydrogen energy boom [Internet]. 2020 [cited 2022 Apr 14]. Available from: <https://www.cnbc.com/2020/11/01/how-salt-caverns-may-trigger-11-trillion-hydrogen-energy-boom-.html>
- Co C. *Flow of fluids through valves, fittings, and pipe*. Crane Company; 1988.
- COPPE. Hybrid Hydrogen Bus | COPPE [Internet]. 2012 [cited 2022 Apr 12]. Available from: <https://www.coppe.ufrj.br/en/a-coppe/coppe-produtos/hybrid-hydrogen-bus>
- Costa AM. *Uma Aplicação de Métodos Computacionais e Princípios de Mecânica das Rochas no Projeto e Análise de Escavações Destonadas à Mineração Subterrânea*. Universidade Federal do Rio de Janeiro; 1984.
- da Costa AM, Amaral CS, Poiate E, Pereira AMB, Martha LF, Gattass M, et al. Underground Storage of Natural Gas and CO<sub>2</sub> in Salt Caverns in Deep and Ultra-Deep Water Offshore Brazil. 12th ISRM Congress. 2011. p. ISRM-12CONGRESS-2011-300.
- Costa AM, Poiate E, Amaral CS, Pereira A, Martha LF, Gattass M, et al. GEOMECHANICS APPLIED TO THE WELL DESIGN THROUGH SALT LAYERS IN BRAZIL: A HISTORY OF SUCCESS. In: *Springer Series in Geomechanics and Geoengineering* [Internet]. 2011. p. 165–8. Available from: [http://link.springer.com/10.1007/978-3-642-19630-0\\_42](http://link.springer.com/10.1007/978-3-642-19630-0_42)
- Costa AM, Poiate J. E, Falcão JL, Coelho LFM. Triaxial Creep Tests in Salt Applied in Drilling Through Thick Salt Layers in Campos Basin-Brazil. In: *SPE/IADC Drilling Conference*. Society of Petroleum Engineers; 2005.
- Costa AM, Poiate Jr. E, Falcao J. Well Design for Drilling Through Thick Evaporite Layers in Santos Basin—Brazil. In: *Proceedings of IADC/SPE Drilling Conference* [Internet]. Society of Petroleum Engineers; 2006. p. 16. Available from: <http://www.spe.org/elibrary/servlet/spepreview?id=SPE-99161-MS>
- Costa PVM, Costa AM, Poiate Jr E, Amaral CS, Pereira AMB. Computer Modeling Applied in the Design of Underground Salt Caverns Opened by Solution Mining for Gas Storage. 49th U.S. Rock Mechanics/Geomechanics Symposium. 2015. p. ARMA-2015-393.
- Da Costa PVM. *POTENCIAL DE ESTOCAGEM SUBTERRÂNEA DE GÁS NATURAL EM CAVERNAS DE SAL ABERTAS POR DISSOLUÇÃO EM DOMO SALINO OFFSHORE NO BRASIL*. Federal University of Rio de Janeiro; 2015.

- Da Costa PVM. Potencial de Estocagem Subterrânea de Gás Natural em Cavernas de Sal Abertas por Dissolução em Domo Salino Offshore no Brasil [Internet]. 2018. Available from: <http://www.ppe.ufrj.br/images/publicações/doutorado/PVassalo.pdf>
- DeVries KL, Mellegard KD, Callahan GD, Goodman WM. Cavern roof stability for natural gas storage in bedded salt. 2005.
- Dias W, Roehl D, Mejia C, Sotomayor P. Cavern integrity for underground hydrogen storage in the Brazilian pre-salt fields. *Int J Hydrogen Energy* [Internet]. 2023 Apr; Available from: <https://linkinghub.elsevier.com/retrieve/pii/S0360319923014155>
- EERE ENERGY. Hydrogen Fuel Cell Engines MODULE 1: HYDROGEN PROPERTIES CONTENTS [Internet]. 2001 [cited 2022 Apr 13]. Available from: [https://www1.eere.energy.gov/hydrogenandfuelcells/tech\\_validation/pdfs/fcm01r0.pdf](https://www1.eere.energy.gov/hydrogenandfuelcells/tech_validation/pdfs/fcm01r0.pdf)
- ENGIE. H2 in the underground: Are salt caverns the future of hydrogen storage? | ENGIE Innovation [Internet]. 2021 [cited 2022 Apr 8]. Available from: <https://innovation.engie.com/en/articles/detail/hydrogene-souterrain-stockage-sel-cavites-mines/25906/12/1>
- EPA U. Global Greenhouse Gas Emissions Data | US EPA [Internet]. [cited 2022 Apr 13]. Available from: <https://www.epa.gov/ghgemissions/global-greenhouse-gas-emissions-data>
- Fairhurst C, St. John CM, Midea NF, Eston SM, Fernandes AC, Bongiovanni LA. Rock Mechanics studies of proposed underground mining of potash in Sergipe, Brazil. 4th ISRM Congr. 1979 Jan 1;131–8.
- Firme PALP. Modelagem Constitutiva e Análise Probabilística Aplicadas a Poços em Zonas de Sal. [Rio de Janeiro, Brazil]: Pontifícia Universidade Católica do Rio De Janeiro; 2013.
- Firme PALP, Brandao NB, Roehl D, Romanel C. Enhanced double-mechanism creep laws for salt rocks. *Acta Geotech* 2018 136 [Internet]. 2018 Jul 13 [cited 2021 Oct 21];13(6):1329–40. Available from: <https://link.springer.com/article/10.1007/s11440-018-0689-7>
- Firme PALP, Roehl D, Romanel C. An assessment of the creep behaviour of Brazilian salt rocks using the multi-mechanism deformation model. *Acta Geotech*. 2016;11(6):1445–63.
- Firme PALP, Roehl D, Romanel C. Salt caverns history and geomechanics towards future natural gas strategic storage in Brazil. *J Nat Gas Sci Eng* [Internet]. 2019 Dec 1 [cited 2022 Apr 7];72. Available from: <https://doi.org/10.1016/j.jngse.2019.103006>
- Firme PALP, Roehl DM, Romanel C, Poiate Jr, E. and Costa AM. Creep constitutive modeling applied to the stability of pre-salt wellbores through salt layers. *Am Rock Mech Assoc*. 2014;10.
- Fjær E, Stenebråten JF, Bakheim S. Laboratory Test for Studies on Shale Barrier Formation - OnePetro. In: American Rock Mechanics Association [Internet]. American Rock Mechanics Association; 2018 [cited 2019 Nov 1]. Available from: <https://www.onepetro.org/conference-paper/ARMA-2018-1146>
- Foh S, Novil M, Rockar E, Randolph P. Underground hydrogen storage. Final report. [Salt caverns, excavated caverns, aquifers and depleted fields]. 1979 Dec 1 [cited 2022 Apr 11]; Available from: <http://www.osti.gov/servlets/purl/6536941-eQcCso/>

- Fuenkajorn K, Daemen JJK. Boreole closure in salt. 1988;191–8.
- Fuenkajorn K, Phueakphum D. Laboratory assessment of healing of fractures in rock salt. *Bull Eng Geol Environ* [Internet]. 2011 Nov 20 [cited 2019 May 2];70(4):665–72. Available from: <http://link.springer.com/10.1007/s10064-011-0370-y>
- Grgic D, Al Sahyouni · F, Golfier · F, Moumni · M, Schoumacker · L, Grgic \* D, et al. Evolution of Gas Permeability of Rock Salt Under Different Loading Conditions and Implications on the Underground Hydrogen Storage in Salt Caverns. *Rock Mech Rock Eng* [Internet]. 2022 Feb 1 [cited 2022 Apr 12];55(2):691–714. Available from: <https://link.springer.com/10.1007/s00603-021-02681-y>
- Günther R, Salzer K, Minkley W, Popp T. Impact of tensile stresses and tensile fractures in rock salt on the evolution of the EDZ — capability of numerical modeling. 2015;(May):115–25.
- Hassanpouryouzband aliakbar, Joonaki E, Edlmann K, Heinemann N, Yang J. Thermodynamic and transport properties of hydrogen containing streams. *Sci Data* [Internet]. 2020 Dec 9 [cited 2022 Apr 13];7(1):222. Available from: [www.nature.com/scientificdata](http://www.nature.com/scientificdata)
- Hévin G. Underground storage of Hydrogen in salt caverns. In: *European Workshop on Underground Energy Storage*. Paris; 2019.
- Hou Z. Mechanical and hydraulic behavior of rock salt in the excavation disturbed zone around underground facilities. *Int J Rock Mech Min Sci*. 2003;40:725–38.
- Hou Z, Lux K-H. A new elastic/viscoplastic model for salt rock included damage and accelerated creep based on the Continuum-Damage-Mechanics. *Geotechnik*. 1998;21:259–63.
- Howarth RW, Jacobson MZ. How green is blue hydrogen? *Energy Sci Eng* [Internet]. 2021 Oct 12;9(10):1676–87. Available from: <https://onlinelibrary.wiley.com/doi/10.1002/ese3.956>
- Hult J, Lemaitre J. *Physical Non-Linearities in Structural Analysis*. Hult J, Lemaitre J, editors. Berlin, Heidelberg: Springer Berlin Heidelberg; 1981.
- Hunsche UE. Failure behaviour of rock salt around underground cavities. In: *Proceedings of the 7th Symposium on Salt*. 1993. p. 59–65.
- Iordache I, Schitea D, Gheorghe A V., Iordache M. Hydrogen underground storage in Romania, potential directions of development, stakeholders and general aspects. *Int J Hydrogen Energy* [Internet]. 2014 Jul 15 [cited 2022 Apr 12];39(21):11071–81. Available from: <http://dx.doi.org/10.1016/j.ijhydene.2014.05.067>
- Kachanov LM. Time of the rupture process under creep conditions. *Izv Akad Nauk S S R Otd Tech Nauk*. 1958;8:26–31.
- Khaledi K, Mahmoudi E, Datcheva M, Schanz T. Analysis of compressed air storage caverns in rock salt considering thermo-mechanical cyclic loading. *Environ Earth Sci* [Internet]. 2016a Aug 9 [cited 2022 May 4];75(15):1149. Available from: <http://link.springer.com/10.1007/s12665-016-5970-1>
- Khaledi K, Mahmoudi E, Datcheva M, Schanz T. Stability and serviceability of underground energy storage caverns in rock salt subjected to mechanical cyclic loading. *Int J Rock Mech Min Sci* [Internet]. 2016b Jul 1 [cited 2019 Feb 6];86:115–31. Available from: <http://dx.doi.org/10.1016/j.ijrmms.2016.04.010>
- Koning T. Is Brazil's Prolific Pre-Salt Petroleum Geology a Template for Oil &

- Gas Exploration in West Africa? GeoConvention 2015 New Horizons. 2015; Labaune P, Rouabhi · A, Tijani · M, Blanco-Martín · L, You · T. Dilatancy Criteria for Salt Cavern Design: A Comparison Between Stress- and Strain-Based Approaches. 2018 [cited 2022 May 10];51:599–611. Available from: <https://doi.org/10.1007/s00603-017-1338-4>
- Langer M, Hoshino K, Aoki K. Use of solution-mined caverns in salt for oil and gas storage and toxic waste disposal in Germany. *Eng Geol.* 1993;35(3–4):183–90.
- Lankof L, Urbańczyk K, Tarkowski R. Assessment of the potential for underground hydrogen storage in salt domes. *Renew Sustain Energy Rev* [Internet]. 2022 May 1 [cited 2022 Apr 12];160. Available from: <https://doi.org/10.1016/j.rser.2022.112309>
- Lao K, Bruno MS, Serajian V. Analysis of Salt Creep and Well Casing Damage in High Pressure and High Temperature Environments. In: *Offshore Technology Conference* [Internet]. Offshore Technology Conference; 2012. Available from: <http://www.onepetro.org/doi/10.4043/23654-MS>
- Lemmon EW, Bell IH, Huber ML, McLinden MO. NIST Standard Reference Database 23: Reference Fluid Thermodynamic and Transport Properties-REFPROP, Version 10.0, National Institute of Standards and Technology [Internet]. 2018. Available from: <https://www.nist.gov/srd/refprop>
- Li W, Miao X, Yang C. Failure analysis for gas storage salt cavern by thermo-mechanical modelling considering rock salt creep. *J Energy Storage* [Internet]. 2020 Dec 1 [cited 2022 Apr 7];32:2352–152. Available from: <https://doi.org/10.1016/j.est.2020.102004>
- Li W, Nan X, Chen J, Yang C. Investigation of thermal-mechanical effects on salt cavern during cycling loading. *Energy* [Internet]. 2021 Oct 1 [cited 2022 Apr 7];232. Available from: <https://doi.org/10.1016/j.energy.2021.120969>
- Liang G chuan, Huang X, Peng X yu, Tian Y, Yu Y hang. Investigation on the cavity evolution of underground salt cavern gas storages. *J Nat Gas Sci Eng* [Internet]. 2016 Jul 1 [cited 2022 Apr 7];33:118–34. Available from: <http://dx.doi.org/10.1016/j.jngse.2016.05.018>
- Lira WWM, Goncalves G de G, Araujo CN, Ramos Junior AS, Frery AC. Thermomechanical effect of vertical well drilling in salt rocks in selected cases. Vol. 32, *Engineering Computations*. Emerald Group Publishing Limited; 2015.
- Liu J, Xie H, Hou Z, Yang C, Chen L. Damage evolution of rock salt under cyclic loading in uniaxial tests. *Acta Geotech.* 2014;9(1):153–60.
- Liu W, Zhang Z, Chen J, Jiang D, Wu F, Fan J, et al. Feasibility evaluation of large-scale underground hydrogen storage in bedded salt rocks of China: A case study in Jiangsu province. *Energy* [Internet]. 2020 May 1 [cited 2022 Apr 12];198. Available from: <https://doi.org/10.1016/j.energy.2020.117348>
- Liu Y, Kabbour H, Brown CM, Neumann DA, Ahn CC. Increasing the Density of Adsorbed Hydrogen with Coordinatively Unsaturated Metal Centers in Metal-Organic Frameworks. 2008 [cited 2023 Jun 11]; Available from: <https://pubs.acs.org/sharingguidelines>
- Lomenick TF, Bradshaw RL. Deformation of Rock Salt in Openings Mined for the Disposal of Radioactive Wastes\* [Internet]. Vol. 1, *Rock Mechanics*. 1969. Available from: <https://link.springer.com/content/pdf/10.1007%2FBF01247355.pdf>
- Lyu C, Liu J, Ren Y, Liang C, Zeng Y. Mechanical characteristics and permeability

- evolution of salt rock under thermal-hydro-mechanical (THM) coupling condition. *Eng Geol* [Internet]. 2022 Jun [cited 2022 Apr 12];302:106633. Available from: <https://doi.org/10.1016/j.enggeo.2022.106633>
- Lyu C, Liu J, Zhao C, Ren Y, Liang C. Creep-damage constitutive model based on fractional derivatives and its application in salt cavern gas storage. *J Energy Storage* [Internet]. 2021 Dec 15 [cited 2022 Apr 7];44:103403. Available from: <https://doi.org/10.1016/j.est.2021.103403>
- Ma L, Wang M, Zhang N, Fan P, Li J. A Variable-Parameter Creep Damage Model Incorporating the Effects of Loading Frequency for Rock Salt and Its Application in a Bedded Storage Cavern Initial shear modulus of the spring in Kelvin body. 2017;50:2495–509.
- Ma LJ, Liu XY, Fang Q, Xu HF, Xia HM, Li EB, et al. A new elasto-viscoplastic damage model combined with the generalized hoek-brown failure criterion for bedded rock salt and its application. *Rock Mech Rock Eng*. 2013;46(1):53–66.
- Maia da Costa A, V. M da Costa P, D. Udebhulu O, Cabral Azevedo R, F. F. Ebecken N, C. O. Miranda A, et al. Potential of storing gas with high CO<sub>2</sub> content in salt caverns built in ultra-deep water in Brazil. *Greenh Gases Sci Technol*. 2019 Feb 1;9(1):79–94.
- Minkley W, Menzel W, Konietzky H, Kamp L t. A visco-elasto- plastic softening model and its application for solving static and dynamic stability problems in potash mining. 2001;
- Mohriak W, Szatmari P, Couto Anjos SM. *Sal: geologia e tectônica*. 2nd ed. Beca, editor. São Paulo; 2008.
- Munson D, Devries K. Development And Validation of a Predictive Technology For Creep Closure of Underground Rooms In Salt. 1991 Jan 1;
- Munson DE. Preliminary deformation-mechanism map for salt (with application to WIPP) [Internet]. Albuquerque, NM, and Livermore, CA (United States); 1979 Jan. Available from: <http://www.osti.gov/servlets/purl/6499296-lbtt3g/>
- Munson DE, Dawson PR. A Workhardening/Recovery Model Of Transient Creep Of Salt During Stress Loading And Unloading. 1982 [cited 2018 Apr 13]; Available from: <https://www.onepetro.org/download/conference-paper/ARMA-82-299?id=conference-paper%2FARMA-82-299>
- Nazary Moghadam S, Mirzabozorg H, Noorzad A. Modeling time-dependent behavior of gas caverns in rock salt considering creep, dilatancy and failure. *Tunn Undergr Sp Technol* [Internet]. 2013 Jan [cited 2022 Apr 7];33:171–85. Available from: <http://dx.doi.org/10.1016/j.tust.2012.10.001>
- Nazary Moghadam S, Nazokkar K, Chalaturnyk RJ, Mirzabozorg H. Parametric assessment of salt cavern performance using a creep model describing dilatancy and failure. *Int J Rock Mech Min Sci*. 2015;79:250–67.
- Niu C kai, Tan Y fei, Li J nan, Song C liang. Model validation and stability analysis for operation projects in Jintan Salt Cavern for strategic oil storage of China. *J Pet Sci Eng* [Internet]. 2015 Mar 1 [cited 2022 Apr 7];127:44–52. Available from: <http://dx.doi.org/10.1016/j.petrol.2015.01.029>
- Ozarslan A. Large-scale hydrogen energy storage in salt caverns. *Int J Hydrogen Energy* [Internet]. 2012 Oct [cited 2022 Apr 8];37(19):14265–77. Available from: <http://dx.doi.org/10.1016/j.ijhydene.2012.07.111>
- P.A.L.P. Firme, A.M. Costa, E. Poiate, M.A. Carrion DR 1, Firme PALP, Costa AM, Poiate Jr. E, Carrion MA, Roehl D. Casing Integrity of a Typical pre-salt Wellbore under Local Salt Dissolution Conditions. 13th ISRM Int Congr Rock Mech. 2015;(May):1–13.

- Pachauri RK, Allen MR, Barros VR, Broome J, Cramer W, Christ R, et al. Climate change 2014: synthesis report. Contribution of Working Groups I, II and III to the fifth assessment report of the Intergovernmental Panel on Climate Change. Ipc; 2014.
- Panfilov M. Underground and pipeline hydrogen storage. *Compend Hydrog Energy*. 2016 Jan 1;91–115.
- Parker FL. Status report on waste disposal in natural salt formations. Oak Ridge National Laboratory; 1958.
- Peach CJ. Influence of deformation on the fluid transport properties of salt rocks. *Faculteit Aardwetenschappen der Rijksuniversiteit te Utrecht*; 1991.
- Peng T, Wan J, Liu W, Li J, Xia Y, Yuan G, et al. Choice of hydrogen energy storage in salt caverns and horizontal cavern construction technology. *J Energy Storage* [Internet]. 2023 Apr;60:106489. Available from: <https://linkinghub.elsevier.com/retrieve/pii/S2352152X22024781>
- Petersen K, Lerche I. Temperature dependence of thermal anomalies near evolving salt structures: importance for reducing exploration risk. *Geol Soc London, Spec Publ*. 1996 Jan 1;100(1):275–90.
- Petrobras. Pre-Salt [Internet]. 2020 [cited 2020 Jun 1]. Available from: <http://www.petrobras.com.br/en/our-activities/performance-areas/oil-and-gas-exploration-and-production/pre-salt/>
- Petrobras. Petrobras [Internet]. 2023. 2023. Available from: <https://petrobras.com.br/en/our-activities/main-operations/basins/santos-basin.htm>
- Pierce WG, Rich EI. Summary of rock salt deposits in the United States as possible storage sites for radioactive waste materials. Vol. 1148. US Government Printing Office; 1962.
- Poiate EJ. Rock mechanics and computational mechanics for the design of oil wells in salt zones. Vol. I. Pontificia Universidade Católica do Rio De Janeiro; 2012.
- Popp T, Kern H, Schulze O. Evolution of dilatancy and permeability in rock salt during hydrostatic compaction and triaxial deformation. *J Geophys Res Solid Earth*. 2001 Mar 10;106(B3):4061–78.
- Portarapillo M, Di Benedetto A. Risk Assessment of the Large-Scale Hydrogen Storage in Salt Caverns. *Energies* 2021, Vol 14, Page 2856 [Internet]. 2021 May 15 [cited 2022 Apr 12];14(10):2856. Available from: <https://www.mdpi.com/1996-1073/14/10/2856/htm>
- Ramesh Kumar K, Makhmutov A, Spiers CJ, Hajibeygi H. Geomechanical simulation of energy storage in salt formations. *Sci Rep* [Internet]. 2021 Dec 4;11(1):19640. Available from: <https://www.nature.com/articles/s41598-021-99161-8>
- Van Sambeek LL, Ratigan JL, Hansen FD. Dilatancy of rock salt in laboratory tests. In: *International journal of rock mechanics and mining sciences & geomechanics abstracts*. 1993. p. 735–8.
- Schulze O, Popp T, Kern H. Development of damage and permeability in deforming rock salt. *Eng Geol* [Internet]. 2001 Aug [cited 2018 Dec 7];61(2–3):163–80. Available from: [www.elsevier.com/locate/enggeo](http://www.elsevier.com/locate/enggeo)
- SIMBECK D. CO<sub>2</sub> Capture and Storage—The Essential Bridge to the Hydrogen Economy. In: *Greenhouse Gas Control Technologies - 6th International Conference* [Internet]. Elsevier; 2003 [cited 2022 Apr 13]. p. 25–30. Available from: <https://linkinghub.elsevier.com/retrieve/pii/B9780080442761500052>
- Simon J, Ferriz AM, Correias LC. HyUnder - Hydrogen underground storage at

- large scale: Case study Spain. *Energy Procedia* [Internet]. 2015 [cited 2022 Apr 12];73:136–44. Available from: [www.sciencedirect.com](http://www.sciencedirect.com)
- Spiers CJ, Peach CJ, Brzesowsky RH, Schutjens P, Liezenberg JL, Zwart HJ. Long-term rheological and transport properties of dry and wet salt rocks. 1988.
- Staudtmeister K, Rokahr RB. Rock mechanical design of storage caverns for natural gas in rock salt mass. *Int J rock Mech Min Sci Geomech Abstr.* 1997 Apr;34(3–4):646.
- Tarkowski R. Underground hydrogen storage: Characteristics and prospects. *Renew Sustain Energy Rev* [Internet]. 2019 May 1 [cited 2022 Apr 19];105:86–94. Available from: <https://doi.org/10.1016/j.rser.2019.01.051>
- Teixeira Mendes CA, Gattass M, Roehl D. The GeMA framework – An innovative framework for the development of multiphysics and multiscale simulations. In: *Proceedings of the VII European Congress on Computational Methods in Applied Sciences and Engineering (ECCOMAS Congress 2016)* [Internet]. Athens: Institute of Structural Analysis and Antiseismic Research School of Civil Engineering National Technical University of Athens (NTUA) Greece; 2016. p. 7886–94. Available from: <http://www.eccomasproceedia.org/conferences/eccomas-congresses/eccomas-congress-2016/2383>
- Tractebel. *Pioneirismo: armazenamento de hidrogênio em alto-mar* | Tractebel [Internet]. 2021 [cited 2022 Apr 13]. Available from: <https://tractebel-engie.com.br/pt/noticia/2021/pioneirismo-armazenamento-de-hidrogenio-em-alto-mar>
- Vouille G, Bergues J, Durup G, You T. Study of the Stability of Caverns In Rock Salt Created By Solution Mining - Proposal For a New Design Criterion. *ISRM International Symposium - EUROCK 93.* 1993. p. ISRM-EUROCK-1993-095.
- Wang G. A new constitutive creep-damage model for salt rock and its characteristics. *Int J Rock Mech Min Sci.* 2004;41(SUPPL. 1).
- Wang J, Zhang Q, Song Z, Feng S, Zhang Y. Nonlinear creep model of salt rock used for displacement prediction of salt cavern gas storage. *J Energy Storage* [Internet]. 2022 Apr 1 [cited 2022 Apr 7];48:103951. Available from: <https://doi.org/10.1016/j.est.2021.103951>
- Wang TT, Ma HL, Shi XL, Yang CH, Zhang N, Li JL, et al. Salt cavern gas storage in an ultra-deep formation in Hubei, China. *Int J Rock Mech Min Sci* [Internet]. 2018 Feb 1 [cited 2022 Apr 7];102:57–70. Available from: <https://doi.org/10.1016/j.ijrmms.2017.12.001>
- Weast RC, Astle MJ. *CRC handbook of chemistry and physics*, 64 edn. CRC, Boca Rat. 1984;
- Xia C, Zhou Y, Zhou S, Zhang P, Wang F. A simplified and unified analytical solution for temperature and pressure variations in compressed air energy storage caverns. *Renew Energy.* 2015 Feb 1;74:718–26.
- Yang C, Daemen JJK, Yin J-H. Experimental investigation of creep behavior of salt rock. *Int J Rock Mech Min Sci* [Internet]. 1999 Feb [cited 2018 Dec 7];36(2):233–42. Available from: [https://ac.els-cdn.com/S0148906298001879/1-s2.0-S0148906298001879-main.pdf?\\_tid=c703bab2-6356-4d1b-b9f1-2a135aaffd83&acdnat=1544194036\\_537464ce232570a26a9216e6b7154d5f](https://ac.els-cdn.com/S0148906298001879/1-s2.0-S0148906298001879-main.pdf?_tid=c703bab2-6356-4d1b-b9f1-2a135aaffd83&acdnat=1544194036_537464ce232570a26a9216e6b7154d5f)
- Yin H, Yang C, Ma H, Shi X, Chen X, Zhang N, et al. Study on Damage and Repair Mechanical Characteristics of Rock Salt Under Uniaxial Compression. *Rock*

- Mech Rock Eng [Internet]. 2019 Mar 26 [cited 2019 May 3];52(3):659–71. Available from: <http://link.springer.com/10.1007/s00603-018-1604-0>
- Zhao K, Ma H, Yang C, Chen · Xiangsheng, Liu Y, Liang · Xiaopeng, et al. Damage Evolution and Deformation of Rock Salt Under Creep-Fatigue Loading The coefficient of determination h Stress triaxiality in Cocks and Ashby model W d Cumulative strain energy at the end of N cycles W 0 Cumulative strain energy at the end of the fin. Rock Mech Rock Eng [Internet]. 2021 [cited 2022 Apr 7];54:1985–97. Available from: <https://doi.org/10.1007/s00603-020-02342-6>
- Zhu C, Pouya A, Arson C. Micro-Macro Analysis and Phenomenological Modelling of Salt Viscous Damage and Application to Salt Caverns. Rock Mech Rock Eng [Internet]. 2015 Nov 7;48(6):2567–80. Available from: <http://link.springer.com/10.1007/s00603-015-0832-9>
- Zhu C, Shen X, Arson C, Pouya A. Numerical study of thermo-mechanical effects on the viscous damage behavior of rock salt caverns [Internet]. 2017. Available from: [https://smartech.gatech.edu/bitstream/handle/1853/58107/2017\\_arma\\_salt\\_caverns.pdf?sequence=1&isAllowed=y](https://smartech.gatech.edu/bitstream/handle/1853/58107/2017_arma_salt_caverns.pdf?sequence=1&isAllowed=y)
- Zivar D, Kumar S, Foroozesh J. Underground hydrogen storage: A comprehensive review. Int J Hydrogen Energy [Internet]. 2021 Jul 1 [cited 2022 Apr 12];46(45):23436–62. Available from: [www.sciencedirect.com](http://www.sciencedirect.com)

# Appendix A

## List of related studies developed during the Ph.D. program:

- Cavern integrity for underground hydrogen storage in the Brazilian pre-salt fields. The paper was approved for publication in the International Journal of Hydrogen Energy.

**ARTICLE IN PRESS**

INTERNATIONAL JOURNAL OF HYDROGEN ENERGY XXX (XXXX) XXX

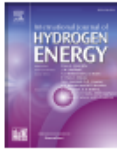


**ELSEVIER**

Available online at [www.sciencedirect.com](http://www.sciencedirect.com)

**ScienceDirect**

Journal homepage: [www.elsevier.com/locate/hydro](http://www.elsevier.com/locate/hydro)



---

## Cavern integrity for underground hydrogen storage in the Brazilian pre-salt fields

Williams Dias <sup>a,b</sup>, Deane Roehl <sup>a,b,\*</sup>, Cristian Mejia <sup>b</sup>, Paul Sotomayor <sup>b</sup>

<sup>a</sup> Department of Civil and Environmental Engineering, Pontifical Catholic University of Rio de Janeiro, 225 Marquês de São Vicente Street, Gávea, 22451-900, Rio de Janeiro, RJ, Brazil

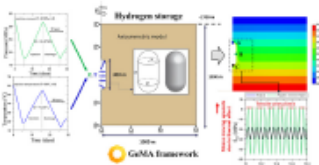
<sup>b</sup> Tecgraf Institute/PUC-Rio, 225 Marquês de São Vicente Street, Gávea, 22451-900, Rio de Janeiro, RJ, Brazil

---

### HIGHLIGHTS

- Simulation of underground hydrogen storage considering thermomechanical effects.
- Coupling thermomechanical finite element analysis with thermodynamics gas simulator.
- Assessment of salt rock integrity considering dilatancy and permeability evolution.
- Cavern integrity analysis using a unified analytical solution for P and T variations.
- Simulating different scenarios of underground hydrogen storage in Brazilian pre-salt caverns.

### GRAPHICAL ABSTRACT



---

### ARTICLE INFO

**Article history:**  
Received 17 December 2022  
Received in revised form 23 February 2023  
Accepted 19 March 2023  
Available online xxxx

**Keywords:**  
Hydrogen storage  
Creep  
Salt cavern  
Thermo-mechanical analysis

### ABSTRACT

Over the years, energy has depended on petroleum-based fuels. However, global warming and the energy crisis have drastically impacted the markets. It urges investing in renewable energy resources, such as hydrogen. Therefore, this work focuses on the hydrogen storage process in salt caverns, as these rocks have relevant properties, such as low permeability, relevant creep, and self-healing. A workflow for cavity integrity analysis is proposed. Hydrogen storage provokes variations in temperature and pressure inside the cavern. The gas thermodynamics is represented through a diabatic solution, which updates the gas pressure and temperature at each time step. The thermomechanical formulation is implemented into an in-house framework GeMA, which couples different physics. Four case studies are analyzed, and the discussions compared mechanical and thermomechanical models. Results demonstrate the importance of thermal effects, as

---

\* Corresponding author. Department of Civil and Environmental Engineering, Pontifical Catholic University of Rio de Janeiro, 225 Marquês de São Vicente Street, Gávea, 22451-900, Rio de Janeiro, RJ, Brazil.  
E-mail addresses: [wildias@tecgraf.puc-rio.br](mailto:wildias@tecgraf.puc-rio.br) (W. Dias), [deane@tecgraf.puc-rio.br](mailto:deane@tecgraf.puc-rio.br) (D. Roehl), [crismo@tecgraf.puc-rio.br](mailto:crismo@tecgraf.puc-rio.br) (C. Mejia), [paulortega@tecgraf.puc-rio.br](mailto:paulortega@tecgraf.puc-rio.br) (P. Sotomayor).  
<https://doi.org/10.1016/j.ijhydene.2023.03.292>  
0360-3199/© 2023 Hydrogen Energy Publications LLC. Published by Elsevier Ltd. All rights reserved.

Please cite this article as: Dias W et al., Cavern integrity for underground hydrogen storage in the Brazilian pre-salt fields, International Journal of Hydrogen Energy, <https://doi.org/10.1016/j.ijhydene.2023.03.292>

- ARMA 19–1567 : Casing integrity assessment of a wellbore crossing a karst cavity in a carbonate reservoir. Conference held in New York (USA) in June 2019;

ARMA 19–1567

## Casing integrity assessment of a wellbore crossing a karst cavity in a carbonate reservoir

Peña, W.D.L., Pereira, F.L.G., Firme, P.A.L.P. and Roehl, D.  
*Tecgraf Institute and Department of Civil Engineering – Pontifical Catholic University of Rio de Janeiro, Brazil*  
Pereira, L.C.  
*Petrobras, Rio de Janeiro, Brazil*

Copyright 2019 ARMA, American Rock Mechanics Association  
This paper was prepared for presentation at the 59<sup>th</sup> US Rock Mechanics/Geomechanics Symposium held in New York, NY, USA, 25–28 June 2019. This paper was selected for presentation at the symposium by an ARMA Technical Program Committee based on a technical and critical review of the paper by a minimum of two technical reviewers. The material, as presented, does not necessarily reflect any position of ARMA, its officers, or members. Electronic reproduction, distribution, or storage of any part of this paper for commercial purposes without the written consent of ARMA is prohibited. Permission to reproduce in print is restricted to an abstract of not more than 200 words; illustrations may not be copied. The abstract must contain conspicuous acknowledgement of where and by whom the paper was presented.



**ABSTRACT:** Different measures of porosity can coexist in carbonate reservoirs, ranging from micropores to large-scale cavities. It is well known that the construction of wellbores intersecting karst cavities can be seriously affected with lost circulation and kick. This work focuses on the casing integrity of a wellbore crossing a karst cavity in a carbonate reservoir during production. 3D geomechanical analyses using the finite element method are carried out. The model considers the main steps of the wellbore lifespan: initial stress state in the formation, drilling, casing run, pressure changes and pore pressure variation in the reservoir. The materials are modeled as elasto-plastic - von Mises criterion for the casing and Mohr-Coulomb criterion for the rocks and cement. Casing integrity (Yield Index, YI) is monitored through the evolution of the ratio between the von Mises deviatoric stress and yield stress with the pore pressure variation. The influence of a 1227m<sup>3</sup> cavity on the results is investigated through the development of two models: an open-hole completion with one production tubing, and a regular wellbore with intermediate and production casings. The results point out a maximum increase of 13.5% on the YI due to the cavity presence.

### 1. INTRODUCTION AND LITERATURE REVIEW

Exploration in carbonate reservoirs is a current priority and challenge for the oil and gas industry. Carbonate reservoirs are complex heterogeneous systems which consist of very low permeability matrix in contrast with high flow rate through fractures, and likely through vugs and cavities depending on the interconnection. The industry estimates that approximately 61% of the world's oil reserves are situated in carbonate zones (Roehl & Choquette, 1985).

The natural occurrence of fractures, vugs and cavities (Fig. 1) with several dimensions characterize a carbonate karst reservoir. These voids might be filled with loose material, such as gravel, mud and sand (Popov et al., 2007). Karstification process is generally categorized in two groups: epigenic and hypogenic. Horvath et al., 2015 define epigenic karstification as a "process of calcite dissolution in the course of infiltration of water including CO<sub>2</sub> from the atmosphere and soil." The water percolates through natural existing fractures in the rock and moves to surface streams or discharge areas, leading to an enlargement of these fractures (Legrand and Stringfield, 1973). Palmer, 1991 define hypogenic karstification as a process that form caverns "by acids of deep-seated origin, or epigenic acids rejuvenated by deep-seated process. Such caves have no relation to recharge through the overlying surface". Hypogenic karst environments present widespread porosity that can be of great economic importance (Palmer, 2011). Tian et al., 2017 presents results of the structure and filling characteristics of karst reservoirs situated at over 5300 m depth. They show that a single well can cross several cavities of different sizes. The level of karstification is influenced by the time for process evolution, and its intensity (Bosak, 2008).

Several approaches to consider the presence of karsts in reservoirs are proposed in literature. The presence of large-scale cavities at the wellbore interface may affect the drilling process, resulting in lost circulation followed by hydrocarbon influx into the wellbore (kick). Colbert and Medley, 2002 present the application of a technique to overcome or reduce the impacts of large fractures and karsts on well control during the drilling process. Sweep et al., 2003 describe a drilling technique applied in a high-pressure reservoir with vertical fractures and cavities.

Because of the difficulties to model carbonate karst formations, Popov et al., 2009 propose a unified approach